Doctoral Dissertation
Doctoral Program in Civil and Environmental Engineering (38th Cycle)

Hydro-climatic forcing of slow-moving landslides: data-driven and modelling approaches

By

Roberta Narcisi
* * * * * *

Supervisors:
Prof. Glenda Taddia, Supervisor
Prof. Federico Vagnon, Co-Supervisor

Doctoral Examination Committee:

Prof. Carlo Esposito, Referee, Università di Roma La Sapienza
Prof.ssa Sabrina Maria Rita Bonetto, Referee, Università di Torino
Prof.ssa Laura Longoni, Politecnico di Milano
Prof. Paolo Dabove, Politecnico di Torino

Politecnico di Torino
2026

Declaration

I hereby declare that, the contents and organisation of this dissertation constitute my own original work and does not compromise in any way the rights of third parties, including those relating to the security of personal data.

Roberta Narcisi

2026

* This dissertation is presented in partial fulfillment of the requirements for **Ph.D. degree** in the Graduate School of Politecnico di Torino (ScuDo).

Acknowledgment

First, I would like to thank my PhD supervisors, Glenda Taddia and Federico Vagnon, for their guidance and for the opportunities they have offered me to grow as a researcher over the years. I am also grateful to the Applied Geology group for their support and for guaranteeing such a productive environment for both research and teaching activities.

I would like to thank Ivan Depina for his valuable advice during my visiting period in Trondheim. The numerical modelling section of this dissertation was carried out under his supervision.

Thanks to Paolo Dabove, Chiara Colombero and Adriano Fiorucci for their constructive feedback, which helped me to strengthen and improve the quality of my research work.

Thanks to my colleagues at ARPA Piemonte – Mauro Tararbra, Luca Lanteri and Sergio Scalenghe – for their cooperation and availability, especially in the management of monitoring activities and data collection, which were essential for this study. Thanks also to Fabrizio Bianco, technician at the DIATI Hydrochemical Laboratory, for his assistance during field activities.

Special thanks go to Alessandro Berta and Luca Biamino for sharing their time and professional experience with me, and for making these years more pleasant, both in the office and outside the workplace.

Finally, I would like to thank my lifelong friends and the wonderful people I met during my PhD for believing in me and encouraging me to pursue an academic career, even during the most challenging times. Their presence greatly enriched this experience.

Thanks to my family for their constant support. My heartfelt thoughts go to my beloved grandmother, who passed away shortly before I submitted this dissertation. Her presence and love will always remain with me.

Abstract

Slow-moving landslides are large-scale gravitational phenomena governed by complex hydro-mechanical dynamics due to the interaction of multiple involved factors. Their long-term evolution could pose a significant geohazard to nearby settlements and infrastructure. Understanding the processes that cause these deformations is crucial for the development of effective monitoring and mitigation strategies. Furthermore, high climate variability makes landslide detection challenging. In mountainous regions, extreme hydroclimatic events, such as heavy and prolonged rainfall or snowmelt, can accelerate the transition from slow creep to significant landslide reactivations. In this framework, a detail investigation of the relationship between groundwater regimes and landslide behaviour is needed.

This work focuses on a few representative landslide sites located in the Western Alps (Piedmont region, Italy), an area highly prone to hydrogeological instability. The research proposed an integrated workflow combining displacement measurements, hydro-meteorological observations and hydrogeological indicators to quantify climate-driven controls on slope deformation and to improve predictive capability in changing conditions.

Landslide displacements are firstly analysed in response to significant climatic events, contextualised against normal precipitation and temperature values over the 1991–2020 reference period. Furthermore, the advantages of integrating monitoring techniques are highlighted by comparing displacement time series derived from in situ instruments (inclinometers) and remote sensing products (InSAR), showing how a ground-based network supported by satellite observations enhances the detection of long-term slope deformation patterns.

A core contribution of this dissertation is the investigation of mountain springs as indicators of aquifer dynamics and as proxies for landslide behaviour. The research aims to demonstrate that spring water levels can be used as a powerful tool for detecting slow-moving landslide displacements and establishing thresholds for early warning and risk mitigation. At the Thures and Champlas du Col landslide sites in the Susa Valley, a statistical approach based on cross-correlation and spectral analyses was employed to explore the relationship between groundwater level fluctuations and slope displacements.
Results showed that when springs and inclinometers are in proximity and belong to the same landslide dynamics, the spring trend can reliably predict conditions

triggering movement. However, the limited spatial distribution of springs over large areas, as well as their location with respect to other instruments, can represent a constraint for this analysis. Hydrochemical analyses were performed on a set of water spring samples to infer groundwater pathways within the landslide body, with the aim of reconstructing a conceptual hydrogeological model of the slope as well as the aquifer setting.

A data-driven predictive model was also developed to estimate displacement patterns by identifying the most impactful predictors. Leveraging the STL decomposition method for the time series involved and regression analysis, the proposed methodology enabled the definition of a preliminary but promising forecasting model to describe landslide kinematics.

Finally, a numerical analysis was carried out on the Champlas du Col landslide to evaluate the hydro-mechanical response of the slope under transient pore pressure variations resulting from a gradual rise in the groundwater table coupled with infiltration, in order to assess soil saturation conditions under different scenarios.

While this dissertation supports landslide acceleration forecasting, a more robust monitoring network is essential for detecting deformation phases. Nevertheless, this study lays the foundation for an alternative use of deep displacement monitoring integrated with transversal analytical tools, which can be further applied to similar landslide settings to improve site-scale hydrogeological characterization.

Contents

List of Tables

List of Figures

Research frame and thesis outline

This work is carried out within the the RETURN project (Multi-Risk sciEnce for resilienT commUnities undeR a changiNg climate), an Extended Partnerships funded by the National Recovery and Resilience Plan (PNRR - Mission 4, Component 2, Investment 1.3 - https://www.fondazionereturn.it/).

RETURN aims to enhance the understanding of environmental, natural and anthropogenic risks, as well as their interaction with the effects of climate change by integrating monitoring techniques and methodologies, with a particular focus on technology transfer and bridging between research and applications to support risk prevision and land use strategies.

The activities of this thesis were conducted within the vertical spoke VS2 "Ground Instabilities", which aims to assess the processes driving the long-term evolution of slope instabilities in mountain areas, through the exploitation of tools and analytical approaches capable of investigating the hydrogeological dynamics.

As reported in following table, this study contributes to the identification of potentially landslide-prone areas through the detection of geomorphological features and hydrogeological indicators (Task 2.2.1 - 2.2.2), the quantitative analysis of relationship between groundwater fluctuations and landslide displacements (Task 2.3.1) under extreme climatic scenarios for risk mitigation purposes (Task 2.5.4).

Study positioning within RETURN project tasks.

Task VS2	Research contribution	Application
T2.2.1 Identification of areas at different scales affected or predisposed to ground instabilities, either in the subaerial (a) and submerged (b) environment by existing inventories and archives – implemented and updated by EO services – and permanent and temporary geophysical observatories (dynamic mapping)	- Detection of predisposing factors to slow-moving landslides in mountainous environments: lithology, geological settings, tectonic stresses and deglaciation	- Preliminary characterization of mountain springs, as expression of aquifer dynamics in a landslide context
T2.2.2 Quantitative analysis of predisposition to ground instabilities through: (a) geological, geomorphological (including erosion, transport, deposition processes), and geotechnical parameters; (b) factors controlling coastal and seafloor environment, geomorphological setting, submarine mass wasting.	- Influence of the DSGSD morphostructure on infiltration dynamics and deep-water circulation	- Reconstruction of a hydrogeological conceptual model of a DSGSD by combining geological and hydrogeological data
T2.3.1 Natural onshore and offshore field laboratories for remote and in-site monitoring of environmental forcings and deformation responses. Validation of cutting-edge sensors, technological devices, and techniques to identify and monitor precursor signals of ground instability, as well as the occurrence of ongoing deformations T2.5.4 Eco-sustainable mitigation of ground instability scenarios in a changing climate framework	- Statistical approaches and numerical modelling for detecting cause-effect relationship between groundwater dynamics and landslide displacement - Champlas du Col and Thures landslide sites as local-scale LE to assess the impact of extreme climatic events on groundwater resources and slope stability	- Spring vs Piezometer in displacement rates detection - Landslide acceleration thresholds - Forecasting model - Semi-automatic tool for investigating slow-moving landslides under climatic forcing

Given these considerations, this dissertation is structured as follows.

Chapter 1 describes the geomorphological and hydrogeological characteristics of slow-moving landslides, providing a review of the key investigative approaches employed to clarify the underlying dynamics. The chapter also presents the study area of the Western Alps (Piedmont region), which is the focus of this work.

Chapter 2 outlines the methodological framework adopted to investigate the climate impacts on long-term gravitational processes in mountain environments, emphasising the role of monitoring techniques - InSAR and in situ observations - in detecting and interpreting slow deformation responses.

In Chapter 3 a data-driven model is developed to explore groundwater forcing on slow-moving landslides, evaluating the role of mountain springs as a valuable indicator of hydrogeological processes and slope deformation. Furthermore, the statistical approach employed is presented, highlighting its potential and limitations.

Chapter 4 focuses on the hydrochemical and physico-chemical analyses carried out on a series of springs, providing additional constraints into groundwater circulation within the landslide body.

Chapter 5 details the time-series decomposition and regression methods employed to quantify the temporal variability of the relationship between hydro-climatic preparatory factors and slope deformation, as well as to predict landslide displacement patterns.

Chapter 6 discusses the numerical modelling steps of a representative landslide site, exploring the hydrogeological response of the slope through the simulation of climate scenarios.

Finally, Chapter 7 summarises the main work achievement and research outcomes, as well as the further developments.

Chapter 1

Introduction

1.1 Slow-moving landslides: characteristics and monitoring approaches

Slope instability in mountainous regions poses a significant natural hazard, with long-term environmental, social and economic impacts which threaten human settlements and infrastructures (Peduto et al., 2025; Tawalo et al., 2025). The combined effects of geomorphological features, land use and increasingly extreme weather events, such as prolonged rainfall and intense storms, make these areas particularly vulnerable to landslide activity (Gariano & Guzzetti, 2016).
These processes affect the geomorphological evolution of the landscape at different scales, depending on the extent of the landslide, the displacement rates and the triggering factors involved, mobilizing soil and rock volumes from multiple slope sectors.

Large deep-seated, slow-moving landslides include several instability phenomena (Cruden & Varnes, 1996) which can persist for years or decades as combined or sequential processes, advancing at rates of a few millimetres per year (Agliardi et al., 2009). Within this framework, Deep-Seated Gravitational Slope Deformations (DSGSDs) refers to complex processes of gravitational movements that still represents an open issue in terms of risk assessment. Compared to the other landslides, DSGSDs cause potential damage associated to a continuous long-term deformation (Preisig, 2020).

The degree of displacement is relatively negligible given the size of the phenomenon, as DSGSDs typically span the entire length of high-relief valley flanks and thus involving very large areas and volumes. Consequently, defining their boundaries and the exact location of failure surface is extremely difficult. Nevertheless, the existence of these gravitational phenomena can be inferred from the presence of some geomorphological features in situ. The morpho-structural features characterizing DSGSDs most often follow tectonic (e.g. fault, joint, shear zones, bedding, foliation) or stratigraphic elements (e.g. lithological contacts, weak rocks). Their persistence can reach several hundreds of metres or more, and their role must be evaluated also considering their depth extent within the slope (Agliardi et al., 2001). As shown in Figure 1.1, the upper slope sector commonly shows trenches, scarps, double ridge, counter scarps, ridge top depression, highlighting an overall extensional regime. Conversely a compressive regime typically characterises the lower portions, as evidenced by toe bulging and variably fractured rock masses (Crosta et al., 2013). Secondary landslides, including a broad range of

instabilities (e.g. rock falls, rockslides, rotational and translational slides), usually occur in the middle and lower portion, as a consequence of the progressive and continuous evolution of these large phenomena.

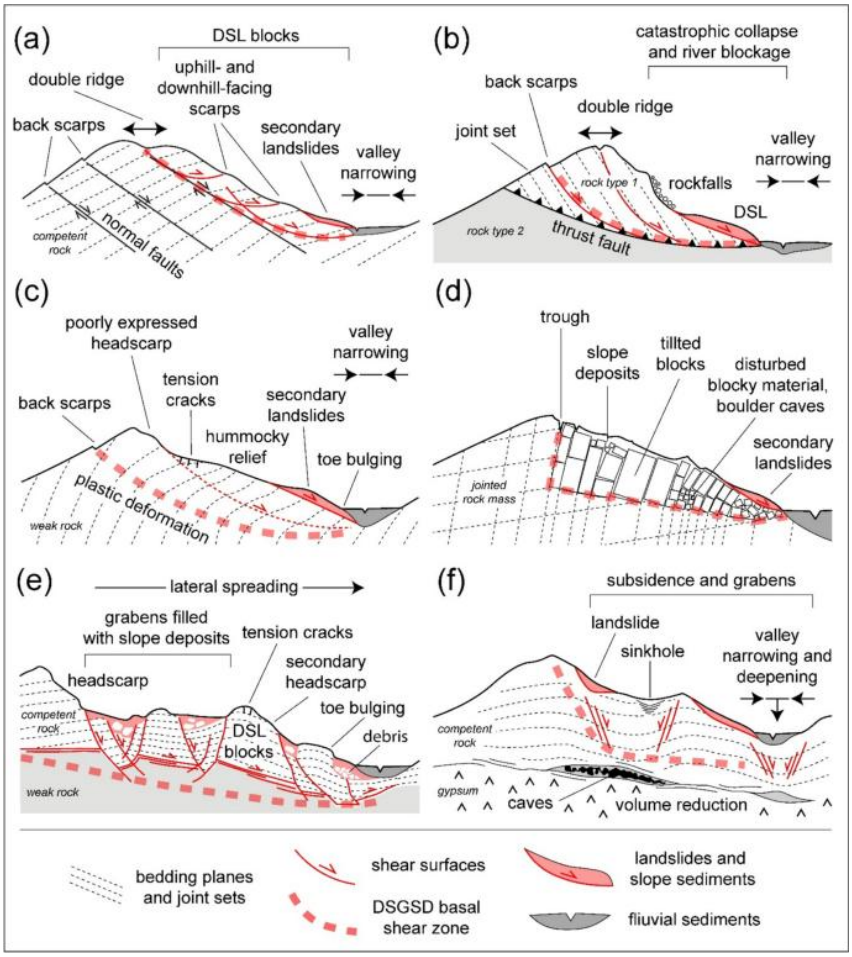

Figure 1.1 Conceptual classification of the DSGSDs based on their controlling factors. (a) Tectonically controlled by a normal fault. (b) Tectonically controlled by a thrust fault and/or lithological contact. (c) Controlled by plastic deformation (rock mass creep). (d) Structurally controlled by discontinuities – toppling. (e) Lateral spreading type. (f) Karst-related and/or subsidence type (Tolocka 2025).

These features can play a major role in controlling the failure, changing mechanical properties and influencing superficial and deep-water circulation.
For instance, long slope transversal features can redirect runoff water, facilitate concentrated infiltration from rainfall and snowmelt, and control anisotropy of hydraulic conductivity, groundwater flow direction and spring location.

The kinematics and long-lasting evolution of DSGSDs are governed by the interaction of a whole set of factors and processes that can lead to meaningful acceleration stages and catastrophic failure (Cheng et al., 2023; Liu et al., 2025). It is important to classify the role of multiple factors according to their intensity and characteristic timescales. The predisposition to instability is inherent to factors that are independent of time, such as the lithology, structural settings and tectonic regime of a given context. On the other hand, preparatory factors can be associated

with near-term changes, including deglaciation and the resulting erosion, topographic stresses, valley incision, fluctuations in the groundwater regime and rock dissolution. Finally, the immediate effects that usually coincide with episodic accelerations are attributable to triggering factors, such as seismic activity or exceptional rainfall events.

Deglaciation is a notable example of an impactful driving process for DSGSD deformations. It causes a relative fast reversal of the conditions with extension close to the ridges and compression along the valley bottom, with an increase in differential stresses, which can cause rock damage (Hugentobler et al., 2020; Zachos et al., 2001). Finally, the presence of active tectonic stresses can induce an increase of compressive stresses, both at the valley bottom and at the ridges, and ice loading can counteract and partially suppress them. These changes in loading conditions on the valley bottom and flanks can interact with the fracture opening and consequently with hydraulic conductivity and groundwater circulation. Most of the DSGSDs described in the literature are found in formerly glaciated valleys affected by a sort of progressive failure mechanism (Eberhardt et al., 2004; Terzaghi, 1962). This suggests that geometric, stress and kinematic changes during deglaciation could lead to strength degradation due to progressive rock damage, a process that can continue for thousands of years after the ice retreats. This phenomenon was observed in the European Alps following the Last Glacial Maximum (LGM) (Leith et al., 2014).

In terms of spatial distribution, Europe is the continent with the highest concentrations of DSGSDs, followed by Asia, with notable clustering in specific areas such as the Western Alps and the Central Apennines (Toločka, 2025). Within these mountain chains, DSGSDs represent a pervasive component of large-scale slope instability and are often closely associated with major valley systems.

It is important to note that the Alpine territory, despite its high relief, is one of the most anthropized mountain chain in the world, with diffuse environmental and cultural heritage. About the 8% of the Italian Western Alps territory is affected by DSGSD, and within this context, the Torino Province is particularly involved (10.5% of the mountainous territory) with a concentration in the main valleys of the region (i.e. Susa Valley, Chisone Valley, Pellice Valley) located in the middle-low portion of the province (Figure 1.3b).

The Alpine landscape has been shaped by centuries of human presence and, through its social, cultural and economic footprint, represents a territory highly susceptible to landslide hazard, especially due to the presence of widespread tourist villages and ski resorts such as Bardonecchia, Sauze d'Oulx, Sestriere (Torino Province), and Valtournenche and Courmayeur (Aosta region).

With regard to the state of activity of the DSGSDs affecting urbanized areas in the Aosta Valley region and in the upper Susa Valley, approximately 22% are classified as active (Cignetti et al., 2020).

The observed damage associated with DSGSDs and their smaller fast-evolving secondary instabilities ranges from slight effects to severe impacts on buildings and infrastructure network (Lacroix et al., 2020). Well-known examples can be found in the Susa Valley (Dora Riparia river basin) near the Champlas du Col locality

(Sestriere) (Figure 1.2) and near the town of Salbertrand, where a complex landslide threatens the highway A32 Torino-Bardonecchia (Mondino et al., 2009).
Despite the long-term impact of these phenomena on strategic structures and infrastructures, a clear hazard assessment methodology and a dedicated urban planning regulatory framework are still lacking in Italy (Cignetti et al., 2020). In addition, due to their limited displacement rates and their areal extension, these phenomena are not usually monitored by onsite instruments, as it is being done for smaller and faster landslides. This may cause an underestimation of the movement rate and, consequently, of the potential effects of the DSGSDs on human activities and other anthropic elements at risk.

In this regard, advanced remote sensing technologies based on higher-quality satellite data are widely exploited for the measurement of ground displacements over a quite long-time span, providing data with extensive spatial coverage and monitoring areas with limited accessibility. Teshebaeva et al. (2019) applied time-series interferometric synthetic aperture radar (InSAR) techniques to quantify slow surface deformations, highlighting the role of lithology, bedding orientation, and tectonic activity as primary controls on DSGSD kinematics.
On a larger scale, (Toločka, 2025) emphasised the importance of systematic regional mapping and multi-sensor monitoring to enhance the detection of the global distribution and evolutionary stages of DSGSDs, as well as the collection of geological structural data, pointing to advances in geochronology, LiDAR, InSAR, and near-surface geophysics as crucial for future research progress (Frattini et al., 2018). While these approaches are effective for detecting slow-moving instabilities in high mountain regions, they mainly assess surface kinematics and thus providing limited insight into of the processes that governing the initiation and evolution of these phenomena.

Indeed, the complexity of DSGSDs settings and the associated instabilities make it challenging to apply ad hoc analytical techniques as well as to plan effective mitigation strategies. Although recognized for decades, a comprehensive investigation of their hydro-mechanical behaviour has only recently advanced thanks to the integration of high-resolution monitoring, geostatistical modelling, and hydrogeochemical analyses. DSGSDs activity is not solely controlled by structural and lithological factors, but also strongly governed by subsurface hydrogeological processes, particularly variations in groundwater recharge and pore pressure variations within shear zones.

Given these assumptions, a deeper knowledge about their hydrogeological control is required, and therefore the development of a suitable model aiming to clarify the groundwater dynamics. For this aim, various methods have been proposed to characterize groundwater flow, storage and response to precipitation including (i) hydrochemistry (Cervi et al., 2012); (ii) hydromechanical modelling (Cappa et al., 2014); (iii) reactive and conservative tracer tests (Bogaard et al., 2007; Hilberg & Riepler, 2016; Ronchetti et al., 2020; Vallet et al., 2015) and (iv) non-invasive geophysical methods (Chalikakis et al., 2011; Jomard et al., 2010; Lajaunie et al., 2019; Zieher et al., 2017).

Several studies have emphasised the importance of correct groundwater monitoring to ensure a proper management of water resources, particularly in mountainous regions. In this sense, springs supplied by the aquifer, play a relevant role in hydrogeological investigations. Desmarais & Rojstaczer (2002) and (Galleani et al. (2011) showed how the spring behavioural model of the drainage can be understood by analysing continuous dataset of rainfall (P), discharge (Q), temperature (T) and electrical conductivity (EC). The temporal variation of these parameters provides useful insight into the aquifer structure (Chiaudani et al., 2019), allowing to predict the volume of groundwater stored at the end of spring and autumn seasons. The dynamics of mountain groundwater resource depletion are heavily influenced by climate conditions. As reported by Cantonati et al. (2022) the water residence time characterizes the retention of spring system. If the water stays in the groundwater body for an extended period, a delayed impact of climatic changes on the spring system is expected. Correspondingly, groundwater bodies with a larger volume have higher resilience to increasing temperatures than smaller ones with the same flow velocity. Therefore, springs that drain small groundwater bodies are likely to be affected more quickly by climate change (Cerino Abdin et al., 2021; Gizzi et al., 2020, 2022; Mondani et al., 2022).

New automated techniques must be employed in the analysis of aquifer hydrogeological parameters to fully understand the dynamics of exhausting available groundwater resources.

Furthermore, recent works have underscored the potential of the autocorrelation and cross-correlation methods for analysing mountain spring monitoring datasets (Fiorillo & Doglioni, 2010; Kresic & Stevanovic, 2010; Kresic & Bonacci, 2010; Panagopoulos & Lambrakis, 2006). Statistically, the autocorrelation of a time series (e.g. spring discharge) describes the correlation between values of the process (Q) at different points in time (t), as a function of the two times or the time difference. The cross-correlation represents a time-dependent relationship between an output process (e.g. daily spring discharge) and an input process (e.g. daily precipitation). Within this methodological framework, SOURCE (Spring mOnitoring data analysis and aqUifeR CharactErization) is an example of an advanced semi-automatic Python tool that automates the hydrogeological characterization of the aquifer behavior as described by Lo Russo et al. (2021). Its reliability has been tested by analysing several mountain springs located in the Aosta Valley region (north-western Italy), enabling the rapid extraction of key aquifer descriptors (e.g., memory effect and lag time response) to support comparative assessments of the system sensitivity and vulnerability to climate forcing (Gizzi et al., 2023).

In the context of gravitational phenomena, continuous monitoring of spring data enables a detailed understanding of the extent to which the presence of a DSGSD influences the position, discharge and chemical-physical characteristics, as well as the infiltration dynamics and vulnerability of the analysed spring (Forno, 2012). An example from the Alpine glacial valley of Rodoretto (Germanasca Valley, Italian Western Alps) affected by a DSGSD shows how the widespread presence of open fractures and the consequent high degree of loosening of the rock substrate (Forno et al., 2011) proved to be very favourable for the storage of large

quantities of water. Additionally, several mountain springs have been identified along the longitudinal trenches mapped in the upper sector of the Rodoretto Valley, many of which are potentially exploitable for drinking water purposes (Gizzi et al., 2020). In this framework, De Luca et al. (2019) underlined the importance of characterizing mountain springs by combining field surveys, tracer tests and hydrochemical analyses with the aim to reconstruct a hydrogeological conceptual model of a DSGSD. Similarly, Pfeiffer et al. (2022) proposed a geostatistical approach, based on stable isotopes as natural tracers, to obtain insights into the hydrogeological setting of deep-seated landslides. This study mapped probable recharge areas that critically influence slope hydrology, providing a methodological basis for designing mitigation strategies such as drainage systems.

Additionaly, the investigation of the groundwater response to precipitation inputs of different intensities and durations is essential to understand the coupled hydro-mechanical behaviour of deep-seated slope deformations (Prokešová et al., 2013). The enduring motion of these landslides depends on variations in the groundwater regime (Yokoyama et al., 2022). Specifically, variations in pore pressure, which are closely related to net rainfall and snowmelt feeding the aquifer, control the movement rate in both acceleration and deceleration phases. This results in a decrease in effective stress which in turn reduces the frictional force acting on the landslide body; thus, the mass mobility increases along the slip surface (Cascini et al., 2010; Handwerger et al., 2013). Due to the involvement of several features, including precipitation, pore water pressure, soil strength and movement rates, a numerical model is the most efficient way to investigate the impact of climate forcing on slope stability and evaluate soil water content and to perform the hydromechanical evaluation of the slope (Lee et al., 2021).

Climate transition complicates this scenario by posing additional challenges for both risk assessment and the development of long-term mitigation strategies. The increasing variability in rainfall intensity and duration has made the hydro-meteorological processes influencing slope stability more unpredictable (Zhang et al., 2024; Zieher et al., 2023).

Figure 1.2 Main impact of the evolution of the DsGSD on anthropic element recognised in the Italian Western Alps: the Champlas du Col landslide with (a) significant damage to roads (SP23R) due to secondary landslides associated with the DsGSD and (b) injuries to buildings.

1.2 Study area

This research is focused on the Western Alps (Piedmont region, Italy) and involves the Dora Riparia (1210 km^2) and Chisone (604 km^2) river basins (Figure 1.3a) with elevation ranging from to 211 to 3534 m a.s.l.

At least 70% of the municipalities belonging to this area are exposed to high hydrogeological hazard (Italian platform on hydrogeological instability – IdroGEO https://idrogeo.isprambiente.it/app/). Roto-translational slides phenomena and rockfalls prevail above 1500 m, due to the snow melting and ice thawing. In the medium-lower sector of the Dora Riparia basin, complex landslides and flows are widespread, involving more or less altered and disaggregated rock substrates (Bordoni et al., 2023; Forno et al., 2016). From a geomorphological point of view, the setting of this Alpine region was completely reshaped by glacial morphogenesis during the Upper Pleistocene, erasing any sedimentary trace of the period before the Last Glacial Maximum (LGM) (Cignetti et al., 2020). Evidence from drilling surveys conducted on various landslides have revealed that the evolution of gravitational phenomena has altered the original post-glacial morphology of valley bottoms (Fioraso et al., 2011). With the end of the LGM approximately 19000 years ago (Deline & Orombelli, 2005) the volume of glacial tongues decreased and glacial fronts retreated rapidly, causing significant deepening of the valleys.

At the same time, gravitational morphodynamics played a predominant role in modelling the slopes, by causing landslides and deep gravitational subsidence. These phenomena are prevalent due to the lithological and stratigraphic structure of the substrate. Both basins are predominantly covered by Lago Nero oceanic units (LCS), consisting of calcschists and serpentinites belonging to ophiolitic units, with intercalations of serpentine schists from the Cerogne-Ciantiplagna unit (CNR) (Figure 1.3c). The poor geomechanical properties of these metamorphic lithoids and the marked anisotropy of rock masses make the whole area susceptible to erosion and hydrogeological instability. The widespread formations of the Quaternary succession consist of continental deposits of glacial origin, developed during LGM, irregularly distributed along the slopes. In contrast, alluvial deposits are located along the main valley bottoms and are sometimes connected with DSGSDs and large active landslides that affect extensive areas of the valley (Fioraso, 2017; Fioraso & Mosca, 2014).

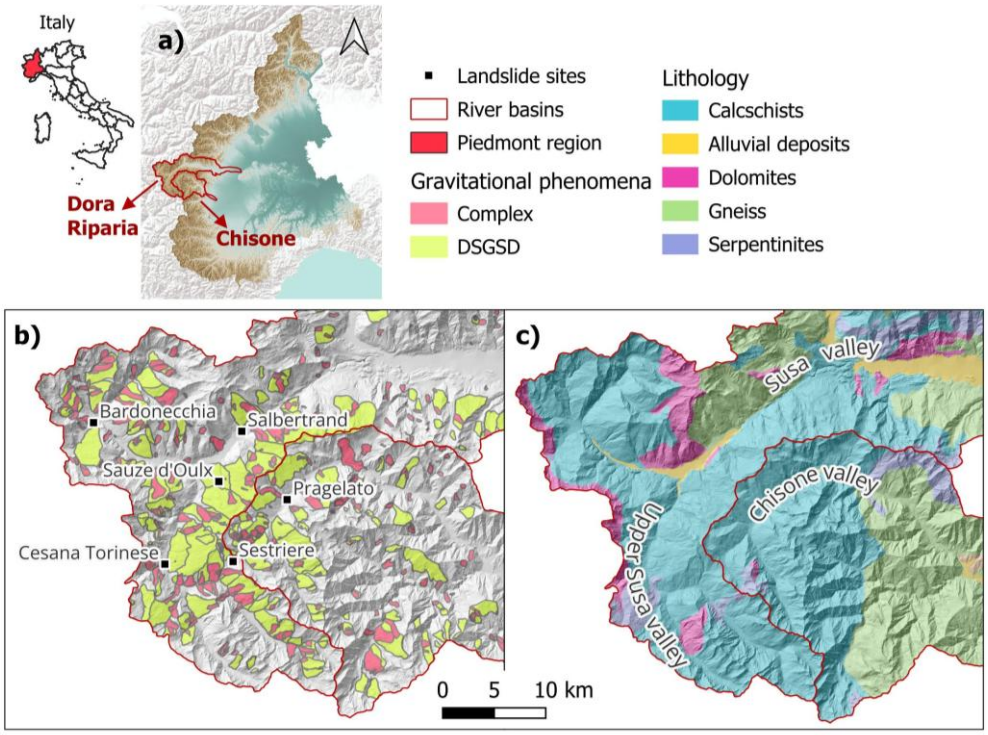

Figure 1.3 (a) Location of the Dora Riparia and Chisone river basins; (b) Distribution of the main landslide sites and DSGSDs; (c) geological framework.

Among the predisposing factors contributing to slope instability in the area, tectonic features strongly influenced the drainage network and landscape morphology, as testified by the Dora Riparia and Chisone rivers and tributaries pattern, which is controlled by NE-SW and NNW-SSE fault systems. In this context, the upper Susa Valley and the upper Chisone Valley stand out for an exceptional concentration of DSGSDs and large landslides, accounting for 38% of the Western Alps. These valleys are regarded as one of the best examples of the interaction between recent tectonic evolution of the relief and slope dynamics, as well as being affected by some of the largest DSGSDs recognised throughout the Alps (Fioraso et al., 2011).

The area covered by individual phenomena is almost always greater than 2–3 km², reaching a maximum of 13 km² in the case of the gravitational collapse in the S. Sicario hamlet (Cesana Torinese). Due to the lack of data on the deep subsoil and the nature of the deformation, which does not provide a precise physical limit within the rock mass involved, the thickness of the rock is difficult to assess (Fioraso & Mosca, 2014).

In addition to the aforementioned factors, karst phenomena significantly contribute to the movement of some gravitational collapses located near the outcrops of the underlying evaporite masses at some of the main tectonic contacts. The intense activity of dissolution processes is confirmed by the hydrogeochemical characteristics of waters draining the slope, as well as by the recent formation of sinkholes on the surface of the gravitational phenomenon itself.

Surface slope instabilities (typically lass than 20 m) manifest as a variety of gravitational phenomena that differ in size and movement rate, such as complex, rotational and translational landslides with flow components.
Almost all of the monitored landslides in the area are considered evolving, as evidenced by the recent detachment niches and accumulation zones, the widespread reactivation following intense rainfall (e.g. the October 2000 flood event) or rapid snowmelt (e.g. the May 2009 and May 2018), the continuous deformation of the road network (e.g. S.R. n. 23 Colle del Sestriere and S.P. n. 215 Sestriere-Cesana) and the damage to numerous buildings (e.g. Duc, Chezal, Borgata, Champlas du Col and Grange Sises).

From a climatic perspective, the study area is protected by the alpine chain from the Atlantic and the Mediterranean moist currents, which reduces rainfall intensity. In the catchment areas of interest, average precipitation ranges from 800 mm/year in the plains to around 1000 mm/year at higher elevation (Autorità di Bacino del fiume Po, 2023a-b). Above 2000 m, precipitation is predominantly snowfall. The largest contribution of flood flows comes from the effect of snowmelt in the spring and summer seasons.

Chapter 2

Climate impacts on surface deformation: in situ and remote sensing techniques

The work described in this chapter has been partially derived from (Narcisi et al., 2024).

2.1 Introduction

In recent decades, there has been growing awareness of the profound influence that climatic factors have on water resources (Leone et al., 2021; Gizzi et al., 2022; Golian & Ruigar, 2015) and, in turn, on landslide activity (Mo et al., 2019) in mountainous regions.

Evaluating the climate change impacts on slope instability is an effort for the scientific community. Even more challenging is the quantitative assessment of future variations in landslide occurrence and frequency related to heavy rainfall and anomalous temperatures (Gariano et al., 2017). Rising global temperatures is unequivocal (Legg, 2021), and its effects have been observed in many regions, especially in the most vulnerable ones, such as mountain areas where water resources are threatened (Gizzi et al., 2023). Significant changes may also be expected in precipitation regime, since the capacity of air to hold moisture is a function of temperature. In general, global warming is therefore likely to lead to an overall greater frequency and magnitude of heavy precipitation events (Calvin et al., 2023).

Several authors have carried out research focusing on relationships between climate trends and landslide activations or changes in displacement rates. The studies revealed a wide range of impacts of climate variations on landslides, including contradictory, uncertain and undetermined effects (Gariano & Guzzetti, 2016).

As an initial step, a whole understanding of the climate pattern in a given location is essential to identify possible series of anomalies with respect to reference values. In pursuit of this objective, the World Meteorological Organization (WMO) has defined climate normals with the aim of comparing observations and providing

average values that are representative of the current or past climate, establishing a reference period of 30 years (WMO, 2017).

Over the years, various approaches have been proposed to evaluate long-term precipitation and temperature regimes and, in particular, their influence on slope instability. (Nigrelli & Chiarle, 2021) have investigated the temperature indices of the European Alps in the period 1990-2019, revealing the identification of one or more climate anomalies possibly correlated with instances of ground instability in specific case studies. (Paranunzio et al., 2019) performed a probabilistic analysis assuming a set of the most representative climate variables on the occurrence of slope failures at high-elevation sites. As a result, 92% of the case studies were attributable to climate anomalies.

In mountainous regions, the occurrence of landslides is influenced by the microclimatic conditions at different altitudes. For instance, the warming and thawing of permafrost may reduce the stability of rock slopes, leading to debris flow. Above the elevation of 1500 m, the expected decrease of snow season in future years will likely affect the frequency and seasonality of landslide reactivations. Analysis of landslide areas in Piedmont adds further evidence to the observed changes in triggering climatic conditions and their impact on landslide occurrance. In this region, it has been demonstrated that landslides have become more frequent during the 21st century, particularly in early spring, often triggered by moderate rainfall (Stoffel et al., 2014).

In this perspective, the role of the monitoring network is crucial for understanding the spatial distribution and temporal evolution of ground defromations. The data acquired both in field and by remote sensing techniques are useful to detect mass movements, sometimes imperceptible, in response to predisposing factors, in particular landslides acceleration due to climate events. In this regard, the InSAR approach stands out as a valuable analysis tool thanks to its spatial accuracy and high temporal resolution of measures (Cigna et al., 2011; Pedretti et al., 2023).

Given these assumptions, the present work aims to explore potential relationships among changes in climatic trends and landslide displacements within Dora Riparia and Chisone basins, focusing on three case studies of slow-moving landslides, monitored for the presence of sensitive elements such as buildings and roads. This chapter is structured as follows (see Figure 2.1). Section 2.2 describes the case studies and choice of landslide monitoring data. Section 2.3 presents (i) the evaluation of significant events and anomalies with respect to the reference thirty-year period 1991-2020 climate trends (Frei & Schär, 1998) and (ii) the effects of climatic factors on landslide displacements observed for each case study from field monitoring stations and InSAR. Finally, in the discussion section, the results obtained are argued and integrated with additional information concerning landslide areas to better understand the outputs of the analysis.

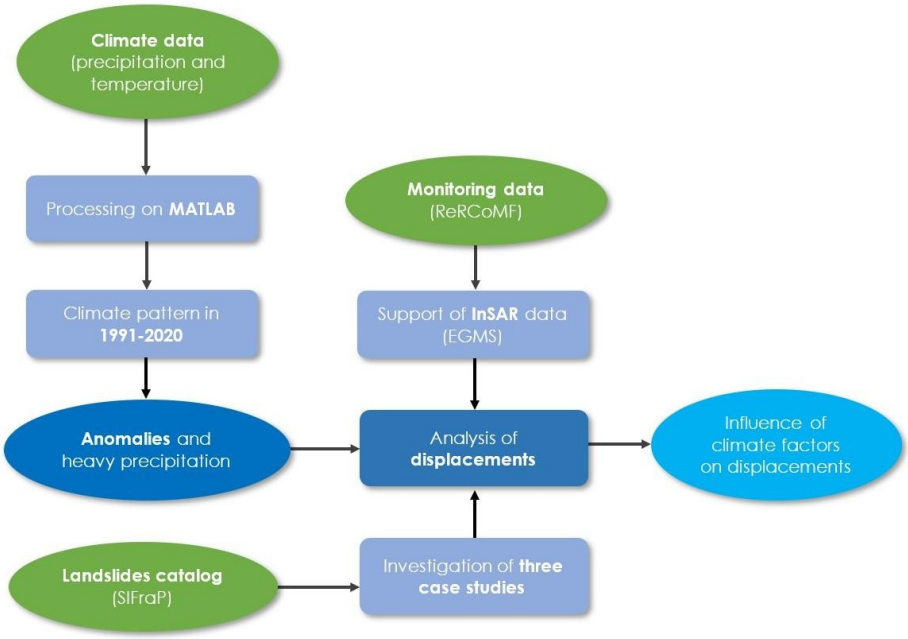

Figure 2.1 Conceptual workflow of climate data, landslide inventory and monitoring datasets processing.

2.2 Materials and methods

For the analysis purposes, a characterization of the investigated area was set up by implementing a geodatabase in Geographical Information System (GIS) environment, capable of managing a large amount of collected spatial data, as suggested by (Giardino et al., 2004). Geomorphological and climate data were included in the geodatabase, to provide a framework of the area in terms of landslide hazard (Audisio et al., 2017). Furthermore, for a detailed view of landslide deformations, displacement assessment included time series from regional monitoring network catalogues and satellite datasets with spatial and temporal information.

2.2.1 Landslide sites

The distribution of landslides in basins territory is collected in the Landslide Information System in Piedmont (Sistema Informativo Frane in Piemonte - SIFraP) inventory, the database of landslides at regional scale. This system is composed of three levels of detail depending on the level of information available for each site. In particular, the case studies presented in this chapter are categorized in the level II sheets so these are phenomena described in detail for morphological features and their continuous displacement monitoring. The catalog is available on the Arpa Piemonte geoportal and it contains all the landslide geometries that can be visualized and processed in GIS environment. Each landslide is identified by a code

and details about the type of movement, state of activity, date of observation, and location are given.

The investigated landslide sites (Figure 2.2) are listed in the following order: a) DSGSD in Sauze d'Oulx; b) Roto-transational slide in Pragelato; c) Complex landslide in Sestriere.

a) The lower-middle slope of the Sauze d'Oulx and Oulx municipalities, located on the topographic right of the Susa Valley, is affected by a DSGSD (Cignetti et al., 2024). This gravitational phenomenon, interesting an area of 5.4 km^2 and ranging in elevation from 1087 m to 1768 m a.s.l., represents one of the largest landslides of the Western Alps. The morphological and hydrogeological attributes distinguishing the Sauze d'Oulx phenomenon exhibit certain differences compared to other DSGSDs in this area. The collapsed slope is characterized by a fan shaped morphology and it is subjected to a rapid evolution, movement similar to rock flow controlled by a deep-seated continuous creep process involving serpentinites. Geomorphologically, the deformation is characterized by numerous pre-existing shear surfaces, attributed to the prevalence of calcareous schist and serpentines, rendering the entire slope fractured and highly permeable. Consequently, surface water circulation is absent, and water infiltration contributes to an aquifer located at significant depth.
Over time, multidisciplinary approach has been developed to comprehend the kinematic evolution DSGSD. The existence of an integrated monitoring system, based on an inclinometer system, satellite and ground-based interferometric techniques and a network of GPS stations, has made it possible to define a kinematic model of the phenomenon, providing information on the horizontal and vertical components of surface movement (Fioraso et al., 2010). Specifically, the surveys demonstrated the existence of gravitational activity traces, both ancient and recent, due to the presence of scarps, counter-slopes and closed depletions. Deformation time series have been continuously monitored since January 1999 through a network managed by Arpa Piemonte, which has installed instrumentation in proximity of buildings with the aim to record damages due to movements (Arpa Piemonte, 2023a).

b) In the Pragelato municipality, at Plan hamlet, there is an evident roto-translational slide phenomenon evolving into local flows, with an extension of 0.25 km^2. In the upper slope, between 2075 m and 1940 m a.s.l., the substrate is intensely fractured up to the landslide detachment zone, this ensures a significant infiltrative contribution that supplies widespread water springs. The accumulation body ranges between 1940 m and the valley floor where the Plan locality is located (1680 m a.s.l.). The evolution of the landslide body, at the bottom, directly involves the road sector of the SP23R regional road connecting the Susa and Chisone valleys, for a length about 1300 meters in correspondence with the hairpin bends that descend to the Pragelato plain. In fact, lesions are found on the retaining walls of the road massif with a width of the order of about twenty meters. The landslide activity, monitored by ground-based instruments and satellite techniques, is given by the combination of two movements, starting with the upstream roto-translative sliding

along some fractures in the substrate of calcareous schist, and developing into a flow in the accumulation zone, characterized by incoherent soils. The complexity of the phenomenon is therefore due to the geological characteristics of the slope (Arpa Piemonte, 2023b).

c) The complex landslide is located in Champlas du Col locality (1768 m a.s.l.), along to SP23R road. The landslide covers an area of 2 km^2, extending from an elevation of 2080 m a.s.l. down to the Ripa Valley floor at approximately 1500 m a.s.l. The phenomenon is the superficial expression of a larger DSGSD that extends to the top of the relief. Surface movements, such as flows and rotational slides are very active and periodically cause damage the SP23R road. A monitoring plan (starting in 2005) of the main landslides affecting this area, which had already been started previously (in 2001), was set up according to the directives of the Piedmont Region Technical Services. Concerning the interferometric data, several datasets are available in ascending and descending geometry, but the southern exposure of the slope does not allow a precise assessment of the magnitude of the surface displacements. Most of monitoring points are placed in proximity of Champlas du Col settlements and along the SP23R road due to recurring damage caused by continuous movement (Arpa Piemonte, 2023c).

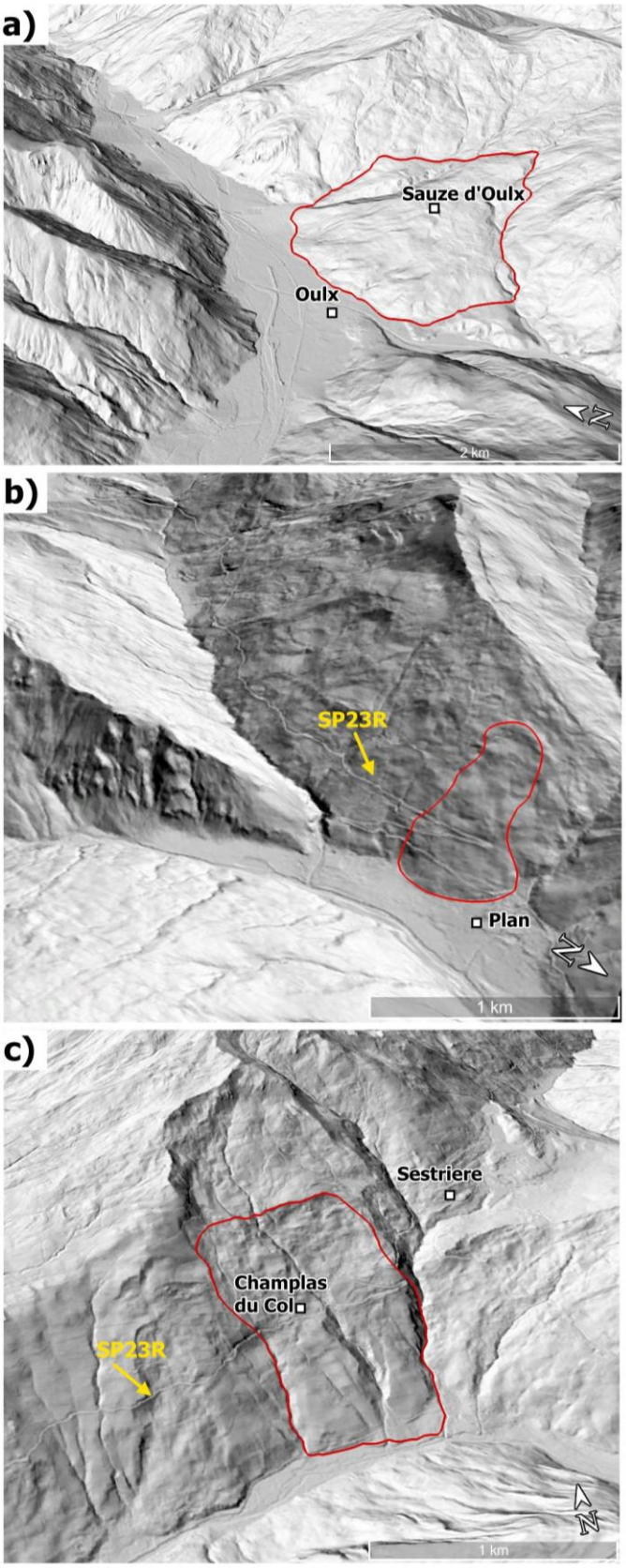

Figure 2.2 Topographic relief maps of the investigated landslides (red polygons): (a) Sauze d'Oulx; (b) Plan-Pragelato; (c) Champlas du Col–Sestriere.

2.2.2 Climate data

In order to evaluate climate patterns in the study area for the thirty-year reference period 1991-2020 according to the WMO, temperature and precipitation data for Piedmont region were considered. The dataset, the NorthWestern Italy Optimal Interpolation (NWIOI), provides daily data of maximum and minimum temperatures and precipitation with a time coverage from December 1957 until the day before the data download and it is updated daily by Arpa Piemonte. The domain covers the whole region (longitude 6.5-9.5 W and latitude 44.0-46.5 N), with a regular grid (0.125° resolution). For the purpose of the study, the period from 1 January 1991 to 31 December 2020 was selected and the data grids were processed by MATLAB® computational software to extrapolate cells covering area of the Dora Riparia and Chisone basins (see Appendix A). For simplicity, the western extremity belonging to France are neglected.

From the daily data, monthly values (mean for temperature and sum for precipitation) are calculated according to specific criteria, for which climate analysis requires the use of long series of quality-controlled, complete, and homogeneous data. The monthly normals are then used to calculate seasonal and annual normal (Fioravanti et al., 2022). The spatial mean of each cell value was then calculated from the clipped area to obtain a daily mean of precipitation and temperature, maximum and minimum, for the whole domain. Finally, the annual values of the two variables were obtained by evaluating the cumulative and mean of the daily data, respectively for precipitation and temperature. In order to better assess the presence of possible anomalies in the precipitation regime and to identify the wettest years, days with heavy rainfall greater than 10 mm were extrapolated from the dataset. This approach allowed to detect the pattern of intense meteorological events over the period 1991-2020 and, in the next step, to investigate possible accelerations in deformations trend under climatic conditions of the wettest years. On the other hand, the climatic pattern of temperatures over the thirty-year reference period is depicted, analyzing the deviations of annual mean temperatures from the reference normal, which is given by the average of annual temperatures in 1991-2020.

For the local-scale climate analysis of the sites, weather stations close to the landslides in both planimetry and elevation were considered. For case a), weather data are provided from the Chateau Beaulard station (1800 m a.s.l.), for case b) the Pragelato weather station (1525 m a.s.l.) and for case c) the Sestriere station (2020 m a.s.l.) (Figure 2.3). The database of the regional meteorological network can be found on the Arpa Piemonte geoportal.

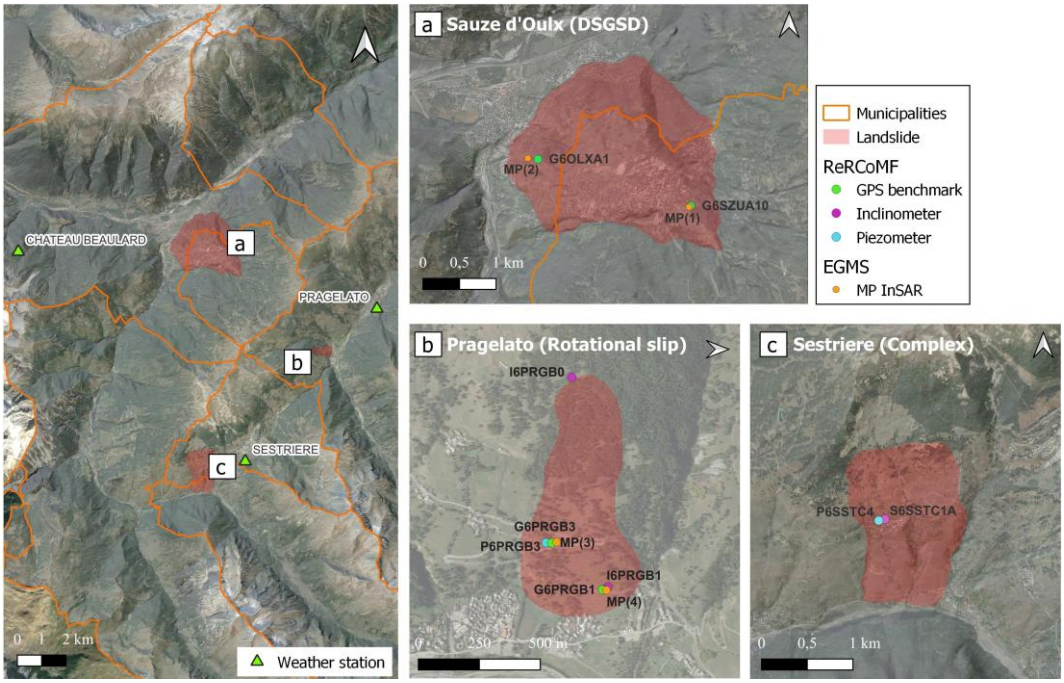

Figure 2.3 Details of the three sites with corresponding weather stations (left) and monitoring points.

2.2.3 Displacement monitoring

Since the 1990s, Arpa Piemonte has been monitoring about 220 landslide sites through the Regional Landslide Control Network (Rete Regionale Controllo Movimenti Franosi – ReRCoMF) for assessing time series of landslide displacements by using deep, shallow and strain gauge measurement points. The database of instruments distinguished by typology, functionality and technical characteristics of the installation is available in the geoportal and, such as landslide areas, the monitoring network can also be imported into a GIS environment.

Displacement measures acquired by Global Positioning System (GPS) benchmarks, inclinometers, and piezometers were analysed in this work. These data with related technical reports have been provided from Arpa Piemonte upon request. The choice of instrumental data used for the three case studies was guided in relation to a suitable time coverage for the period of interest. In addition, some site was discarded a few years after their installation and therefore not considered.

For instance, in the case of the landslides in Sauze d'Oulx and Sestriere, the GIS some inclinometers were active in 2002-2004 and several GPS stations have recently been installed, between 2017 and 2019, thus not useful for analysis. GPS data are processed for the Sauze d'Oulx and Pragelato landslides, while inclinometer data are considered for the Sestriere landslide. Furthermore, in support of the analysis, some additional information collected in the level II SIFraP report about the other instruments installed on the landslide body will be discussed. As it can be seen in Figure 2.3 the landslide areas and the distribution of monitoring points (Table 2.1) are shown.

Table 2.1 ReRCoMF monitoring instrumentation for the three case studies.

	ID code	Instrument	Date of installation	Reading frequency
1) DSGSD	G6OLXA1	GPS benchmark	2010/09	annual
	G6SZUA10	GPS benchmark	2008/09	annual
2) Rotational slip	G6PRGB1	GPS benchmark	2015/01	annual
	G6PRGB3	GPS benchmark	2015/01	annual
	I6PRGB0	Inclinometer	2004/08	semiannual
	I6PRGB1	Inclinometer	2012/11	semiannual
	P6PRGB3	Piezometer	2004/10	automated
3) Complex	S6SSTC1A	Inclinometer	2013/09	automated
	P6SSTC4	Piezometer	2004/09	automated

In cases a) and b), an integrated approach using satellite data was adopted, by comparing the information provided by Synthetic Aperture Radar Interferometry (InSAR) products with the GPS dataset. The joint analysis provided a comprehensive view of the deformation field of the landslide. An effective integration of monitoring data from different sources can be critical in reducing uncertainties, as individual monitoring techniques often have inherent limitations. Consequently, it can be difficult to achieve complete multi-parametric data coverage due to these isolated limitations (Carlà et al., 2019). The InSAR technique allows to monitor ground deformations and geological processes over extended areas, improving the conditions for slow-moving landslides detection (Cascini et al., 2010; Cignetti et al., 2024; Solari et al., 2019). SAR images are acquired by Sentinel-1 satellite since April 2014, which operates in C-band mode (wavelength of 5.6 cm) thus providing high spatial resolution data (Del Soldato et al., 2021).

Time-series deformations are available on the European Ground Motion Service (EGMS - https://egms.land.copernicus.eu/) open platform of the Copernicus service (Shahbazi et al., 2022) and in particular, for the aim of this work, ortho data which constitute the EGMS level 3 product (after basic and calibrated data) were considered. They are the result of processing satellite data acquired in ascending and descending trajectory and therefore provide information on vertical and horizontal (east-west) displacements with a constant revisiting time of 6 days from January 2016 to December 2021. Both components are available in raster format with spatial resolution of 100 m and also in vector points (Measurements Points, abbreviated as MP) referred to the center of the resolution cell. For the purpose of the analysis, only east-west displacements are considered for comparison with the horizontal component of the GPS station records.

2.2.4 Processing InSAR data

The method is based on a purely analytical approach, which is performed with MATLAB® and the open-source QGIS (version 3.28) software by processing

climate data and measurements of continuous landslide displacements. Starting from the analysis of precipitation regime over the thirty-year period 1991-2020, the rainiest years were identified in order to looking for a possible influence on significant accelerations during those periods in the landslide areas (Ardizzone et al., 2023).

For the cases of Sauze d'Oulx and Pragelato, a similar procedure is adopted, as already mentioned, which compares GPS and satellite data with the aim to overcome some limitations of these techniques. GPS is an optical instrument most commonly used for 3D surface displacement measurements. For the continuously operated mode, the accuracy of GPS measurement can reach the level of sub-centimeter, especially in the horizontal direction. Despite its precision, the limited availability of GPS measurements with a dense geographical distribution is a consequence of deployment constraints and high operational costs (Hu et al., 2014). Another drawback is related to the annual frequency reading which inhibits a detailed investigation of surface deformations over time and space; an aspect complemented by InSAR data that are extremely useful for landslide studies, since they grant millimeter accuracy due to short revisiting time. Moreover, InSAR techniques have more advantages: (i) good cost/benefit ratio; (ii) acquisition in all weather conditions and both day/night; (iii) data coverage of remote and inaccessible areas. Nevertheless, the interferometric approach is also affected by issues strictly related to (i) geometrical distortions between the LOS (Line of Sight) and the slope; (ii) atmospheric contribution and aliasing phase; (iii) the presence of snow, vegetation or variable land cover of the area, especially in the mountain environment (Del Soldato et al., 2021; Solari et al., 2020).

Given the above considerations, merging GPS and InSAR information should be cautious because of their complementary features. In order to carry out the displacement analysis for cases a) and b), it is necessary to make both datasets comparable at spatial and temporal scales, so the GPS benchmark falling within the raster cell (100 m) of the InSAR east-west mean velocity grid was considered. As the InSAR technique has an acquisition frequency of 6 days, the comparison is made by extracting from the satellite time series the daily data concurrent with the GPS acquisition date, which is annual. In this regard, time windows of the GPS and InSAR data exploited for the case studies a) and b) are shown in Table 2.2.

A distinctive methodology that excludes interferometric data, was employed to understand changes in displacement for the Sestriere landslide (case c), emphasizing the correlation between aquifer recharge processes following precipitation inputs and rise of displacements. In this case, the analysis focused on variations in piezometer recordings for the groundwater levels and inclinometer measurements for displacements.

Table 2.2 Temporal intervals of GPS and InSAR dataset for Sauze d'Oulx and Pragelato.

	Sauze d'Oulx	Pragelato
GPS (one measure per year)	14/06/2016 - 20/07/2021	15/07/2016 - 19/07/2021
InSAR (every 6 days)	05/01/2016 – 16/12/2021	

2.3 Results

2.3.1 Climate trends in the period 1991-2020

The rainfall and the temperatures pattern of the reference period 1991-2020 for the study area was investigated. The main purpose was to assess the evolution of climate factors, both long-term trends and inter-annual variability and extreme events.

The graphs below show the most interesting results obtained from the analysis conducted using the data provided by regular grids on Piedmont region, from which areas of the Dora Riparia and Chisone basins were extracted. The annual distributions of daily rainfall greater than or equal to 10 mm (Fioravanti et al., 2022) are shown and it can be deduced that the years with the most significant events are 2016 (with a value of 156.75 mm on 24/11/2016) followed by 2000, 2011, 2018 (Figure 2.4). The trend of the maximum daily rainfall, or rather the maximum annual rainfall, has also been plotted and shows a statistically significant increase.

Since the heaviest rainfall occurs in spring and autumn, the precipitation trend in these seasons were also investigated. Following the WMO guidelines for the calculation of normal climate values, the monthly cumulative precipitation was calculated from the daily values. As reported in Appendix A, seasonal precipitation was then determined by cumulating the monthly data (March, April, May for the spring season and September, October, November for the autumn season).

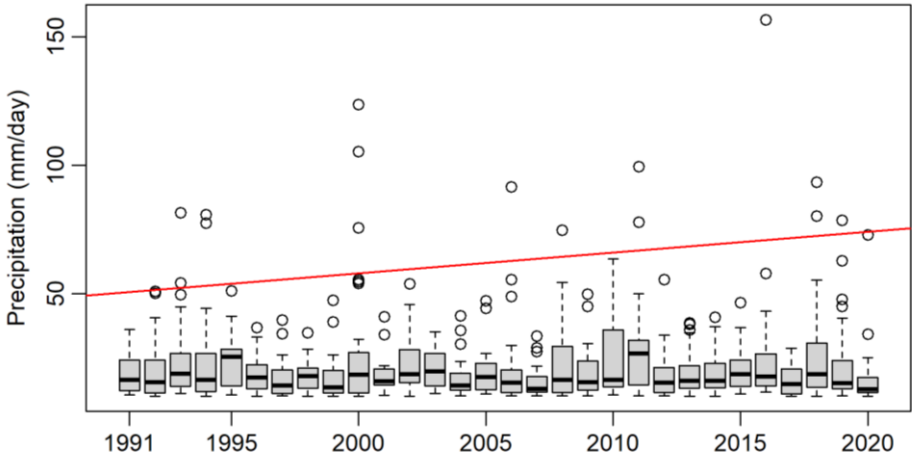

Figure 2.4 Annual distributions of daily precipitation greater than 10 mm in the period 1991-2020. Red line indicates the annual maximum values trend.

A similar approach is adopted for temperature regime. The maximum and minimum values were used to calculate the mean daily temperatures for the thirty years, from which the annual temperatures were derived for each year. Consequently, the resulting mean temperature over the period 1991-2020 is established as a reference value, and it is given as 7.5°C. Therefore, anomalies are evaluated by comparing the annual mean temperatures of each year to this value in order to identify meaningful deviations from the average. It can be observed how recent years have been increasingly affected by above-average temperatures (Figure 2.5).

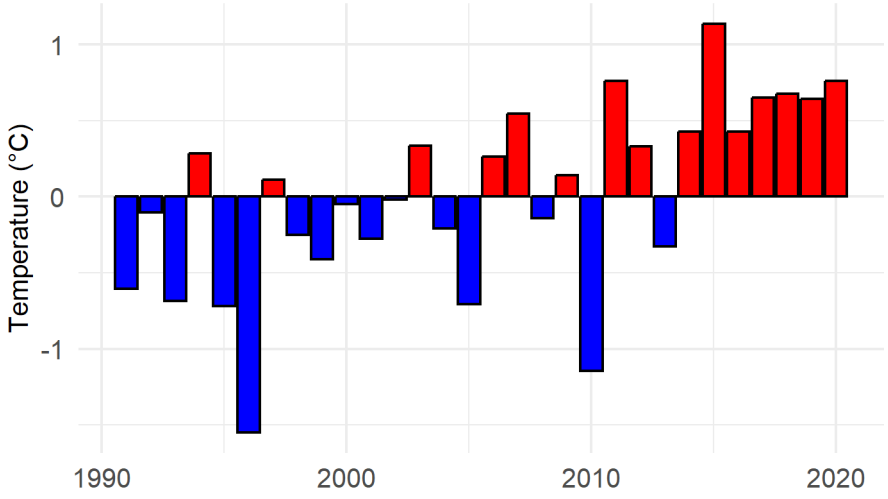

Figure 2.5 Annual mean temperature anomalies compared to the reference period 1991-2020.

The graphical results are consistent with the annual climate reports on temperature and precipitation for Piedmont region compared to the reference period 1971-2000. The reports state that 2016 and 2018 were among the wettest years and therefore investigated to develop the study, while 2022 was the hottest year in the entire dataset since 1958 (Arpa Piemonte, 2023d).

2.3.2 Influence on landslide displacements

The analysis of precipitation trends at the two basins scale has made it possible to identify the years affected by extreme events for which possible changing in movement trends can be investigated for the three case studies. Weather stations related to the sites are considered for a local scale analysis. For cases a) and b) in the graphs showing GPS and InSAR displacements trend, cumulative precipitation every 6 days are also depicted, having the same temporal resolution of the InSAR, to recognize possible accelerations or decelerations in the deformation time series following precipitation events.

a) The Chateau Beaulard weather station (1800 m a.s.l.) reported significant daily rainfall values during precipitation events that have affected Piedmont in recent years. In particular, 120 mm on 25/11/2016, 103.6 mm on 9/1/2018 and also the years 2019, 2020, 2021 with heavy autumn rainfall (Appendix A). Therefore, the state of activity the DSGSD focused on these periods was investigated coupling GPS and InSAR data. For the evaluation of the slope deformations, two MPs have been considered, since the displacement rate changes from the upper part of the landslide body to the bottom of the slope. In addition, these points have been identified to facilitate the comparison between the datasets obtained with the two techniques. Since G6OLXA1 does not fall in the InSAR values domain, because it is placed outside the raster cell, the nearest MP is considered for comparison. The MP(2) is located at a distance of 125 m from G6OLXA1 and therefore it can be considered reliable for the analysis (Figure 2.6).

The comparison analysis between GPS and satellite measurements confirms the trend of annual displacements in the order of 2 cm/year, as reported in the SIFraP sheet. In particular, the upper sector of the landslide, where the G6SZUA10 is located, moves at a speed of approximately 3 cm/year, unlike the G6OLXA1 located at the foot of the landslide body, which reports lower displacement rates. The InSAR data time series (Figure 2.7 and Figure 2.8Figure 2.**8**) show a similar trend (approximately 2 cm/year). Specifically, 19.39 mm/year for MP(1) (Table 2.3). While, at MP(2) the annual velocity is equal to 16.6 mm/year, confirming a lower displacement rate at the foot of the landslide body (Table 2.4). In both cases, the INSAR makes it possible to detect slight accelerations of movement close to the indicated precipitation events, which are not perceived by the GPS survey due to the temporal frequency with which it operates.

Table 2.3 Annual values of displacements (mm) at the Sauze d'Oulx DSGSD top.

	14/06/2016	**04/07/2017**	**17/07/2018**	**02/07/2019**	**21/07/2020**	**20/07/2021**
G6SZUA10	29	61	93	123	147	191
MP(1)	6.6	26.4	47.4	65.8	87	107.5

Table 2.4 Annual values of displacements (mm) at the Sauze d'Oulx DSGSD bottom.

	14/06/2016	**04/07/2017**	**17/07/2018**	**02/07/2019**	**21/07/2020**	**20/07/2021**
G6OLXA1	19	44	68	89	106	119
MP(2)	18.9	29.7	36	62.8	77.4	97.6

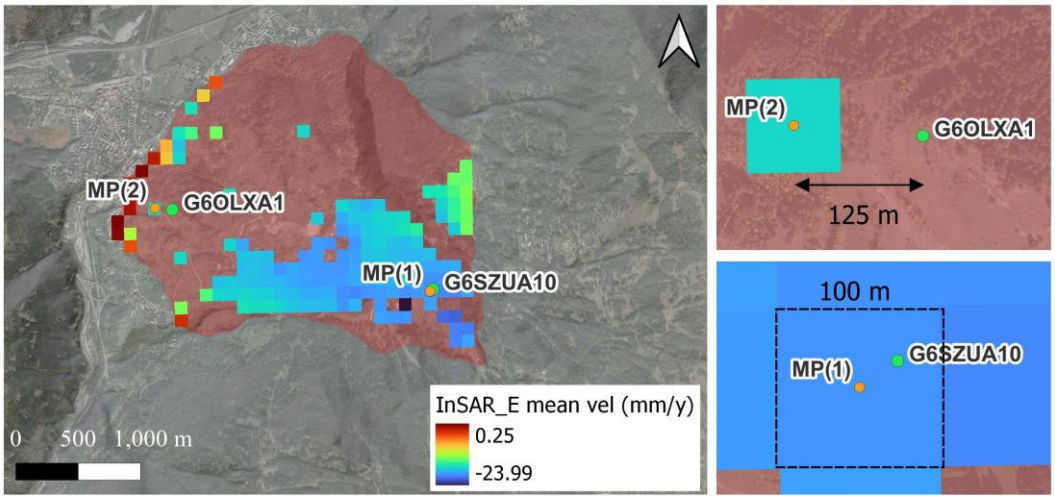

Figure 2.6 InSAR data coverage of DSGSD in Sauze d'Oulx. Negative velocity values indicate westward displacements, positive values indicate eastward displacements (left). The location of MPs and GPS marks is shown in detail (right).

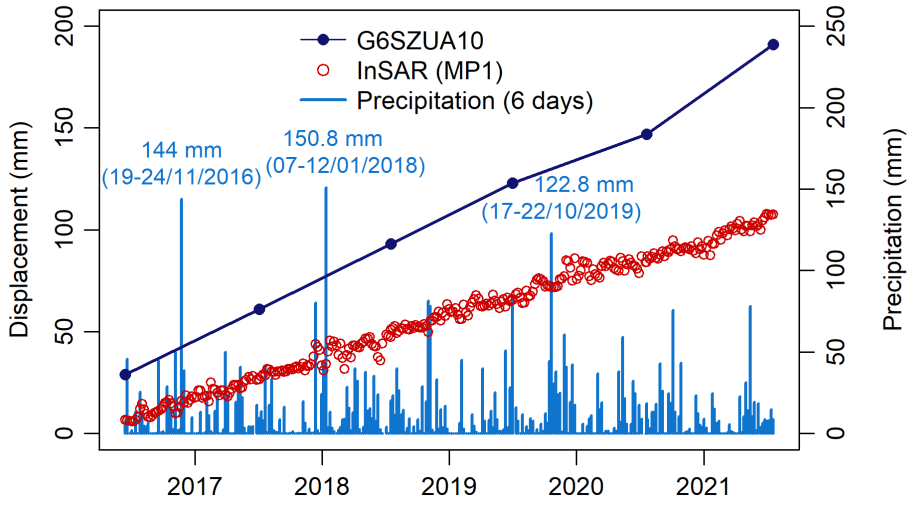

Figure 2.7 Displacements time series at the top of DSGSD in Sauze d'Oulx (modified by Narcisi et al. 2024).

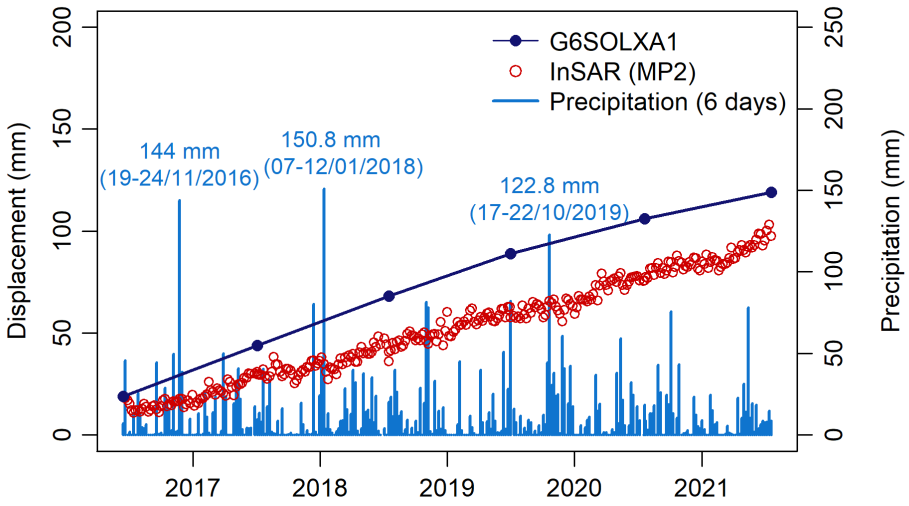

Figure 2.8 Displacements time series at the bottom of DSGSD in Sauze d'Oulx (modified by Narcisi et al. 2024).

b) The impact of the November 2016 event rainfall on displacement rates was also investigated for the Pragelato landslide (Appendix A). Again, it can be deduced that InSAR is more sensitive than GPS in extrapolating possible changes in deformation trends due to precipitation events. The GPS measurements report slow and progressive movements at the bottom (between 1 and 2 cm/year) as confirmed by InSAR mean values, showing eastward displacements (Figure 2.9). The G6PRGB1 and G6PRGB3 in the period 2016-2017 reported a displacement magnitude of about 2 cm, showing a relevant acceleration of the movement, probably correlated with heavy precipitation occurring.

In addition, significant accelerations were also detected by G6PRGB3 in 2018 and 2019 with a displacement since the last reading of 2.9 cm and 2.4 cm respectively, due to heavy rainfalls in the spring and autumn of 2018. In Table 2.5 and Table 2.6 measures from GPS are reported and compared with InSAR at the MP (18.2 mm/year for MP(3) and 12.2 mm/year for MP(1)), while in Figure 2.10 and Figure 2.11 it can be noticed the pattern of displacements time series.

Table 2.5 Annual values of displacements (mm) in the upper sector of the Pragelato landslide.

	15/07/2016	**10/07/2017**	**23/07/2018**	**18/07/2019**	**24/07/2020**	**19/07/2021**
G6PRGB3	16	36	65	89	100	108
MP(3)	2.6	26.8	47.1	66.9	87.1	95.9

Table 2.6 Annual values of displacements (mm) at the bottom of the Pragelato landslide.

	15/07/2016	**10/07/2017**	**23/07/2018**	**18/07/2019**	**24/07/2020**	**19/07/2021**
G6PRGB1	12	20	27	31	36	34
MP(4)	11	24.2	41.11	49.9	64.2	66.8

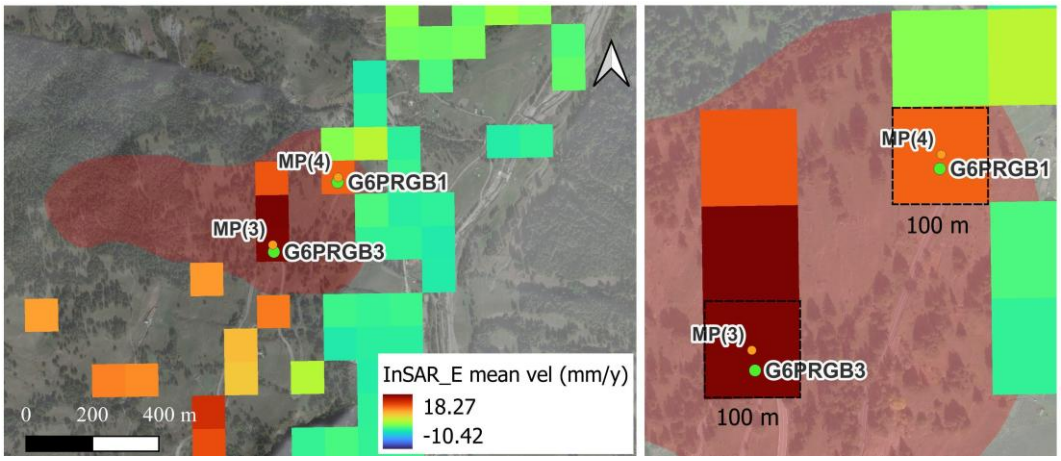

Figure 2.9 InSAR data coverage of landslide in Pragelato. Negative velocity values indicate westward displacements, positive values indicate eastward displacements (left). The location of MPs and GPS marks is shown in detail (right).

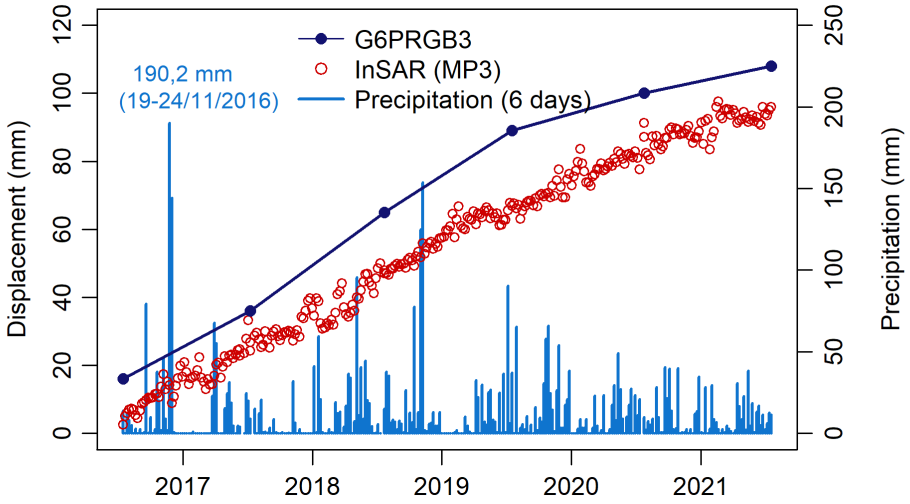

Figure 2.10 Displacements time series at the top of landslide in Pragelato (modified by Narcisi et al. 2024).

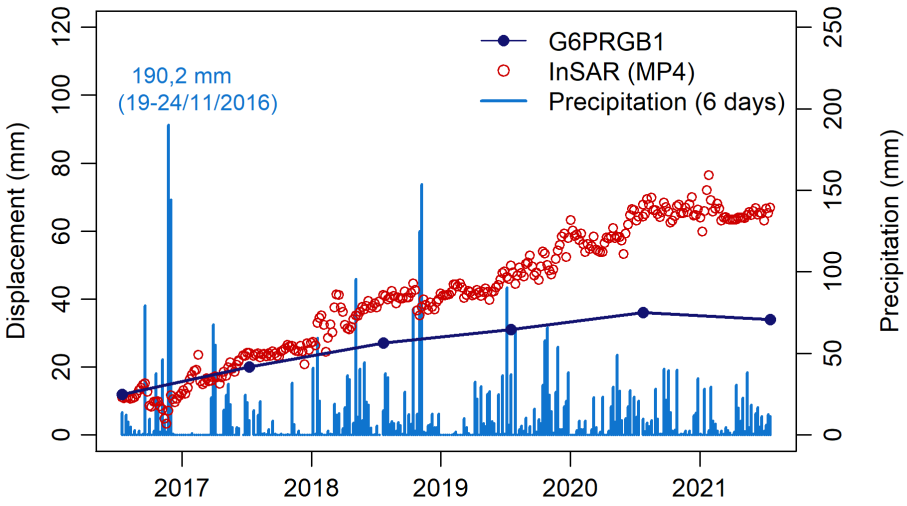

Figure 2.11 Displacements time series at the bottom of landslide in Pragelato (modified by Narcisi et al. 2024).

c) The complex landslide located at Champlas du Col is characterised by a movement rate of a few cm/year, varying with depth, with significative accelerations in the spring period due to snow melting as reported by Arpa Piemonte. In this case study, the daily displacements recorded by the fixed-probe inclinometer S6SSTC1A were considered. The inclinometer detects two surfaces (at depths of 18 and 30 meters) with movement rates of even more than 4 cm/year (2013-2017 period). The shallowest deformations are more circumscribed but particularly active phenomena and at high risk since their acceleration can involve built-up areas and roads. Accordingly, the analysis focuses on the displacements recorded by the 18 m probe, computing the average seasonal displacement over the 2014–2022 period (Table 2.7).

Snow coverage and groundwater level trends since 2014 have also been examined in support of the analysis (Appendix A). It has been proven that the greatest displacements occur in spring (3.43 mm), coinciding with the period of snowmelt which contributes to the increase of groundwater level. For instance, in the spring 2018 (Figure 2.12), the inclinometer recorded a significant displacement increase of approximately 5 mm, probably due to the abundant snowfall during the winter (maximum of 196 cm).

Table 2.7 Mean seasonal displacements over the period 2014-2022 for the Sestriere landslide.

	Autumn	**Winter**	**Spring**	**Summer**
S6SSTC1A (18 m)	1.11	1.58	3.43	2.00

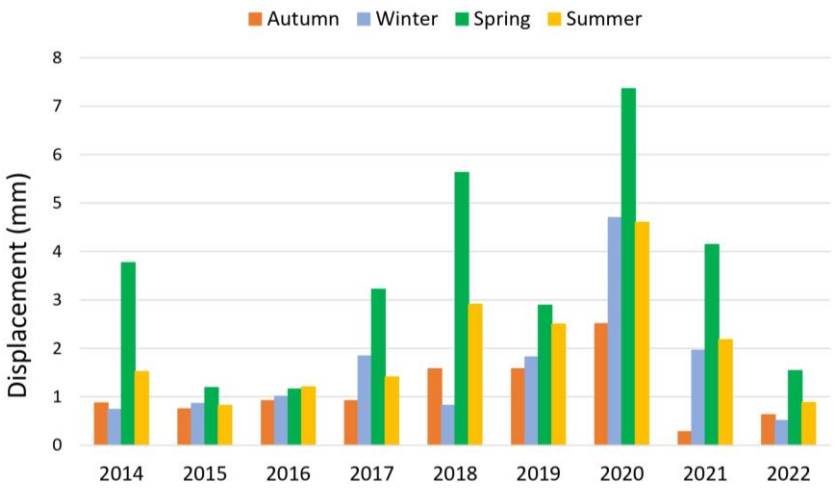

Figure 2.12 Seasonal displacements (2014-2022) recorded by the inclinometer S6SSTC1A for the Sestriere landslide.

In order to better assess the interannual variability of displacements during the spring season and to highlight potential anomalies, the full dataset from 2014 to 2024 was considered. This 10-year period was adopted as a suitable reference window for analysing variations in spring movements (cumulative values from March to May) due to comparable changes of the influencing factors. However, the direct comparison of multiple time series, characterized by distinct units and magnitudes, can lead to misinterpretation. To mitigate this problem, it is advisable to supplement visual analysis with a statistical approach that standardises the data. One method is to normalise the time series by subtracting the mean from each value and dividing it by the standard deviation, in order to obtain standardised values (z-score) with a mean of 0 and a standard deviation of 1 (Figure 2.13).

In order to associate potential displacement anomalies with hydro-meteorological forcings, the same approach was applied to (i) winter temperature (January–March), as warmer winters can significantly accelerate and intensify the snowmelt process; (ii) cumulative snowfall (November-April), which increases the available water supply for meltwater recharge and (iii) spring rainfall (March–May), as it can contribute to rising groundwater levels. Significant displacement anomalies occurred in 2018, 2020 and 2024, due to significant snow accumulation and warmer winter conditions. Conversely, negative anomalies (e.g. in 2015–2016 and 2022–2023) correspond to comparatively reduced snowfall and limited recharge.

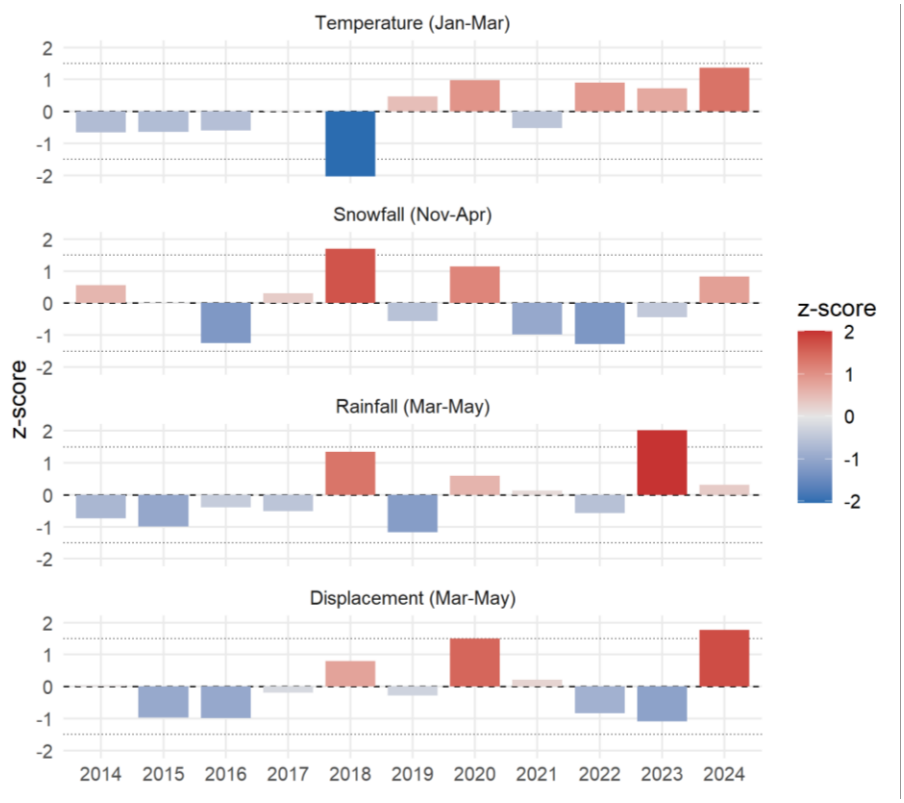

Figure 2.13 Standardised (z-score) interannual variability of hydro-meteorological factors and spring displacements for the period 2014–2024.

2.4 Discussion

The assessment of the climatic variables time series in the Dora Riparia and Chisone basins revealed heavy precipitation occurrence and rise of temperatures starting from a first general evaluation of climatic pattern of the area, which have resulted in accelerations for landslides investigated as confirmed by monitoring instruments.

For the purpose of the study, the geological and morphological conditions predisposing the area to slope instability were evaluated in a preliminary analysis, resulting in a significant level of landslide hazard for the Western Alps. The three case studies selected belong to this framework, all of which are being monitored as they are affected by slow but persistent movements over time and involve built-up areas and infrastructure. The choice of monitoring network instruments was guided not only by the availability of long and gap-free time series, but also by the typology of gravitational phenomenon to be investigated. In support of field observation, the contribution of satellite data is emphasized for the detection of slow-moving ground processes, thus identifying significant changes in the time series displacement under extreme rainfall events. However, due to the approach chosen, it should be emphasised that any acceleration or changes in the InSAR time series cannot be correlated certainty with to the effects of the precipitation event, but may be due to radar acquisition errors. This is because the proposed approach is very simplified and is intended to provide a preliminary guide for future studies. The joint

combination of in situ and remote sensing techniques, such as GPS and InSAR, enables the comprehension of the deformation field of the landslide, which could be imperceptible when it comes to slow surface movements.

In the case of the DSGSD in Sauze d'Oulx, being a very large and complex landslide body, there have been different displacement rates at the top and the bottom of the slope over the years. It is among the most important DSGSD in the area and it has been monitored for more than twenty years due to its not negligible acceleration (2-3 cm/year). Therefore, rates of movements recorded by GPS benchmark G6SZUA10 and G6OLXA1 located at different elevations were analysed and supplemented by InSAR data, which provide a more detailed temporal resolution. The investigation time window starts in 2016, the year from which the InSAR data are available, with the aim to assess the possible responses of the displacements trend after the exceptional rainfall event occurred in November 2016. The comparison between GPS and InSAR acquisitions is based on a simplified approach which neglects measurement discrepancies due to the poor coverage on the landslide slope of Sentinel-1 data. Moreover, this type of analysis focuses on surface deformations, excluding the displacements in depth at the sliding surface, which must instead be analyzed with inclinometer. The displacements measured by inclinometer probes were not considered as most of them were discarded after only a few years of monitoring activity and therefore not useful for analysis purposes. However, the Arpa Piemonte reports state that the manual inclinometer I6OXA3 (active since 2001), with quarterly reading, recorded a remarkable movement increase between July and December 2016, with 2018 as the year of greatest acceleration, and also during the second half of 2020. This information supports the displacement rates recorded by GPS benchmarks during the wettest periods investigated.

For the Pragelato landslide, the same method based on GPS and InSAR data was adopted, identifying the benchmarks that fall within the Sentinel-1 product raster cell. As in the case of Sauze d'Oulx, possible accelerations of displacements since 2016 have been investigated due to the occurrence of significant precipitation events. The demonstrated effectiveness and adaptability by integrating GPS and InSAR, coupled with the accessibility of free data from EGMS, as well as the possibility of solving some limitations of these techniques through their combination confirm its performant use in several applications (Del Soldato et al., 2021). The landslide in Pragelato moves with speed about few cm/year. The Arpa Piemonte reports state that manual inclinometer measurements conducted at the top (I6PRGB0) and at the foot of the landslide body (I6PRGB1) show almost constant and extremely slow movements, with the exception of the 2016-2017 period with greater displacements as confirmed by G6PRGB3 measures. At the end of the 2016, the piezometer P6PRGB3 recorded significant groundwater increases following heavy autumn rains.

Finally, for the Sestriere landslide, the displacement patterns were investigated by considering the impact of snowmelt and precipitation on the fluctuations of the water table. Therefore, inclinometer S6SSTC1A data were processed from its installation, analyzing the displacements occurred over the seasons in the period

2014-2022. It was found that significant displacement increases occur in spring, particularly relevant are the ones recorded in 2018 and 2020. In support of the analysis, the Arpa Piemonte reports state that piezometer P6SSTC4 (see Appendix A) recorded an increase of the groundwater level of approximately 5 metres in spring 2018 (from -13.07 m on 4 March to -8.71 m on 10 May), probably due to heavy precipitation in May 2018 and as a consequence of rising temperatures in the previous year. Such conditions could have contributed to the observed acceleration of landslide movements.

2.5 Conclusion

In the present study, an analytical approach was proposed to investigate the impact of the climatic anomalies of temperature and rainfall compared to the reference period 1991-2020, on the degree of activity of three slow-moving landslides.

However, since climate change is still an open issue for its complexity, no absolute and reliable interpretation has yet been provided. Consequently, it becomes equally difficult to interpret the response of the kinematic mechanisms of landslides to the occurrence of extreme events. For this reason, a number of researchers have analyzed historical records of landslides by attempting to compare them with climate variables, especially precipitation and temperature. In general, the studies reveal a wide range of influences and consequences of climate change on landslides, including contradictory, uncertain and undetermined effects.

The methodology proposed in this chapter constitutes a simplified approach that suggests the use of different tools and available data in order to clarify as much as possible the complexity of this scenario. Furthermore, statistical analyses and geotechnical slope modelling could be employed to supplement surface deformation detection.

Chapter 3

Spring levels in slow-moving landslide displacement

The work described in this chapter has been partially derived from (Narcisi et al., 2026).

3.1 Introduction

Acceleration phases in slow-moving landslides are typically triggered by groundwater forcing, which is commonly linked to prolonged infiltration from intense rainfall or snowmelt. This leads to elevated pore-water pressures, reduced effective stress on discontinuities and increased deformation. These dynamics may develop gradually across seasons or episodically during anomalously wet years (Toločka, 2025). Given the amount of available meteorological data, groundwater depth measurements and continuous time series of monitored displacements, the definition of a data-driven model capable of statistically estimating the deformation response to changes in the main triggering factors may be useful.

Several authors have conducted researches to assess the effects of precipitation and groundwater flow regime on landslide reactivations. Lacroix et al. (2020) and Bordoni et al. (2023) reviewed the environmental conditions of landslide-prone regions and the forcing factors such as precipitation, earthquakes and human activities that drive movements, and discussed the circumstances under which slow-moving landslides can accelerate rapidly or fail catastrophically. Bernardie et al. (2015) introduced a statistical-mechanical approach to predict changes in landslide displacement as a function of pore water pressure, which influences soil shear strength along the sliding surface (Conte & Troncone, 2011). Indeed, the positive pore pressure due to the rising groundwater level is considered the main mechanism leading to failure in hydrologically induced deep-seated landslides, implying that water content controls the behaviour of slow-moving landslides (Prokešová et al., 2013; Van Asch et al., 2007). Matsuura et al. (2008) investigated the relationship between rainfall, snowmelt and pore water pressure increases over time and correlating them with landslide displacements.

Similarly, the Fourier spectral analysis has been effectively applied in numerous research fields, for monitoring environmental seismic noise datasets (Colombero et al., 2018), to quantify groundwater level fluctuations in terms of

frequency (Joelson et al., 2016), in landslide susceptibility mapping (Bao et al., 2022; Hoseinzade et al., 2022) and hydrology, demonstrating its potential for modelling and predicting precipitation patterns (Laguardia, 2011). The hydrogeological and geomechanical properties of slopes under rainfall conditions have been extensively investigated, with important contributions by Huang et al. (2012) and (Pecoraro & Calvello, 2021) in the monitoring of pore pressures and the development of warning systems. The role of thresholds in supporting these systems has been emphasized by (Segoni et al., 2015) and (Berti et al., 2012) who developed probabilistic methods to assess rainfall thresholds for landslide occurrence, providing more accurate and statistically rigorous prediction models.What is still missing, at least to the best of the authors' knowledge, is the ability to use spring water level, an important indicator of aquifer dynamics (Kresic & Stevanovic, 2010), as a powerful tool for detecting slow-moving landslide displacements and establishing thresholds useful for early warning or risk reduction (Pecoraro et al., 2019).

In this framework, by collecting groundwater level and landslide displacement time series, this work aims to improve understanding of the hydrogeological factors influencing slow-moving landslides, focusing on two large slow-moving landslides in the Susa Valley (Champlas du Col and Thures). As precipitation is often the main preparatory factor, it is important to quantify the recharge mechanisms and consequently the effects on displacement trends. Using this approach, the displacements trend could be described from the groundwater level, bypassing the precipitation input data.

Given these assumptions, the performed analysis follows these main steps: (i) understanding the dynamics of aquifer by detecting spring hydrometric data with autocorrelation function and assessing the system response to rainfall through cross-correlation analysis; (ii) application of the Fourier Transform to water level and displacement data to detect possible periodicity of signals and clarify whether the spring can reasonably represent the effects of groundwater fluctuations on landslide acceleration; (iii) detection of anomalies in the landslide acceleration patterns in the meaning of significant groundwater level rising.

3.2 Champlas du Col and Thures landslides

The two sites (Figure 3.1a) are characterised by intense fracturing of the rock mass, which allows the development of a complex network of water outlets, with supply sectors in the highest areas of the slopes. The presence of intense and widespread water circulation within the rock mass is manifested on the surface by numerous springs, mainly distributed in the lower-middle part of the contact between landslides or glacial deposits and the bedrock or rock mass. These springs are generally characterised by modest discharge and, in some cases, are subjected to significant variations in flow rate due to the seasonality of the inflow from the recharge zone. The Cordeminas and Thures springs are actually spring intakes,

where groundwater is collected into a chamber with a cement basin, as shown in Figure 3.2c.
The two case studies are noted as: (i) Champlas du Col landslide and (ii) Thures landslide, whose simplified cross-sections are shown in Figure 3.1c-1d. Some representative views of both sites are shown in Figure 3.2.

i) A preliminary overview of the site has been already provided in the Section 2.2.1. A schematic geological section of the landslide was defined using available borehole data and geological documents provided by the Regional Agency for the Protection of Environment (ARPA Piemonte - Banca Dati Geotecnica) to reconstruct the stratigraphy. The stratigraphies obtained from the various surveys prove that the upper soil layer consists of highly fractured calcschist embedded in a silty sand matrix. This clearly indicates the presence of deep movements causing the degradation of the bedrock. Previous analyses have recognized a complex system with several sliding surfaces, attributed to the presence of a highly fractured and disjointed rock mass, a factor that contributes to the infiltration of meteoric water inputs. Moreover, the existing borehole C1, was used to install the S6SSTC1A inclinometer.
As evidenced by the SCC3 borehole, in the lower part of the slope, the presence of fluvial deposits at a depth of 79-89 m indicates that the landslide advanced along a sliding surface below the existing valley floor. Upstream of SP23R, movement occurs along horizons of different permeability due to the presence of gravel alternating with silt and sand. Given the shallow depth of the boreholes (maximum 100 m), the thickness of these incoherent soils along the slope was roughly estimated. From a hydrogeological point of view, the landslide body hosts an aquifer characterised by the prevalence of glacial deposits which, subject to consolidation phenomenon, reduces the overall permeability (Fontan, 2022).
In the context of the DSGSD, the specific case of the Champlas du Col reveals the typical characteristics of rock flows. Here, the slope collapse is dominated by a visco-plastic deformation component, with creep movements distributed over a large part of the rock mass. This results in a dominant sliding component along different planes on structural discontinuities (Fioraso & Mosca, 2014).

ii) The Cima Bosco Complex Landslide (CBCL), so called because it extends on the hydrographical right slope of the Thuràs Valley from the top of Cima Bosco (2350 m a.s.l.), is located in the municipality of Cesana Torinese, in the Thures locality (1670 m a.s.l.). The entire west-oriented slope of the Cima Bosco mountain is affected by a DSGSD covering an area of 4.27 km^2. The deformation is mainly concentrated along well-defined discontinuities, which cause the movement of rock masses towards the valley floor (Fioraso & Mosca, 2014) Within this area, it is possible to distinguish a main shallow landslide body (Figure 3.1d) from a deeper bedrock layer (first 10-20 m), consisting of overlying formations such as eluvial-colluvial products, glacial and alluvial deposits in flat conoids. The CBCL has a well-developed surface hydrographic network in its distal sector, associated with the groundwater table. This hydrographic system is sustained by the main landslide

body, which, despite its loosened and disarticulated structure, is characterized by a low permeability due to the presence of the abundant silt-clay matrix. The stratigraphy derived from some surveys carried out at the site reveals the presence of fractured calchscists corresponding to the sliding surfaces identified by the inclinometer near Thures.

Based on all available evidence, the aquifer supply is primarily superficial (Alberto et al., 2008; Arpa Piemonte, 2024a). Stratigraphic findings further suggest that the sliding plane lies below the groundwater table. Water accumulation in this sector may increase pore-water pressure, leading to failure within the rock mass and as well as active landslide processes.

Field observations and monitoring (using inclinometers and SAR-PS techniques) show slow and non-homogeneous movements (about 10 mm/year), which have caused some damages to the buildings in Thures.

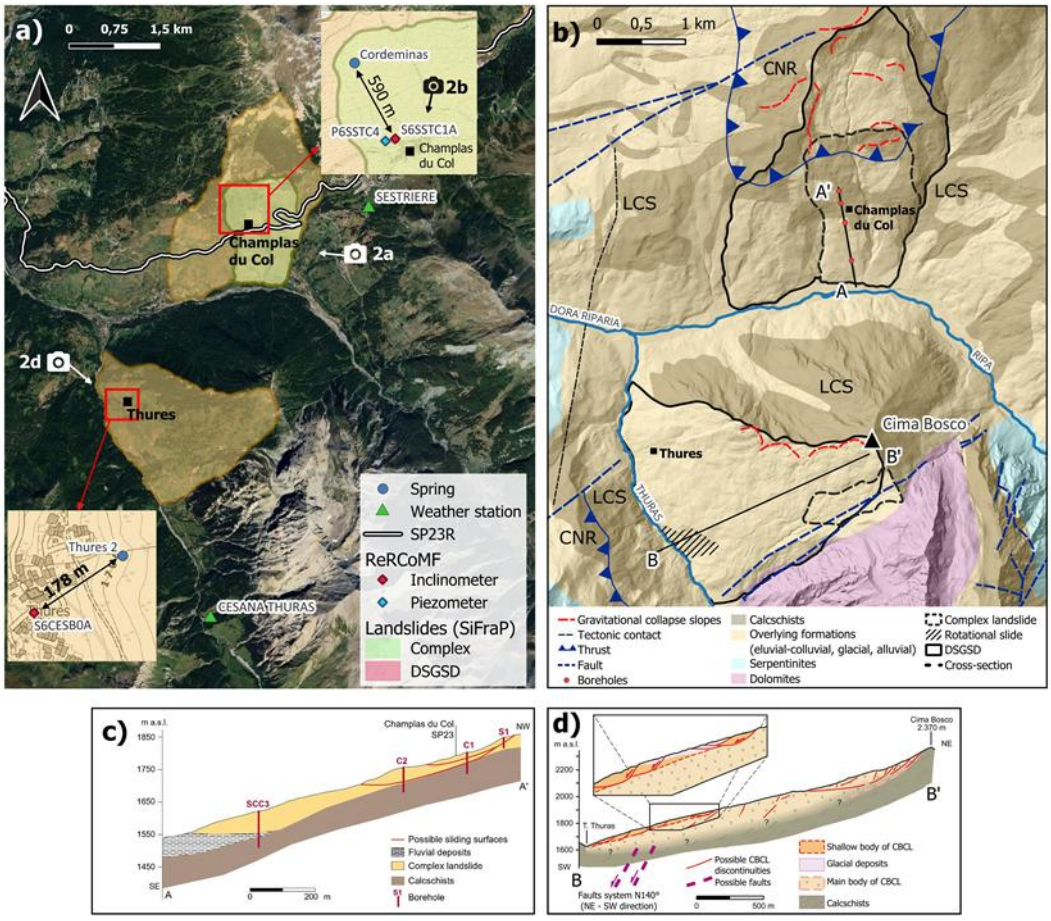

Figure 3.1 (a) Study area and location of (i) Champlas du Col and (ii) Thures landslides; (b) Geological map (modified by FOGLIO 171 (Servizio Geologico D'Italia, 2014); (c) Simplified cross-section of the Champlas du Col landslide (created using AutoCAD® 2024); (d) Geological cross-section of the Thures landslide site (modified after Alberto et al. 2008)

3.3 Materials and methods

3.3.1 Data collection

The water springs ("Cordeminas" and "Thures 2" drawn as blue dots in Figure 3.1a) are monitored by ARPA Piemonte in collaboration with the Applied Geology research group at the Department of the Environment, Land and Infrastructures Engineering (DIATI) of the Politecnico di Torino. Multiparameter CTD probes were installed at the Cordeminas spring (since 2020) and Thures 2 spring (since 2017). Both springs, which are actually spring intakes, are collected within small cement basins to measure electrical conductivity (EC), temperature (T) and water depth (D), hereafter referred to as water level, with an hourly time step (Bonomo, 2023). The analysed dataset is updated to the measurement campaign conducted in December 2024 (Table 3.1).

The water level time series were compared with precipitation data to investigate possible impacts on groundwater springs. Precipitation data were obtained by selecting available weather stations from the official ARPA Piemonte regional network. The choice of these weather station was based on the following criteria: i) proximity to the investigated site, ii) comparable topographical altitude, iii) same exposure and iv) continuity of the time series. The Sestriere and Cesana Torinese weather stations met these criteria (Figure 3.1a and Table 3.1). To ensure consistency between spring and weather datasets, the hourly water level data were transformed into average daily values.

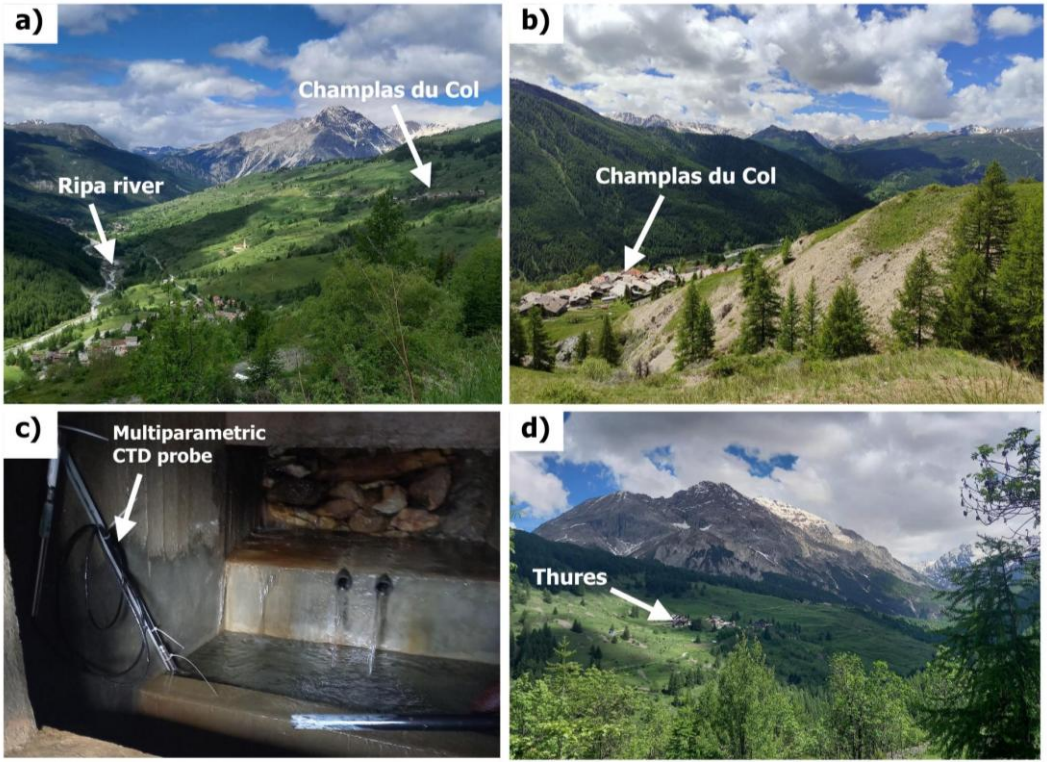

Figure 3.2 (a) Champlas du Col slope from the eastern side (b) Counterscarp on Champlas du Col landslide body (c) Spring cement basin with multiparametric CTD probe (d) View of Thures from the opposite slope (see Fig. 3.1a for pictures location).

Table 3.1 Monitoring network and available datasets for (i) Champlas du Col and (ii) Thures landslide.

Site	Spring	Elevation (m a.s.l.)	Weather station	Elevation (m a.s.l.)	Distance (km) spring - weather station	ReRCoMF		
						ID code	Instrument	Period
(i) Champlas du Col	Cordeminas (17/10/2020-09/12/2024)	1960	Sestriere (since 1996)	2016	2.2	S6SSTC1A	Inclinometer	2013/09 - 2024/11
						P6SSTC4	Piezometer	2004/09 - present
(ii) Thures	Thures 2 (19/10/2017-09/12/2024)	1700	Cesana Thuras (since 2002)	1902	3.7	S6CESB0A	Inclinometer	2012/10 - present

Spring and precipitation data were compared in order to analyse the groundwater level variations and available deep displacements dataset from the already installed monitoring system to detect any correlation with acceleration phases in the landslide deformation trends. As described in the previous section, the two sites (Figure 3.1a and Table 3.1) have been equipped with traditional and automatic fixed inclinometers and piezometers (ReRCoMF monitoring network). These data with related technical reports have been provided from ARPA Piemonte upon request.

Analogous to the choice of weather stations, only useful instruments with large and continuous datasets. Therefore, inclinometers without automatic acquisition were excluded, and only fixed probe inclinometers, which provide daily cumulative displacement values from the installation date, were considered. The S6SSTC1A and S6CESB0A inclinometer probes intercept the main sliding surface at depths of 18 m and 22.5 m respectively.
Both sites have more than 10 years of available data, with the exception of the S6SSTC1A inclinometer, whose fixed probe was removed in November 2024 due to pipe damage caused by high movement rates of the landslide body during the previous spring season. For the following analyses, data recorded after 10 June 2024, for the Champlas du Col landslides, were neglected in the comparison with other considered parameters.
The piezometers record daily depth to groundwater levels, reflecting changes in the hydraulic head of the aquifer, and therefore can be useful in supplementing the spring measurements to detect groundwater fluctuations. For the Champlas du Col site, piezometric data were included in the analysis of landslide accelerations due to the proximity of the instrument to the inclinometer. Conversely, at the Thures site, the piezometric dataset was neglected, both due to its limited length, as the existing piezometer was installed in 2019, and because the spring is located very close to the inclinometer considered in this study.
For all datasets, a correction of time series and filling of short gaps using interpolation was applied where necessary, as shown in Figure 3.3.

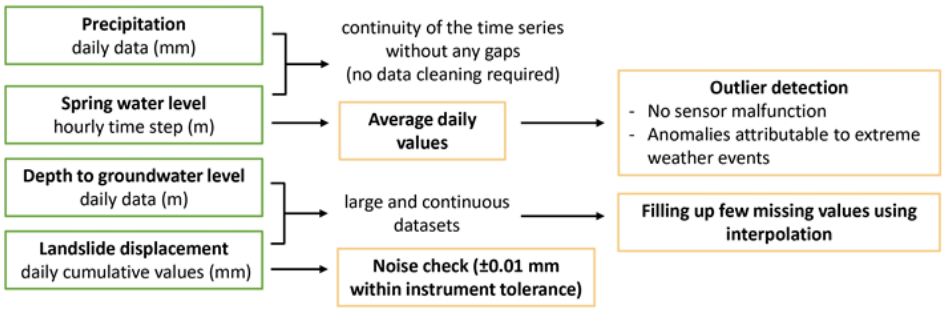

Figure 3.3 Schematic framework of data pre-processing.

3.3.2 Autocorrelation and cross-correlation analysis of spring hydrometric data

Statistical analyses were carried out to describe the spring system behaviour over the hydrological years, a crucial step for the comprehension of possible effects on changes in landslide displacement trends. The proposed approach aims to reproduce the preliminary analysis steps that can be implemented within the SOURCE tool (Gizzi et al., 2023; Lo Russo et al., 2021), which is useful for a semi-automatic hydrogeological characterisation of aquifers supplying the monitored springs. In this work, the SOURCE methodology has been customized to the analysis purposes

and improved for assessing the structure of time series and the presence of cyclical components.

For both springs, the Autocorrelation Function (ACF) was applied to the water levels to determine the possible existence of memory in the recorded signal and to identify potential stationarity (Sapone, 2023), as well as the vulnerability of the aquifer system under dry and wet conditions. As mentioned in the introduction, the ACF is a univariate method which evaluates the temporal reciprocal influence on subsequent data of a single dataset. In practice, it quantifies the correlation between observations of a time series at two points in time, separated by a specific lag time (τ). The ACF for a lag τ corresponds to the covariance of all measurements x_t and measurements with a time distance $x_{t+\tau}$, according to the following equation (Lo Russo et al., 2021):

$$cov\tau = \frac{1}{n-\tau}\sum_{t=1+\tau}^{n} x_t x_{t-\tau} - X_t X_{t-\tau} \qquad (3.1)$$

where *x* is the time series, *n* is the number of measurements in the time series, *t* is the time (days), τ is the time distance between two measurements, and *X* is the average value of the sample. The ACF function always assumes values between -1 and 1, and particularly for τ = 0, ACF = 1, which indicates a perfect linear correlation with itself. Therefore, the graph of the ACF always has a value of 1 at the origin (i.e. at lag = 0). When using the ACF on hydrological data, a slow decline of ACF curve in the graphical output indicates an aquifer characterised by poor draining properties, low permeability or significant groundwater storage. Conversely, a fast decline indicates a more rapid flow of water through the aquifer or limited storage capacity, which could be characteristic of a karst aquifer (Lo Russo et al., 2021).

Besides, the bivariate method of the Cross-Correlation Function (CCF) was performed to identify potential connection between input (daily rainfall) and output time series (daily spring water level) and to obtain information about the time delay at points of maximum similarity (Amanzio et al., 2015). Cross-correlation analysis is based on an equation similar to the ACF as it depends on the time interval k between the individual values in the series. If two-time series are marked as variables *X* and *Y*, and *n* is the number of pairs that are compared in one step *(k)* of the CCF, the cross-correlation coefficient can be obtained by the following (Box et al., 1974):

$$R_{xy}(K) = \frac{n\sum XY - \sum X \sum Y}{\sqrt{[n\sum X^2 - (\sum X)^2] \times [n\sum Y^2 - (\sum Y)^2]}} \qquad (3.2)$$

This coefficient can range between -1 (perfect negative correlation) and +1 (perfect positive correlation); a value of 0 indicates no correlation.

As with the ACF, the CCF is an established technique that is usually applied to Q and P datasets. However, the CCF can also assess T and EC datasets in relation to

precipitation, and such analyses could be used to validate hydrogeological considerations of the time lag response and maximum Rxy(K) values (Lo Russo et al., 2021).

3.3.3 Power spectral density

The trend and magnitude of landslide movements in relation to the recharge regime of the groundwater system was examined.
The evaluation of the periodogram was carried out to identify possible dominant periodicities in the groundwater level and displacement time series. Before this step, a preliminary analysis of the inclinometer data was required because the cumulative displacements recorded since the installation date of the instrument are plotted as a monotonically increasing curve, which does not provide comprehensive information on variations in landslide displacements over time. Given the typical long-term evolution of slow-moving landslides, the daily displacement for both sites is very low (< 0.05 mm), but conversely, more significant displacement rates can be observed over a larger time window. Therefore, the cumulative values were processed by considering the displacement rates over a 30-days moving time window, using the following expression:

$$v_t = \frac{d_t - d_{t-30}}{30} \qquad (3.3) \qquad t=1, 2,\ldots,N$$

where d_t is the displacement value on day t, N is the total number of daily displacements, v_t is the displacement rate.
This approach enables the comparison of daily water levels with displacement values, providing a preliminary overview of any potential correlation between the rise in water levels and the landslide accelerations.
A periodogram is an estimate of the Power Spectral Density (PSD) of a signal and it is mathematically related to the autocorrelation sequence r_{xx} by the discrete-time Fourier transform (Oppenheim et al., 1999). This function provides a representation of the spectral components of the parameters in terms of frequency:

$$P_k(\omega) = \frac{1}{2\pi} \sum_{m=-\infty}^{+\infty} r_{xx}(m)\, e^{-j\omega m} \qquad (3.4)$$

where ω is $2\pi f/f_s$, f is the physical frequency and f_s the sampling frequency (Fiorillo & Doglioni, 2010).
Fourier analysis assumes signal stationarity, which can limit its performance when time series are affected by extreme or transient events, such as the spring water level, groundwater level and displacement signal analysed here. However, the PSD provides an averaged representation of the spectral content, which is suitable for identifying dominant periodicities in the dataset, even though it does not fully capture transient or evolving frequency responses associated with short-term disturbances. In this sense, the PSD allows the identification of recurrences in the

analysed datasets, from which e of the coupling between slope deformations and groundwater fluctuations can be inferred (Priestley, 1981).

3.3.4 Detection of landslide acceleration anomalies

A meaningful step in this work aims to evaluate the acceleration of the landslide body using the following expression:

$$a_t = \frac{v_t - v_{t-30}}{30} \qquad (3.5)$$

where v_t is the displacement rate on day t (Eq. 3.3) and a_t quantify the variation of displacement rates over a 30-days moving time window.
Given the acceleration time series for both sites, potential anomalies were identified using the Interquartile Range (IQR) method (Barbato et al., 2011). The IQR method uses statistical descriptors provided by the quartiles of the data distribution, specifically the first (Q1) and third (Q3) quartiles, to calculate the interquartile range (IQR = Q3 - Q1). Data outside the range defined by Q1-1.5×IQR and Q3+1.5I×QR are considered outliers, which could be linked to extreme scenarios, such as heavy rainfall or groundwater recharge due to significant snow accumulation. It was then checked whether these anomalies are consistent with pronounced fluctuations in groundwater levels.

3.4 Results

3.4.1 Groundwater springs investigations

The daily water levels of the springs were processed from the available hourly dataset and compared with precipitation dataset. As shown in Figure 3.4, the two investigated spring regimes exhibit different behaviours.
For the Cordeminas spring (Figure 3.4a), it is rather difficult to identify regular components as the hydrometric level is fairly constant and ranges between 0.11 m to 0.13 m, with few peaks up to 0.17 m. The spring is strongly influenced by rapid flow contributions, characterised by water level peaks following intense rainfall events, which overlap with the base flow component driven by snowmelt process. A notable example is the highest peak ever recorded, immediately following the precipitation event of December 1, 2023 (60 mm/day). The overview is markedly different in the case of Thures spring (Figure 3.4c) in which the hydrometric values exhibit a more regular and smoothed regime defined by clearly distinguishable snowmelt peaks and seasonal recessions, with variations ranging from 0.13 m to 0.15 m. On the other hand, for the Thures spring, there appears to be no direct influence from a single rainfall event. The hydrograph shows a stronger dependence on the snowmelt process, with peaks clearly associated with the spring season. The

hydrogeological years are easily distinguishable, as well as the summer recession rate is more pronounced. The autocorrelation analysis allowed to highlight precisely these differences, considering as demonstration cases the scenarios of a dry year (2021-2022) and wet year (2023-2024) affecting the Piedmont region, in order to assess their respective impacts on both sources. The winter 2021-2022 was the third warmest and driest in the last 65 years, a highly anomalous season, as such a combination of extreme drought and warm temperatures is rare during winter (Arpa Piemonte, 2024b). On the other hand, the winter 2023-2024 was the warmest in the last 67 years and it was also characterised by abundant precipitation (Arpa Piemonte, 2024c). The amount of spring rainfall was also meaningful: while the spring 2022 was one of the driest since 1958, the spring 2024 had a surplus 102% compared to the 1991-2020 climate reference normal (Arpa Piemonte, 2024h, 2024f).

It is noteworthy that the evaluation of the ACF curves (Figure 3.4b-d) is based on the analysis of water levels trend over the whole hydrogeological year (starting in October) without distinguishing between the corresponding effects of snow and rainfall on spring discharge variations.

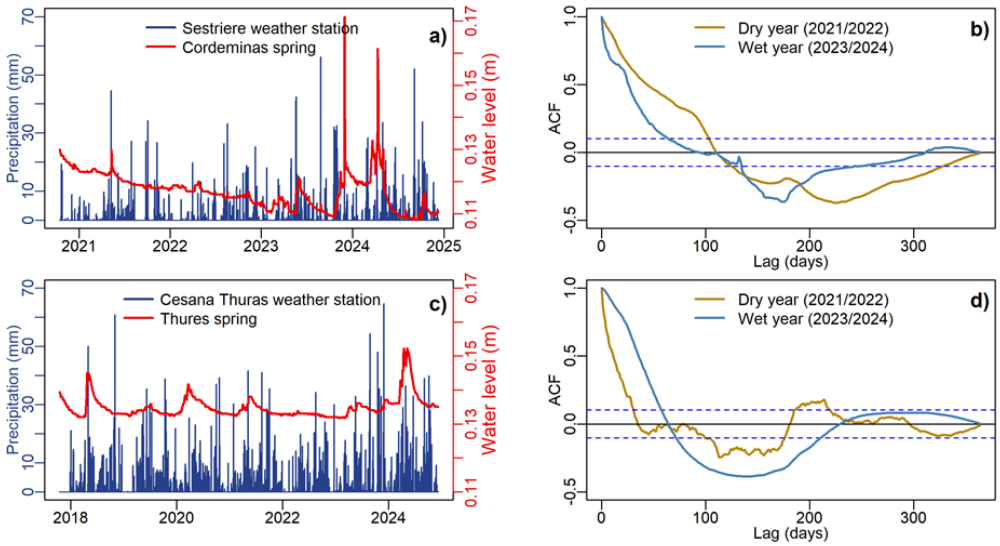

Figure 3.4 Daily spring water levels compared with precipitation at Champlas du Col (a) and Thures (c) and autocorrelogram of Cordeminas (b) and Thures (d).

The hypothesis of a dependent (autocorrelated) time series is tested by evaluating whether the ACF coefficients exceed the 95% confidence limits. An autocorrelation coefficient is considered statistically significant if it falls outside these bounds, which represent the threshold for the entire correlogram.

For the Cordeminas spring (Figure 3.4b), the autocorrelation is higher and longer under dry conditions. A persistent exceeding of the confidence limits can be observed, indicating that the autocorrelation coefficients for this period are significantly different from zero. This suggests that the water level time series is characterized by low variability, making it highly autocorrelated. On the other hand, in 2023/2024, fluctuations in spring levels are more pronounced, suggesting

that the system is more sensitive and responsive to atmospheric inputs. ACF curve decreases more rapidly over time because rainwater infiltrates quickly and is not retained in the system for long time.

The Thures spring autocorrelogram (Figure 3.4d) shows a more rapid decline during dry periods, with values mostly distributed within the confidence interval, indicating that changes in water levels are minimally influenced by previous values. The ACF curve tends to decrease more quickly because daily fluctuations in spring level are less attenuated by the constant recharging action. In contrast, the behaviour is reversed under conditions of heavy rainfall. The system appears to have a greater storage capacity with more gradual release times, as evidenced by the slower recession after annual snowmelt peaks compared to the Cordeminas spring.

To determine the degree of influence of rainfall on the hydrometric levels of the springs – a cross-correlation analysis (Eq. 3.2) was performed. This approach requires eliminating the influence of the winter recharge period up to the peak caused by snowmelt. Snow coverage is predominant from December to April, while rainfall is random throughout the year, with intense events occurring more frequently during summer and autumn season. Springs do not respond directly to winter precipitation as the water feeding the springs comes mainly from snowmelt, which is correlated with temperature fluctuations rather than precipitation (Lo Russo et al., 2021). However, the effect of rainfall on groundwater recharge remains unclear.

Based on these considerations, the cross-correlation between daily water level fluctuations and rainfall time series was evaluated for the period from April to November, under the assumption that no snow precipitation occurs during these months and by neglecting the snowmelt contribution. The analysis was performed for the dry year 2022 (Figure 3.5a-c) and the wet year 2024 (Figure 3.5b-d) of the available water level dataset, comparing the results obtained for both sites.

The graphs clearly show the strength and time of response of the two systems for the scenarios examined. According to the assumptions of the autocorrelation analysis, the Cordeminas spring is more reactive to rainfall inputs and shows marked fluctuations that are not found in the Thures system, which seems to react impassively to precipitation contribution. The strong contrast between the dry and wet years reveals the significant impact of heavy rainfall events.

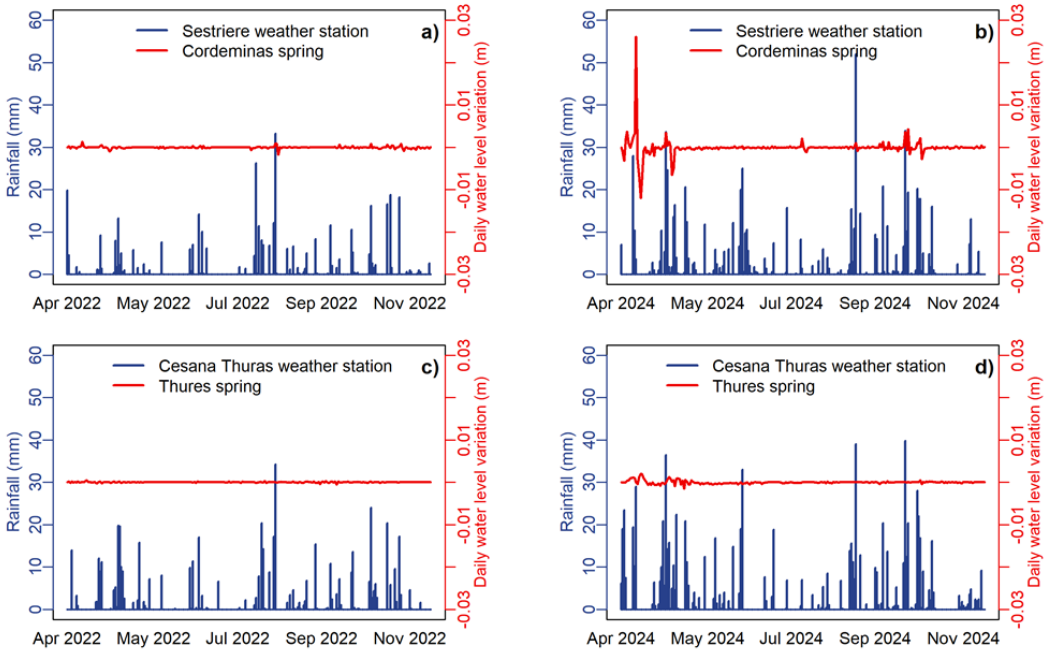

Figure 3.5 Daily water level variations of Cordeminas and Thures spring compared to rainfall in the dry (a,c) and wet year (b,d).

As shown in Figure 3.6, the low cross-correlation values for both springs suggest that the influence of the fast flow component is significantly attenuated by the presence of low-permeability soil, as discussed in the geological setting section. However, the Cordeminas spring appears to respond more quickly and noticeably to intense rainfall events, as shown by the maximum correlation peaks for short lags. On the other hand, water level fluctuations at the Thures spring are less pronounced and nearly negligible, as shown by the low cross-correlation coefficients over longer lags in particular for dry year, in which all CCF values are within the confidence interval. This suggests that the rise in water level is primarily associated to the snowmelt period and it reacts poorly and slowly to rainfall events, maybe regulated by a deeper or more regulated flow system.

Conversely, in 2024, the Thures spring shows a more pronounced response, although with a longer lag than Cordeminas spring, indicating a major influence from the prolonged recharge of rainfall.

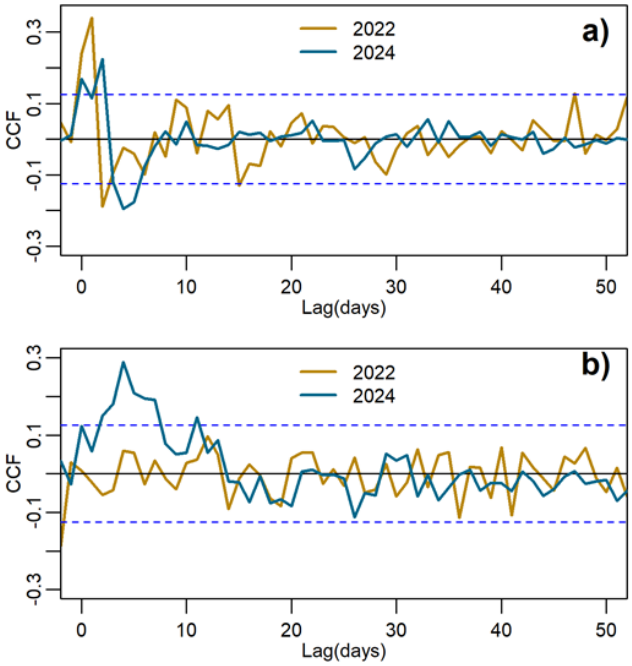

Figure 3.6 Crosscorrelogram of (a) Cordeminas and (b) Thures spring water levels.

3.4.2 Cause-effect relationships between groundwater fluctuations and landslide displacement trends

Daily time series of spring water level and inclinometer displacement were compared for both sites to understand if their trends are compliant. The graphs in Figure 3.7 show how the processed inclinometer data (Eq. 3.3) accurately describes the evolution of landslide body movement over the year, suggesting a more direct dependence on variations in the groundwater level pattern.

In the first case, the supplementary dataset of piezometric values provided by P6SSTC4 was also exploited, as discussed in the section 3, by considering the available displacements dataset (until 10 June 2024). Thus, knowing the date of installation of the Cordeminas probe, the spring hydrometric level, the groundwater level and displacement trends from October 2020 to June 2024 were plotted (Figure 3.7a).

In the case of Thures (Figure 3.7c), on the other hand, it is possible to observe how spring data can capture the landslide displacement trend over hydrogeological years. The acceleration phase of the landslide body is clearly recognisable in the spring season in coincidence with the snowmelt period, which is precisely described by the spring recharge leading up to the snowmelt peak.

The power spectral density, described in section 3.3, was applied to investigate the seasonal components of springs and displacements. Panels in Figure 3.7b-d show the power spectrum in the frequency domain (1/day) and the frequencies

associated with the most significant peaks are reported in the corresponding Table 3.2.

In both cases, a peak at approximately 365 days was detected (frequency 4 in Champlas and frequency 7 in Thures), indicating a complete annual variation of the signals, with water level peaking during spring season and then returning to their initial values, strictly affecting the displacements. This finding suggests a relatively consistent pattern typical of spring discharge across hydrological years.

However, for both systems, the first dominant peak appears at lower frequencies (1 in Champlas du Col and 2 in Thures) indicating a non-cyclical component likely associated with an extreme event throughout the entire dataset. This phenomenon corresponds to the conditions occurred in the spring 2024, when heavy precipitation led to an unusual increase in both groundwater levels and landslide displacement rates. The spectral response suggests that this event had a significant impact on the landslide dynamics, inducing an acceleration phase that deviated from the typical displacements trend.

In this analysis, the difference between the performance of the spring and the piezometer in Figure 3.7b in delineating displacement variations is quite imperceptible. Although they measure different parameters, both reflect the groundwater recharge regime, which intensifies during snowmelt. Consequently, the annual component is unequivocal in both spectra. The correlation analysis has highlighted the importance of piezometric data to describe displacement variations over time, as spring data alone do not adequately capture these variations, particularly in Cordeminas spring. As discussed in detail in previous sections, the water levels of the Thures spring show a more pronounced regularity, suggesting a stronger annual cyclical pattern, as revealed by the higher PSD magnitude compared to the annual component of the Cordeminas spring.

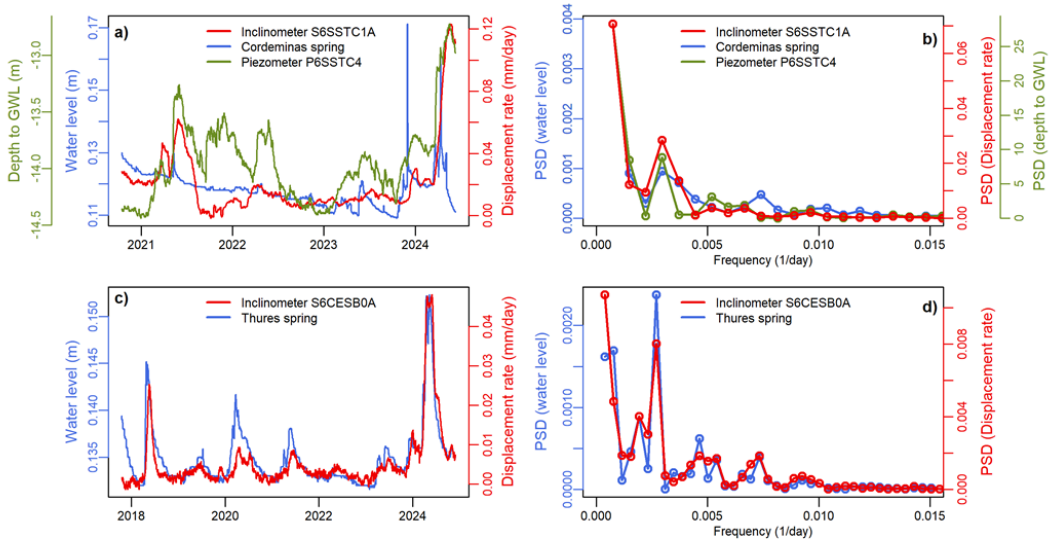

Figure 3.7 Groundwater level patterns and displacement rates in (a) Champlas du Col and (c)Thures and related spectral analysis (b,d).

Table 3.2 Main components (indices in brackets) of PSD curve.

	Frequency (1/day)			Days
	Spring	**P6SSTC4**	**S6SSTC1A**	
(i) Champlas du Col	(1) 0.00074 (4) 0.00296	(1) 0.00074 (4) 0.00296	(1) 0.00074 (4) 0.00296	(1) 1350 (4) 338
	Spring	**-**	**S6CESB0A**	
(ii) Thures	(2) 0.00077 (7) 0.00270	-	(1) 0.00038 (7) 0.00270	(1) 2592 (2) 1296 (7) 370

These considerations are supported by correlation analysis between the variables in Figure 3.7 using the *pairs.panel()* function provided by the *psych()* library (Revelle, 2023). Each panel in the matrix provides complementary information on the relationships among the monitored variables. The plots below the diagonal show the bivariate scatterplots between each pair of variables, highlighting their degree of linear association (the red line represents the linear fit). The histograms in the diagonal panels show the distribution of the datasets and the Pearson correlation coefficients above the diagonal quantify the strength and direction of the linear relationships between variables (values close to 1 indicate a strong positive correlation).

The correlation matrix for the case (i) (Figure 3.8a) shows a weak relationship between the spring data and the displacement data, indicating that the water level signal does not fully describe the landslide deformations. However, when the depth to groundwater level (gwl) is considered, the correlation with displacement increases substantially ($r = 0.70$), suggesting that the piezometric data effectively capture the hydromechanical response of the Champlas du Col system. Conversely, in the case (ii) (Figure 3.8b) a much stronger correlation is observed, proving that spring water levels can adequately describes the deformation behaviour. These findings suggest that the linear correlation provides a reasonable first-order approximation of the proportional relationship between water level and displacement. Nevertheless, it assumes instantaneous responses between the variables, without accounting for potential lag effects.

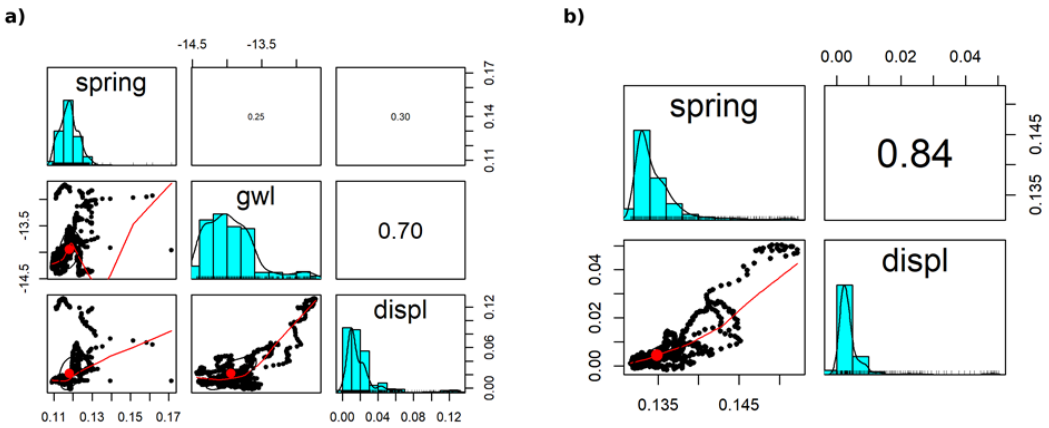

Figure 3.8 Correlation matrix for the (a) Champlas du Col and (b) Thures case study.

In this final section, acceleration values were derived from displacement rates to identify potential anomalies under specific conditions. In addition to the already discussed scenario of spring 2024, similar patterns were also observed in spring 2018, affected by heavy and prolonged precipitation (Arpa Piemonte, 2024d). Analysis of landslide accelerations (Figure 3.9) related to snow cover height provides a more sensitive assessment of normalised displacement rates over time, particularly in capturing responses to triggering factors.

This approach allows the characterisation of anomalous accelerations of the landslide body based solely on spring level data for Thures and piezometric level data for Champlas, thus avoiding the analysis of precipitation pattern.

Since the Cesana Thuras weather station does not have a snow gauge, data from the Sestriere station were also adopted for the Thures site (Figure 3.9b), assuming similar conditions. The main landslide acceleration phases appear to be driven by meaningful fluctuations in piezometric levels for Champlas du Col system (Figure 3.9a) which rise significantly following the groundwater recharge due to snowmelt. This further supplement the work addressed in Section 3.3.2. Noteworthy are the peaks in piezometric data observed during the spring season, which appear to be proportional to the amount of accumulated snow on the ground. Conversely, in Thures system (Figure 3.9b), the anomalies are associated with abnormal increases in spring water levels occurring in the same season, likely due to similar hydrological processes.

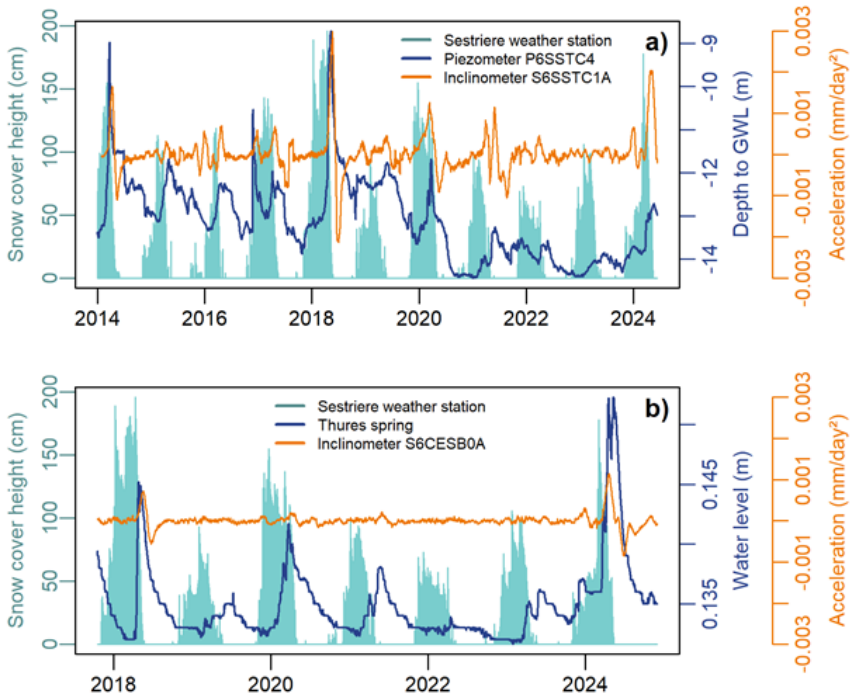

Figure 3.9 Acceleration patterns of the (a) Champlas du Col and (b) Thures landslide.

In this context, the Interquartile Range (IQR) method was applied to identify significant outliers from the central distribution of the data. The insight of the data distributions (Figure 3.8) indicates that the variables are non-normally distributed, although without significant skewness. Given this condition, the use of the IQR method is appropriate, as it is a non-parametric and robust approach that does not require normality (Helsel et al., 2020). The Table 3.3 summarizes the key statistical descriptors of the dataset, including mean and quartiles. It is noteworthy that the mean and median are almost identical for each variable, confirming that the deviation from normality is minimal. Based on the first (Q1) and third (Q3) quartiles, the lower and upper bounds of the central distribution were defined. In order to detect abnormal accelerations—potentially indicators of rapid displacement rate or sudden instabilities of the landslide body—only values exceeding the upper bound (Q3 + 1.5 × IQR) were considered. Lower outliers are excluded, as they correspond to deceleration phases of the landslide, which are not relevant for risk assessment purposes.

In both systems, the temporal ranges of acceleration outliers identified in the 2018 and 2024 scenarios exhibit a short lag of only a few days relative to the onset of anomalies in the groundwater level time series. This short lag suggests a rapid response of slope acceleration to hydrological forcing. However, in case (i), notable accelerations were recorded during spring 2024 despite the absence of corresponding outliers in the piezometric series. This discrepancy is attributed to unusually warm winter temperatures, which led to early snowmelt and early-season soil saturation. Under these conditions, the water table rise was low, as the water infiltrated during the prolonged rainfall did not migrate downwards as quickly as in the case of unsaturated soil. This process triggered a marked acceleration in both systems, approximately one month earlier than in 2018.

Table 3.3 Statistical descriptors and identified outliers in groundwater level (GWL) and acceleration patterns.

	GWL (P6SSTC4)		Outliers (>Q3+1.5×IQR)	Acceleration (S6SSTC1A)		Outliers (>Q3+1.5×IQR)
(i) Champlas du Col	*Mean*	-13.10	19/04-21/05/2018 -8.71 (peak on 10/05/2018)	*Mean*	2.68e-05	22/04-07/06/2018 2.97e-03 (peak on 20/05/2018)
	Median	-13.15		*Median*	1.24e-05	
	Min	-14.44		*Min*	-2.13e-03	
	Max	-8.71		*Max*	2.97e-03	28/03-28/05/2024 2.04e-03 (peak on 05/05/2024)
	Q1	-13.87		*Q1*	-1.22e-04	
	Q3	-12.41		*Q3*	1.11e-04	
	Q1-1.5×IQR	-16.06		*Q1-1.5×IQR*	-4.70e-04	
	Q3+1.5×IQR	-10.22		*Q3+1.5×IQR*	4.60e-04	
	GWL (spring)		**Outliers (>Q3+1.5×IQR)**	**Acceleration (S6CESB0A)**		**Outliers (>Q3+1.5×IQR)**
(ii)Thures	*Mean*	0.1349	22/04-30/05/2018 0.1452 (peak on 27/04/2018) 22/03-27/06/2024 0.1523 (peak on 17/04/2024)	*Mean*	2.59e-06	24/04-04/06/2018 7.22e-04 (peak on 17/05/2018) 23/03-13/05/2024 1.14e-03 (peak on 19/04/2024)
	Median	0.1340		*Median*	1.96e-06	
	Min	-0.1316		*Min*	-8.44e-04	
	Max	0.1523		*Max*	1.14e-03	
	Q1	0.1330		*Q1*	4.44e-05	
	Q3	0.1359		*Q3*	3.33e-05	
	Q1-1.5×IQR	0.1286		*Q1-1.5×IQR*	-1.60e-04	
	Q3+1.5×IQR	0.1402		*Q3+1.5×IQR*	1.50e-04	

3.5 Discussion

The purpose of this study was twofold: firstly, to clarify the relationship between groundwater regime and landslide displacements in the mountain context of Susa Valley and secondly, to explore the potential of using spring behaviour as an indicator to detect and forecast landslide acceleration. The two sites analysed, Champlas du Col and Thures, are affected by deep-seated landslides who hidden shallower landslides whose movements are strongly dependent on hydrogeological factors.

The presence of monitoring points in both sites enabled a comprehensive statistical analysis using groundwater level variations and displacement data. Each spring located on the landslide body play a crucial role, providing valuable insights into aquifer dynamics in response to precipitation and annual snowmelt cycles. The analysis of the water levels using piezometer also allowed for a better understanding of the infiltration process within these systems and whether they can influence the acceleration phases of landslide movements (Corominas et al., 2005). However, the limited spatial distribution of springs across large areas represents a constraint for this analysis. In the first case, the hydrometric levels of the spring are not representative of the groundwater fluctuations occurring at Champlas du Col, as the spring is located far from the SP23R road, where the main sliding surfaces responsible for continuous surface deformations are detected by the S6SSTC1A

inclinometer. As demonstrated by the correlation analysis, in this case, piezometric data are more reliable than spring water levels for predicting changes in displacement rates.

Conversely, for Thures site the spring hydrometric data and displacement measurements from the S6CESB0A inclinometer can be spatially correlated and it provides a valuable case study for the development of forecasting models of landslide displacement trends based on spring dynamics.

Autocorrelation and spectral analysis applied to the spring water level data highlighted the influence of monitoring location on the hydrometric level patterns. The Cordeminas spring is part of a shallower system, situated near the aquifer recharge area at the top of the landslide body, which makes it more sensitive to surface runoff from rainfall, as also confirmed by the cross-correlation results (Figure 3.6a-b). In contrast, the spring at Thures is fed by an aquifer primarily influenced by snowmelt, with rainfall contributing only minimally, though not insignificantly. In this context, extending the analysis to additional spring parameters, such as electrical conductivity, could provide valuable insights into seasonal responses to external inputs.

As discussed in previous work (Musbah et al., 2019), Fourier analysis has made it possible to identify cyclical components in the groundwater fluctuations, and to understand how these can lead to periodic variations in displacement (Conte et al., 2016; Vallet et al., 2016; C. Wang et al., 2023). The power spectrum applied to the variables of interest revealed that the groundwater regime—monitored through spring hydrometric level and piezometric data—exhibits a clear annual pattern governed by snowmelt. This analysis also confirmed that the activity of most slow-moving landslides is seasonal, following the periodicity of groundwater fluctuations (Liu et al., 2022; Van Asch et al., 2009). If the water content in the slope is strongly correlated with snow accumulation, which governs the long-term hydrological balance of groundwater recharge in deep landslides, then short-term hydroclimatic conditions also play an important role in soil saturation (Prokešová et al., 2013). Indeed, extreme weather events, such as those recorded in 2024, can cause sharp increases in groundwater levels, leading to significant acceleration phases. These are identified as rare events through spectral analysis of the available dataset and are also recognized as outliers within the overall dataset.

The rapid development of slope saturation occurred in spring 2024 undoubtedly affected the time lag in the landslide system's response. In this regard, the analyses could be expanded by assessing the water content responsible for the behaviour of deep-seated landslides, through appropriate numerical and hydromechanical models (Cappa et al., 2014; Conte & Troncone, 2011; Yokoyama et al., 2022), which can simulate deformations under specific soil saturation conditions. This would allow to identify threshold values based on the contributions of precipitation as well as the role of temperature variations on snowmelt process.

This numerical approach could be adopted particularly in the case of Champlas du Col, since the analyses carried out have shown the strategic importance of the area in terms of possible protective measures to be planned for the presence of the SP23R road. As ARPA Piemonte reports, the greatest displacements occurred after

the wettest winters. In the case of Champlas, cumulative precipitation above 100 mm in the winter season of the years 2014, 2018, 2020, 2024, with a peak of 206 mm in 2018, the snowiest winter, resulted in bimonthly displacements during the spring season with values between 3 and 6 mm, when the average value is 1.42 mm. In particular, the year 2024 was the most anomalous as April and May months were very rainy (Arpa Piemonte, 2024e) that led to a significant increase in surface deformations, in this regard the S6SSTC1A inclinometer recorded the highest value so far (7.06 mm) on 5 June 2024. Given these considerations, a much more extensive monitoring network based on geophysical surveys could be designed to monitor the constant infiltrative inputs affecting the Champlas du Col landslide body.

In summary, the potential use of spring dynamics as an indicator of landslide displacement and acceleration is promising, as demonstrated in this study, but it also presents some limitations: i) the location and distribution of springs within the landslide body, depending on its geological setting and spatial extent; ii) the hydrodynamic characteristics of the water circulating within the landslide mass; iii) the availability of deep deformation measurements. Nevertheless, spring data offer a valuable alternative to the traditional monitoring approach based on piezometric data, also because spring probes are unaffected by deep slope movements which frequently damage piezometer pipe, thereby reducing intervention costs in the view of maintenance needs.

3.6 Conclusions

In this chapter, two deep-seated landslides in the Susa Valley are represented as clear example of gravitational phenomena influenced by variations groundwater levels. To investigate the effects of seasonal groundwater fluctuations on landslide displacement trends, a purely statistical analysis approach was developed. This approach provides a valuable tool for interpreting slope accelerations in relations to water level changes in terms of spring data.

Among the two case studies discussed, the Thures landslide appears to be the most suitable for predicting displacement variations based on the spring hydrometric levels. Nonetheless, the Champlas du Col site is also of significant interest due to the potential for additional surveys that could improve the assessment of surface movements and help mitigate ongoing damage to the SP23R road.

Chapter 4

Hydrochemical analyses

4.1 Spring dynamics and water sampling

In the research field of slope stability, knowledge of groundwater behaviour is essential for understanding the hydrogeological dynamics of slope failure, but at the same time it typically suffers from a lack of data, given the complexity of large landslide systems (Lindenmaier et al., 2005; Tullen et al ., 2002) with very variable water pathways. While monitoring the spatial distribution of pore pressure in the slope is crucial (Anson & Hawkins, 2002) for explaining local variation in mass movement pattern and propose mitigation measures, water chemistry can get insights on the subsoil hydrogeological setting and groundwater circulation (Flores et al., 2023). In this context, isotope measurements and geochemical analyses could be undertaken to identify zones of water infiltration within the landslide body and to map groundwater flowpaths (Bogaard et al., 2007; Islam & Mostafa, 2022).

While monitoring the springs discharge allows to observe the dynamic characteristics of an aquifer, monitoring additional physical and chemical properties of the water, such as temperature and electrical conductivity, can greatly enhance the detection of these processes (Filippini et al., 2018). Figure 4.1 shows time series of water level, temperature and electrical conductivity for the Cordeminas and Thures springs, with the aim of supplementing the findings discussed in the Section 3.4. Although dealing with water levels, it is clear that both springs are characterised by low discharge rates (roughly 0.5 l/s) and relatively slow recession dynamics particularly for Thures, confirming the presence of significant groundwater reserves in low-permeability systems (Fioraso & Mosca, 2014).

Electrical conductivity (EC) is an indicator of total ionic content and thus directly reflects water mineralization, which in turn depends on the residence time of water in the aquifer system. As EC is sensitive to dissolution processes, and thus to the time required for water to reach chemical equilibrium with surrounding rocks (Athamena et al., 2022; Kouassi et al., 2016; Rembert et al., 2020), persistent high values are linked to longer residence times. For mountain springs, a decrease of these values is a consequence of dilution by recent infiltrated water from precipitation and snowmelt (Brighenti et al., 2021; Chiaudani et al., 2019), thus providing additional information on the reactivity of spring system to meteorological inputs. Conversely, EC rises during dry periods, as the contribution of older groundwater increases.

At both sites, EC values approximately ranges between 350 µS/cm and 500 µS/cm, with pronounced spikes for Cordeminas (Figure 4.1a), in compliance with

temperature variations, confirming greater sensitivity of this spring to external conditions. On the contrary, the EC pattern for Thures (Figure 4.1b) is smoother, accurately capturing the dilution phases that occur with the recharge phases during the snowmelt period. However, instrumental malfunctions have been identified at this site, resulting in some unrealistic values observed as consistent negative peaks in the time series that do not align with the temperature and levels.

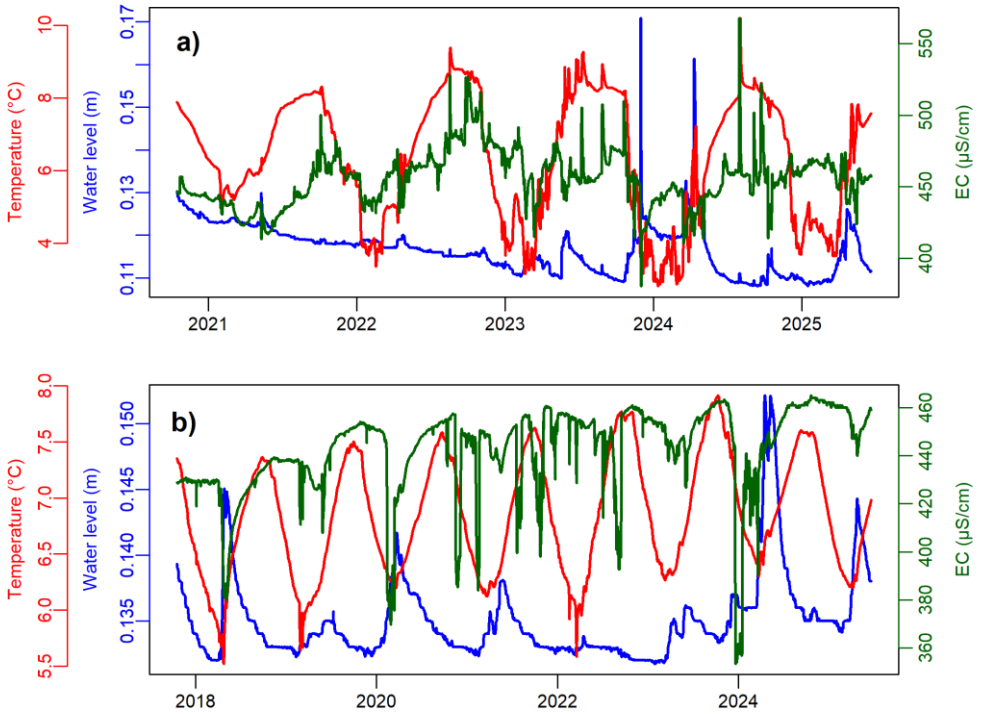

Figure 4.1 Time series of spring parameters for (a) Cordeminas and (b) Thures, updated to 20 June 2025.

It is important to note that the temperature patterns reveal significant differences between the two sites when compared with the air temperature (Figure 4.2). Cordeminas appears to be more in equilibrium with the external conditions than Thures, as evidenced by a much wider range of values, with peaks of up to 10 °C. The relatively constant temperature with slight fluctuations at the Thures spring once again indicates a more resilient system capable of mitigating the effects of random disturbances caused by a single precipitation event or sudden temperature changes.

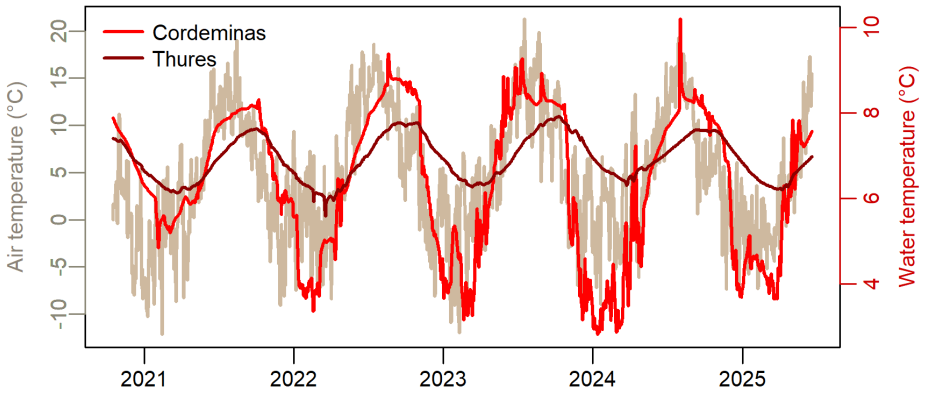

Figure 4.2 Comparison between spring water temperature for both sites and air temperature (Sestriere weather station).

In addition to the two instrumented springs analysed in this study, several other springs located on the Champlas du Col and Thures landslides (Figure 4.3) are monitored by Arpa Piemonte in collaboration with DIATI at the Politecnico di Torino.

The sampling campaigns are typically carried out twice a year and the collected water samples are analysed for the hydrogeological characterization of both sites.
In Champlas du Col, four sampling points were chosen:

- Boiler (1970 m s.l.m.);
- Cordeminas (1960 m s.l.m.);
- Tunnel Drenante (1875 m s.l.m.);
- CFAV (1855 m s.l.m.).

Spring monitoring started at different times. Sampling at Cordeminas, Boiler, and Tunnel Drenante began on 4 November 2020, whereas monitoring at CFAV started on 29 April 2021.
In Thures, five springs were selected:

- Alta (1890 m s.l.m.);
- Thures 2 (1700 m s.l.m.);
- Fontana Thures (1660 m s.l.m.);
- Rotazionale (1660 m s.l.m.);
- Abete Bianco (1585 m s.l.m.).

Also in this case, monitoring began in different years. The first sampling of Abete Bianco, Rotazione and Fontana Thures springs took place on 18 October 2017, while Alta and Thures 2 points began on 4 October 2018. For the Alta spring, only the first sample collected on 4 October 2018 is available, as no further sampling could be performed due to logistical constraints when accessing the site, particularly in snowy conditions. Consequently, the Alta spring was excluded from the results, since the dataset consists of only a single measurement (Bonomo, 2023).

As discussed in the Chapter 3, only the Cordeminas and Thures 2 springs are equipped with multiparametric probes for the continuous recording of water level, electrical conductivity and temperature.

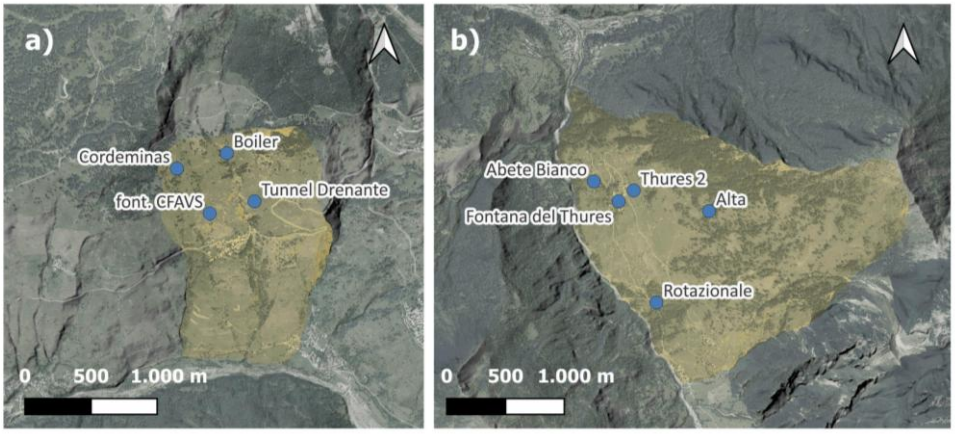

Figure 4.3 Monitored water spring at a) Champlas and b) Thures for hydrochemical purposes.

4.2 Physical-chemical analyses

Electrical conductivity (standardised to 25°C), temperature (Ma et al., 2011), redox potential (Eh) and pH are measured in situ at each sampling point using the WTW multiparameter probe. The collection of these values allows to qualitatively map the groundwater flow circuit and to detect possible spatial variations. It is noteworthy that for some sampling campaigns these parameters are missing, while chemical analyses were carried out as usual on the water samples collected. As reported in Table 4.1 and Table 4.2, the numerical suffix in the alphanumeric code for each sampling point denotes the measurement campaigns sequence, referenced to the first Thures sampling (18 October 2017), and provides a common identifier for both sites.

Eh provides an approximate indication of the oxidative or reductive properties of groundwater and, indirectly, of oxygen availability and recent recharge. Generally, positive Eh values (typically 50-300 mV) reflect oxidising conditions, which are commonly observed in shallow flow systems (Ramesh Kumar & Riyazuddin, 2012). In contrast, deeper or longer-residence groundwater commonly show low or negative Eh values, associated with the prevalence of reducing conditions. As Eh is a non-specific and frequently non-equilibrium measurement, it is most reliably interpreted when supplemented by suitable field procedures and additional indicators, especially dissolved oxygen. At both sites, the relatively constant EC and positive Eh values are characteristic of shallow flow systems with ongoing recharge and limited reducing mineralisation (Barcelona et al., 1989; Ramesh Kumar & Riyazuddin, 2012; Turkeltaub et al., 2023). This assumption is further supported by measurements taken on 21 November, which revealed

dissolved oxygen saturation of around 90% at several monitoring points, suggesting a close dependence on atmosphere conditions. Overall, these observations support the hypothesis that the water is not under pressure and originates from a relatively shallow, unconfined aquifer.

The T and EC measured by the OTT probe at the Cordeminas and Thures 2 springs are also reported in Table 4.1 and Table 4.2. These data enable the comparison between the multiparametric probe recording and the instantaneous value, allowing to check the reliability of OTT probe measurements and to identify potential instrumental issues, as in the case of the EC values for Thures 2. Indeed, significant discrepancies have been reported between OTT values and in situ measurements (approximately of 100 µS/cm on 22 October 2021 and 21 November 2025).

Table 4.1 Physical-chemical parameters measured at the Champlas du Col springs during sampling campaigns. Springs are identified by alphanumeric codes (Boiler = BO; CFAV; Cordeminas=COR; TD=Tunnel Drenante), ordered chronologically by sampling date.

Sampling date	Code	pH	T WTW [°C]	T OTT [°C]	EC WTW [µS/cm]	EC OTT [µS/cm]	Eh [mV]
4-nov-20	**BO-07**	8.78	7.80		583		156
29-apr-21	**BO-08**	8.07	5.60		596		263
22-ott-21	**BO-09**	7.79	7.70		592		
3-ago-22	**BO-10**						
15-nov-22	**BO-11**						
12-dic-23	**BO-12**	7.80	7.60		564		62
10-giu-24	**BO-13**	7.58	7.60		640		225
9-dic-24	**BO-14**						
20-giu-25	**BO-15**						
21-nov-25	**BO-16**	7.35	7.80		308		318
29-apr-21	**CFAV-08**	8.72	7.10		501		280
22-ott-21	**CFAV-09**	8.12	8.70		555		
3-ago-22	**CFAV-10**						
15-nov-22	**CFAV-11**						
12-dic-23	**CFAV-12**	8.03	6.80		544		148
10-giu-24	**CFAV-13**	7.87	8.90		525		250
9-dic-24	**CFAV-14**						
20-giu-25	**CFAV-15**						
21-nov-25	**CFAV-16**	8.48	3.70		570		162
4-nov-20	**COR-07**	9.06	7.60	7.53	480	450	165
29-apr-21	**COR-08**	8.42	6.10	5.93	464	433	332
22-ott-21	**COR-09**	7.94	7.60	7.64	481	460	
3-ago-22	**COR-10**						
15-nov-22	**COR-11**						
12-dic-23	**COR-12**	7.90	4.20	4.20	449	422	99
10-giu-24	**COR-13**	7.86	7.80	7.96	462	448	200
9-dic-24	**COR-14**		4.58	4.58	461	460	
20-giu-25	**COR-15**						

21-nov-25	**COR-16**	8.25	6.80		488	487	220
4-nov-20	**TD-07**	8.74	8.00		679		87
29-apr-21	**TD-08**	8.58	6.70		645		258
22-ott-21	**TD-09**	7.74	8.30		668		
3-ago-22	**TD-10**						
12-dic-23	**TD-12**						
10-giu-24	**TD-13**	7.45	7.90		602		260

Table 4.2 Physical-chemical parameters measured at the Thures springs during sampling campaigns. Springs are identified by alphanumeric codes (Abete Bianco = ABTH; Thures 2=CTH; Fontana Thures=FTH; Rotazionale=SRTH) ordered chronologically by sampling date.

Sampling date	**Code**	**pH**	**T WTW [°C]**	**T OTT [°C]**	**EC WTW [µS/cm]**	**EC OTT [µS/cm]**	**Eh [mV]**
18-ott-17	**ABTH-01**	7.43			480		247
28-mag-18	**ABTH-02**	8.12			332		211
4-ott-18	**ABTH-03**						
20-giu-19	**ABTH-04**	7.68	7.10		581		207
21-nov-19	**ABTH-05**	8.26	7.90		564		260
29-giu-20	**ABTH-06**	8.60	7.70		542		185
4-nov-20	**ABTH-07**	7.55	8.10		557		254
22-ott-21	**ABTH-09**	7.71	8.40		570		
3-ago-22	**ABTH-10**						
15-nov-22	**ABTH-11**						
12-dic-23	**ABTH-12**						
10-giu-24	**ABTH-13**						
9-dic-24	**ABTH-14**						
20-giu-25	**ABTH-15**						
4-ott-18	**CTH-03**		7.40	7.33	416	435	
20-giu-19	**CTH-04**	7.72	6.60	6.61	440	440	250
21-nov-19	**CTH-05**	8.61	7.00	7.04	450	453	220
29-giu-20	**CTH-06**	8.90	6.90	6.93	444	448	257
4-nov-20	**CTH-07**	9.34	7.30	736	452	457	135
29-apr-21	**CTH-08**	8.40	6.40	6.28	440	443	238
22-ott-21	**CTH-09**	8.31	7.50	7.50	450	384	
3-ago-22	**CTH-10**						
15-nov-22	**CTH-11**						
12-dic-23	**CTH-12**		7.26	7.26	446	445	
10-giu-24	**CTH-13**	7.65	6.90	6.92	446	451	235
9-dic-24	**CTH-14**						
20-giu-25	**CTH-15**						
21-nov-25	**CTH-16**	7.72	5.80	7.22	485	390	260
18-ott-17	**FTH-01**	7.27			690		310
28-mag-18	**FTH-02**	8.24			370		288
4-ott-18	**FTH-03**		8.10		663		
20-giu-19	**FTH-04**	7.40	7.60		693		235
21-nov-19	**FTH-05**	8.04	6.90		710		209

29-giu-20	**FTH-06**	8.53	7.90	692	290
4-nov-20	**FTH-07**	8.04	7.60	714	144
29-apr-21	**FTH-08**		6.60	703	
22-ott-21	**FTH-09**	7.83	7.80	716	
3-ago-22	**FTH-10**				
15-nov-22	**FTH-11**				
12-dic-23	**FTH-12**				
10-giu-24	**FTH-13**	7.35	8.00	710	277
9-dic-24	**FTH-14**				
20-giu-25	**FTH-15**				
21-nov-25	**FTH-16**	7.95	6.40	720	114
4-ott-18	**SRTH-03**		9.30	736	
20-giu-19	**SRTH-04**	7.50	7.00	690	233
21-nov-19	**SRTH-05**	7.75	7.40	751	283
29-giu-20	**SRTH-06**	7.93	7.10	743	260
4-nov-20	**SRTH-07**	7.92	7.60	783	277
29-apr-21	**SRTH-08**				
22-ott-21	**SRTH-09**	7.60	7.70	810	
3-ago-22	**SRTH-10**				
15-nov-22	**SRTH-11**				
12-dic-23	**SRTH-12**				
10-giu-24	**SRTH-13**	7.26	7.20	790	194
9-dic-24	**SRTH-14**				
20-giu-25	**SRTH-15**				
21-nov-25	**SRTH-16**	7.52	7.60	803	245

Chemical analyses of the collected water samples were performed in the Hydrochemical Laboratory of the DIATI.

Chemical data (Appendix B) were treated with Piper and Schoeller diagrams. The Piper diagram highlights the relationships between the four cations (Ca^{2+}, Mg^{2+}, Na^{+} and K^{+}) and the four anions (CO_3^{2-}, HCO_3^{-}, Cl^{-} and SO_4^{2-}) expressed as percentages, to simultaneously compare a large number of water samples enabling the definition of the hydrochemical facies (Piper, 1944) (Figure 4.4 and Figure 4.5).

The analyses of major ions show that groundwater samples from both sites generally belong to the Ca-HCO_3 facies due to the presence of calcschists in the area, as proven by the stratigraphy obtained from surveys near the Champlas du Col and Thures localities. The diagrams show that the water samples collected at the monitoring points exhibit remarkably similar chemical properties, with a few exceptions.

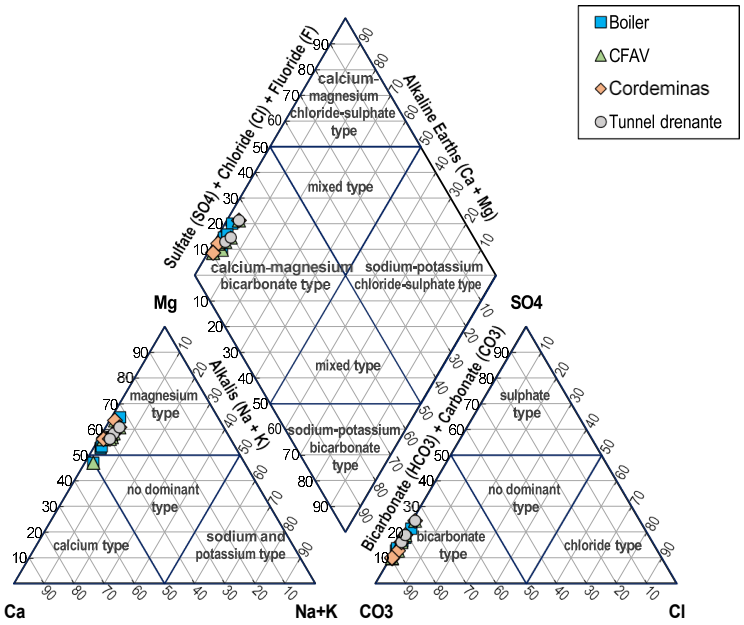

Figure 4.4 Piper diagrams including sampled water of Boiler, Cordeminas, CFAV and Tunnel Drenante springs.

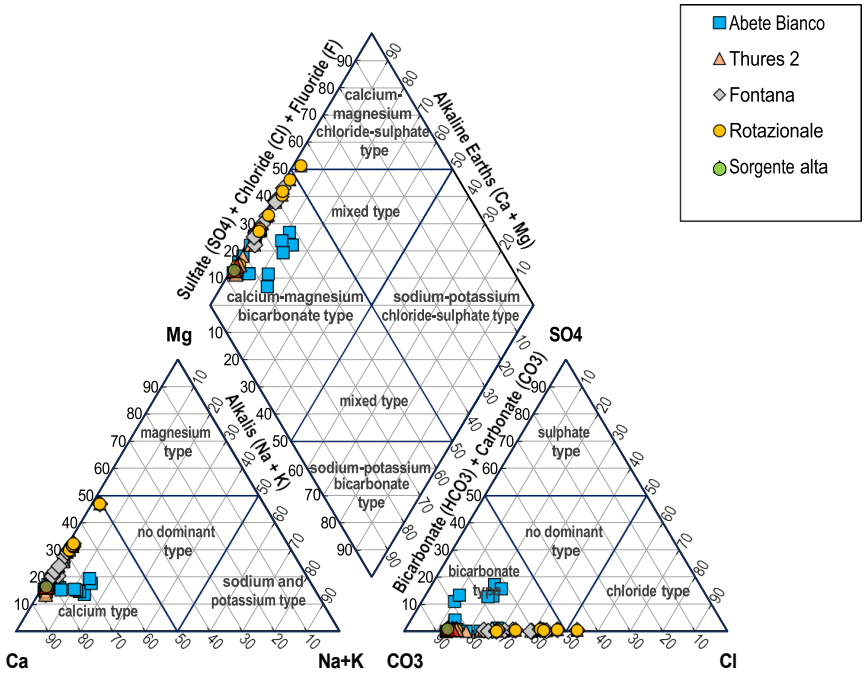

Figure 4.5 Piper diagrams including sampled water of Alta, Thures 2, Rotazionale, Abete Bianco and Fontana Thures springs.

The Schoeller diagram plots the absolute concentrations of major ions on a semi-logarithmic scale at each monitoring point (Schoeller, 1962). For simplicity, Figure 4.6 and Figure 4.7 show only the Schoeller diagrams for Cordeminas and Thures 2 springs, whereas the diagrams for the other springs can be found in Appendix B. The Schoeller diagram illustrates how the chemical composition of the water in the substrate varies seasonally, reflecting the same behaviour of EC. In particular, the reduction in ionic concentrations during the summer is directly attributable to the dilution effect due to snowmelt. Conversely, higher values are typically associated with dry periods, when reduced recharge limits the supply of newly infiltrated water and promotes longer groundwater residence times.

The Schoeller diagrams for the Boiler (Figure B.1), CFAV (Figure B.2) and Cordeminas (Figure 4.6) sites indicate higher magnesium concentrations, which is consistent with the bicarbonate-calcium-magnesium facies of these waters. At the Thures site, a secondary sulphate-magnesium facies is identified for both the Fontana spring (Figure B.4) and the Rotazionale spring (Figure B.5). The high concentration of SO_4^{2-} ions is likely due to the presence of gypsum embedded in the calcareous schist substrate, and therefore the deep-water flow in this portion of the rock mass causes a slow dissolution of these salts. Furthermore, chloride ions are present in significantly higher quantities in water samples taken from the Abete Bianco spring (Figure B.6) than at other monitoring points, probably due to the impact of road de-icing (Bonomo, 2023).

Overall, the mineralisation of these waters remains constant throughout the sampling period, except for chloride salts, which were present in higher concentrations in samples taken in 2022 likely due to the scarcity of precipitation that year (De Luca et al., 2019). The persistence of fairly constant EC, water chemistry and temperature at these springs distributed along the slope is probably due to the presence of a large aquifer in the porous deposits, which allow homogenization of the chemical composition of groundwater throughout the year (Briški et al., 2020; Comina et al., 2025).

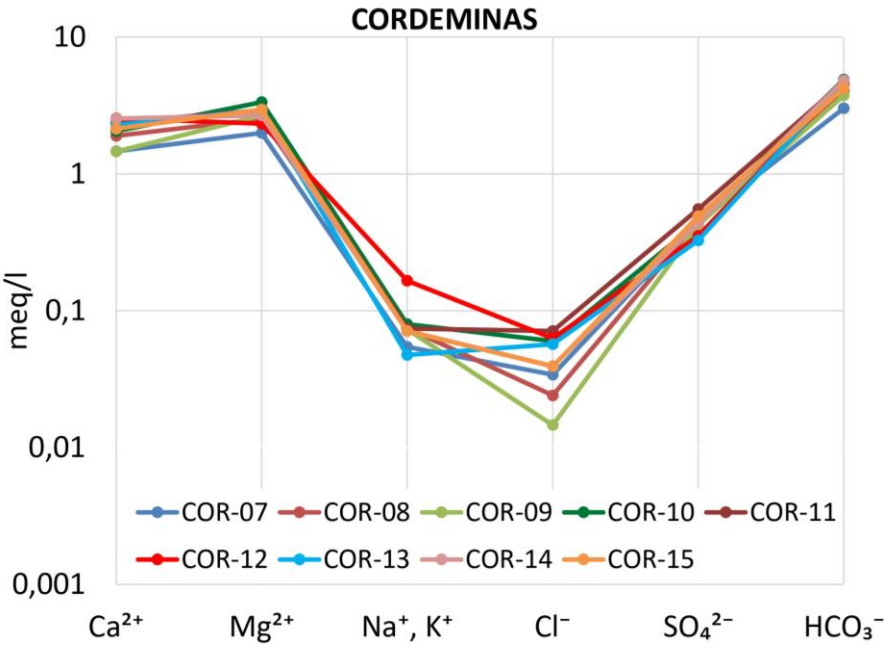

Figure 4.6 Schoeller diagram of Cordeminas spring.

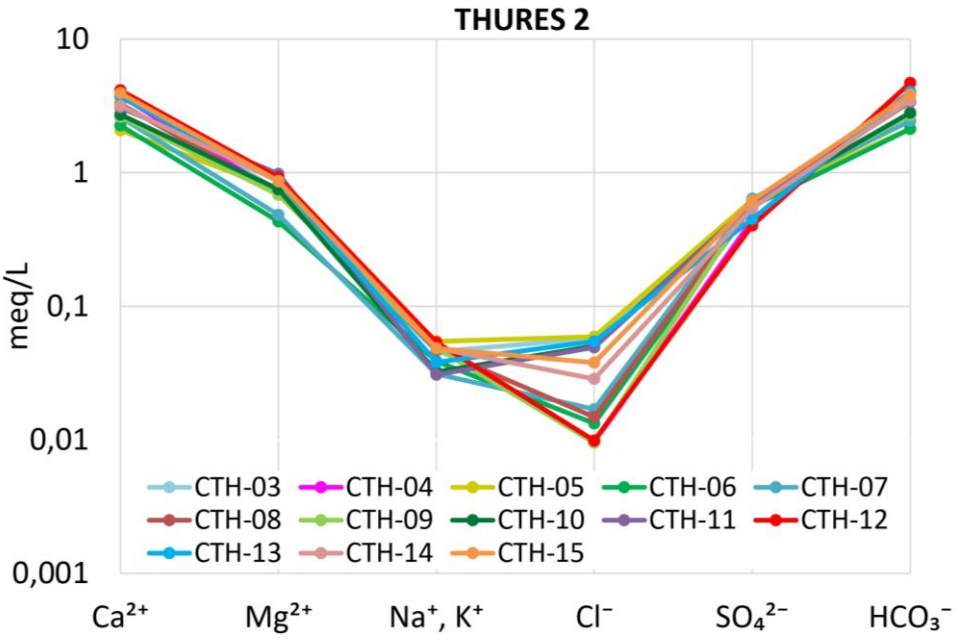

Figure 4.7 Schoeller diagram for Thures 2 spring.

Chapter 5

Data-driven prediction of landslide displacement

5.1 Time series decomposition: the STL method

It is widely recognised that environmental time series exhibit complex patterns combining trend, seasonality, outliers and noise. A robust and accurate decomposition of these variables can provide insight into time sequences from different perspectives and enable further analysis including anomaly detection, forecasting and classification. This approach is crucial in many fields such as hydrology, particularly for runoff forecasting systems (Ma et al., 2025), water quality assessment (Esterby, 1993), ecology (Balazs & Chaloupka, 2004; Chaloupka, 2001), atmospheric science (Carslaw D.C., 2005), and meteorology, as well as the detection of groundwater level fluctuations (Shamsudduha et al., 2009). Accurate short-term flow forecasting and the identification of key driving factors are essential for assessing and managing available water resources.

Although long-term projections are valuable for planning purposes, short-term forecasting poses a particular challenge due to the need to capture the rapid evolution of atmospheric and hydrological processes (Wen et al., 2020). Applying this differentiation if the time series is whole is challenging, as the signal components overlap, masking one effect from another.

Among many seasonal-trend decomposition methods, the most classical one is the STL (Seasonal-Trend decomposition using LOcal regrESSion) which breaks down a time series into three components as follows (Alfio et al., 2024; Lafare et al., 2016):

$$Yt = Tt + St + Rt \qquad (5.1)$$

where Yt is the observed value of the time series; Tt is the trend component; St is the seasonal component; Rt is the residual component.

Generally, trend captures smooth long-term change of the overall data. For instance, it may show a decrease or an increase in air temperature over time relative to a given period. Conversely, the seasonality describes regular and predictable patterns at fixed periods. For rainfall regimes, it identifies wet and dry periods. Finally, the residual contains short-term, irregular or extreme fluctuations, typically centered around zero. Residuals could be interpreted as instrumental anomalies,

noise, non-systematic variability or generally the unpredictable component of a signal linked to the occurrence of extreme events that cannot be explained by the trend and the seasonal factor. In detail, STL is a flexible, non-parametric method that iteratively uses locally weighted regression to fit a smooth curve through the time series data, proving to be very effective in handling non-linear relationships, non-stationary data and outliers (Alfio et al., 2024; Cleveland et al., 1990; G. Zhang et al., 2024).

Given these assumptions, the proposed approach enables the investigation of hydrogeological variables, thus improving the comprehension of groundwater response to climatic influences and, consequently, the propagation of these effects on landslide movements (Lafare et al., 2016). Since baseflow is prevalent in large and porous aquifer systems, seasonal and long-term variations can mask the effects of random recharge, particularly when bivariate time series analyses are applied, such as CCF. For this reason, residual component analysis is essential in order to avoid information loss, after removing seasonal cycles as well as trend components (Chiaudani et al., 2019).

In order to achieve this objective, the investigated time series (spring parameters, snow, rainfall, landslide displacements) were decomposed according to the STL technique for Champlas du Col and Thures sites. Before applying STL decomposition, the hourly water level, temperature and EC data from the Cordeminas and Thures 2 springs have been processed using a Kalman filter (Welch & Bishop, 1995) to remove high-frequency noise while preserving the underlying signal, and then aggregated into daily values. This preliminary step proved that the original datasets are relatively clean and free of unrealistic values, except for EC at Thures, where an instrumental malfunction was identified. For this parameter, a more rigorous correction procedure was implemented on the hourly series to process outliers accurately. Specifically, the hourly EC data were cleaned using a Kalman filter and then decomposed into trend, seasonal and residual components using STL. Outliers were detected in the residual pattern using the interquartile range (IQR) criterion and thereafter removed. The entire series was then reconstructed by summing the cleaned trend, seasonal and residual components, and converted to daily values. Finally, the missing data were interpolated using a second-order polynomial fit (Figure 5.1), resulting in a physically consistent, quality-controlled dataset suitable for further analysis.

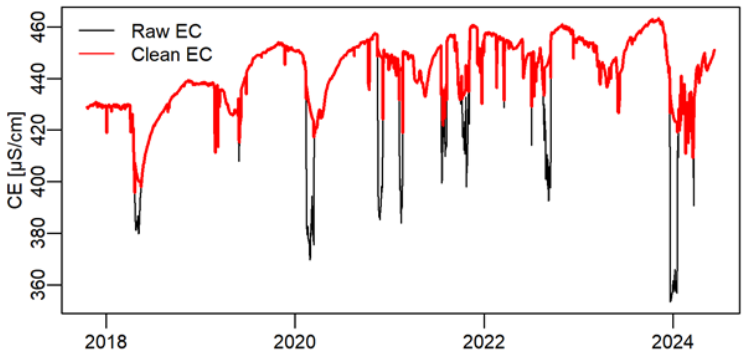

Figure 5.1 Comparison of raw and cleaned EC for Thures 2 spring.

5.2 Regression-based forecasting model

In this section, the displacement time series are analysed to identify the main factors governing landslide movement and to support the construction of a prediction model (Duan et al., 2023).

Following a decomposition-prediction-reconstruction strategy (Zhou et al., 2025), the landslide displacements and all potential predictors are first decomposed with the STL approach. To improve the accuracy and efficiency of the forecasts, all candidate driving factors are selected by applying cross-correlation to the target component to determine the maximum CCF and associated time lag. These factors are then modelled using regression analysis. Finally, the predictor components are recombined to obtain the total predicted displacement. Similar approaches have been widely adopted in the literature for rainfall-controlled landslides and deformation mechanism modelling (Hong & Wan, 2011; Jin et al., 2024). In this study, the time lags controlling the displacement response to each explanatory variable are treated as model parameters that require calibration. This adjustment procedure is commonly employed in hydrology to improve the reliability of simulations and ensure that predicted time series accurately reproduce the observed dynamics (Montanari & Toth, 2007).

Numerous authors have emphasised that the predictive skill of both physics-based and data-driven hydrological models (Liong et al., 2000) critically depends on careful calibration and optimisation of parameter sets and input selections, which are often guided by sensitivity analysis (Cloke et al., 2008). Nevertheless, such calibration efforts are only meaningful when enough long and simultaneous datasets of displacement and all relevant influencing factors are available. This limitation is frequently highlighted in studies of landslide time series prediction (Z. Wei et al., 2019).

Building on this rationale, the adopted workflow (Figure 5.2) is a stepwise procedure that combines cross-correlation analysis, a constrained delay search, predictive evaluation through train–test time splits, and likelihood-based model selection. The proposed approach thus explores model sensitivity under different parameterisations and assesses predictive performance on previously unused data.

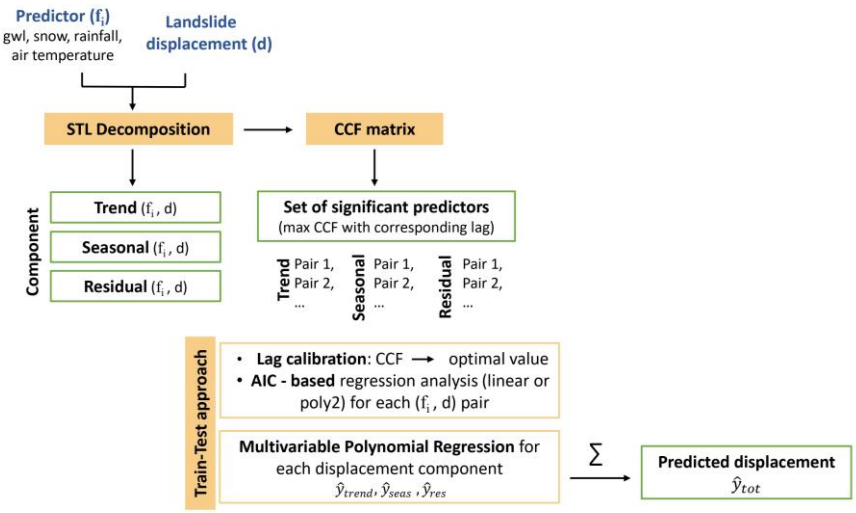

Figure 5.2 Landslide displacement prediction workflow.

The main steps are described as follows:

a. Pre-processing and time series decomposition

All potential predictors (groundwater level, air temperature, snow coverage, cumulative precipitation) and displacement time series were collected into a dataset with a daily time step to ensure temporal coherence. Each time series was then decomposed into trend, seasonal, and residual components using STL method. This stage allows the short-term, seasonal and long-term variability of predictors and displacements to be treated separately, and enables process-based pairing between explanatory variables and slope response (e.g. seasonal snow versus seasonal displacement, trend of groundwater level versus trend of displacement).

b. CCF analysis

The cross-correlation function (CCF) was computed according to the Eq. (3.2) for each predictor-displacement pair within a specified time lag range to quantify their relationship and associated response time. The lag is expressed in days and mainly reflects the common variability of the hydrogeological parameters involved. For the trend components, the CCF was evaluated over lags of at least 150 days to capture long-term behaviour. Conversely, for the residual components, which are characterised by more impulsive variations, a shorter lag window (30 days) was adopted. The analysis returned a correlation matrix showing the maximum CCF for each pair. The most significant predictors were then identified for CCF values close to 1, and the lag corresponding to the maximum CCF was used as an initial and physical plausible estimate of the system response delay.

c. Construction of a lag search window

The lag corresponding to the maximum CCF coefficient represents the average landslide displacement response, but it does not necessarily optimise predictive skills (Box et al., 2015). Therefore, for each predictor-response pair, a local search

window is defined around the CCF-based lag k (e.g. ±60-100 days). Within this window, a lagged predictor series is built as $f_{lag} = f(t - k)$ and then paired with the corresponding displacement component $d(t)$.
The purpose of this analysis step, based on a calibration approach, is to identify an optimal delay that improves the predictive performance of the model while avoiding the analysis of unrealistic parameter values (Cloke et al., 2008; Montanari & Toth, 2007).

d. Optimal lag selection based on Train - Test validation

To ensure that the lag calibration is driven by predictive performance, each potential lag is evaluated using a chronological training and testing approach.
For each predictor-response pair and each candidate lag, the time series f_{lag}, $d(t)$ is divided into a training (60%) and a testing (40%) subsets within the search window.

For each candidate lag, two single-predictor regressions are fitted to the training subset only: (i) a linear model and (ii) a second-order polynomial and then compared using the Akaike Information Criterion (AIC). For a model with maximised likelihood L and p free parameters, the AIC is defined as follows (Akaike, 1973):

$$AIC = -2\log L + 2p \qquad (5.2)$$

which balances goodness of fit and model complexity, avoiding overfitting. The goal is to select the model with the lowest AIC value for each predictor. Higher-order polynomials are only adopted when they substantially improve upon simpler models, as proven by a reduction in AIC of at least 10 units. Accordingly, the analysis was restricted to second-degree polynomial to avoid overfitting.

The predictive accuracy of the selected model is then assessed on the test subset using the Root Mean Square Error (RMSE) (Hodson, 2022) for a sample of n observations y_i (i = 1,2,..., n) and n corresponding model predictions $\hat{y}_i$:

$$RMSE = \sqrt{\frac{1}{n}\sum_{i=1}^{n}(y_i - \hat{y}_i)^2} \qquad (5.3)$$

The optimal lag for a given explanatory variable–response pair is finally defined as the lag that minimises the test RMSE among all candidate lags in the search window. This procedure is consistent with standard hydrological verification frameworks, in which model setting and inputs are evaluated based on their performance with data that was not used in the calibration process (Liong et al., 2000; Wagener & Gupta, 2005).

e. Regression model fitting and likelihood-based structure selection

Once the optimal lag has been identified, a Multivariable Polynomial Regression model (MPR as detailed in Appendix C) is then built for each component, using all the associated lagged predictors simultaneously. A set of candidate multivariate models, corresponding to different combinations of linear or quadratic terms for

each regressor, is explored on the training subset. For each combination, a model is fitted to the training data and evaluated using the AIC. The best multivariate structure for each component is selected as the one with the lowest AIC value on the training subset, with RMSE on the test subset used as a secondary criterion in case of very similar AIC values. This ensures a balance between parsimony and predictive skill.
Finally, the selected multivariate model for each component is used to generate predictions for validation on the training and test subsets, and to reconstruct the full predicted time series of that component over the entire observation period.

f. Reconstruction of total displacement

For each day *t*, the predicted displacement components - trend, seasonal, and residual - are obtained from their respective multivariate regression models. The predicted displacement time series is obtained through the additive reconstruction of the modelled components. It is noteworthy that when multiple predictors contribute to the same component, their influence is combined within the same multivariate regression model through the estimated regression coefficients (Appendix C). The resulting component prediction is therefore a coherent multivariate estimate rather than a simple arithmetic mean of independent single-factor fits.

g. Global performance evaluation

The total predicted displacement is compared with the observations over the entire dataset. After fitting, model performance is quantified using some of the common indicators (Hrehova et al., 2025) employed to evaluate the accuracy of regression model. The RMSE (Eq. 5.3) and the coefficient of determination (R^2) are computed on the total dataset and on the training and testing subsets separately. The R^2 (Helland, 1987) measures the percentage of variation in the response variable $\hat{y}_i$ explained by the variable y_i. Thus, it is an important measure of how well the regression model fits the data and it is defined as:

$$R^2 = 1 - \frac{SSE}{SST} = 1 - \frac{\sum_{i=1}^{n}(y_i - \hat{y}_i)^2}{\sum_{i=1}^{n}(y_i - \bar{y})^2} \qquad (5.4)$$

where *SST* is the total sum of squared deviations in y_i from its mean $\bar{y}$ ans *SSE* denotes the sum of squared residual errors ($y_i - \hat{y}_i$).
The R^2 value is always between 0 and 1. An R^2 value of 0.8 or above is very good and a value of 0.6 or above may be satisfactory in some applications. However, errors in prediction may be relatively high in such cases. When the R^2 value is 0.5 or below, the regression explains only 50 % or less of the variation in the data so prediction may be poor (Ostertagová, 2012).

5.3 Results and Discussion

5.3.1 STL-based Autocorrelation and Cross-Correlation analyses

The results of the STL analysis (Table 5.1) were investigated using the ratio *r* of the variance of each component to the variance of the original signal (Alfio et al., 2024; Colyer et al., 2022).Values of *r* close to 1 indicate that the corresponding component accounts for a larger share of the total variance and can therefore be interpreted as a dominant driver of the observed dynamics. For both springs, temperature is predominantly controlled by the seasonal component, while other variables exhibit mixed behaviour.

The water level at the Cordeminas spring is driven by both trend and residual variability, whereas the level at Thures shows a near-balance among components. Additionally, the EC demonstrates similar contributions from all components at Cordeminas, whereas it is trend-dominated at Thures, suggesting more significant low frequency hydrochemical fluctuations.

Table 5.1 Summary of STL results for Cordeminas and Thures 2 springs.

Spring	Parameter	*r*(trend)	*r*(seasonal)	*r*(residual)
Cordeminas	Level	0.400	0.145	0.366
	EC	0.307	0.267	0.360
	Temperature	0.046	0.889	0.102
Thures 2	Level	0.301	0.323	0.298
	EC	0.523	0.185	0.289
	Temperature	0.079	0.894	0.018

The graphs obtained for each spring (Figure 5.3 and Figure 5.4) show how the variables of interest generally respond to the annual snowmelt cycle, while the residuals are linked to significant precipitation events that have caused some disturbances within the time series. After STL decomposition, Q-Q plots are a diagnostic tool used to determine whether the residuals can be treated as approximately white and normally distributed noise (W. Ahmed et al., 2025; Feng et al., 2020). Therefore, once the trend and seasonality have been removed, it was checked whether the residuals behave as an unstructured random component with nearly constant variance over time. By comparing the empirical quantiles of the residuals with the theoretical quantiles of a normal distribution, Q-Q plots can reveal heavy tails, skewness or outliers, which would suggest a deviation from normality (reference line in the Q-Q plot in Figure 5.5 and Figure 5.6). When the points closely follow the reference line, the residuals can be considered to be approximately normal. Conversely, systematic deviations, particularly in the tails, suggest that the STL has not effectively captured the seasonal components or that further treatment of extreme values is required.

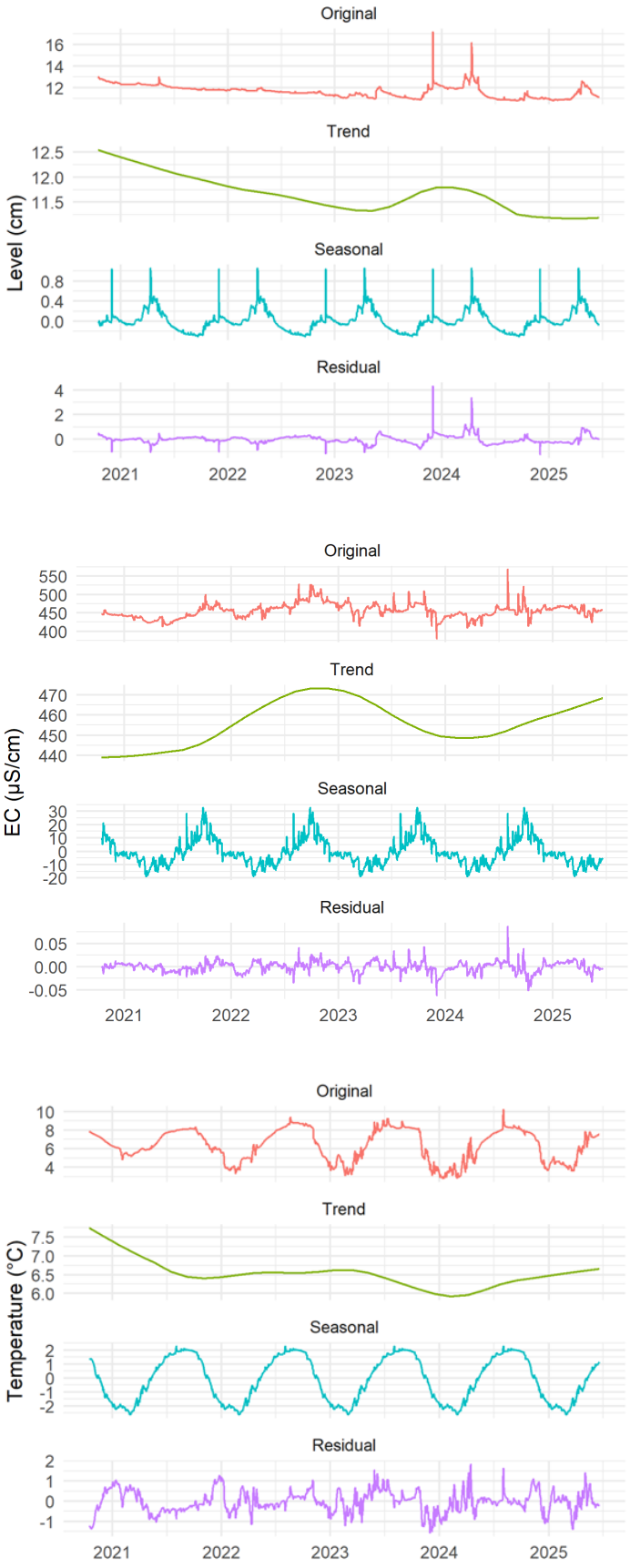

Figure 5.3 STL decomposition results of Cordeminas spring parameters.

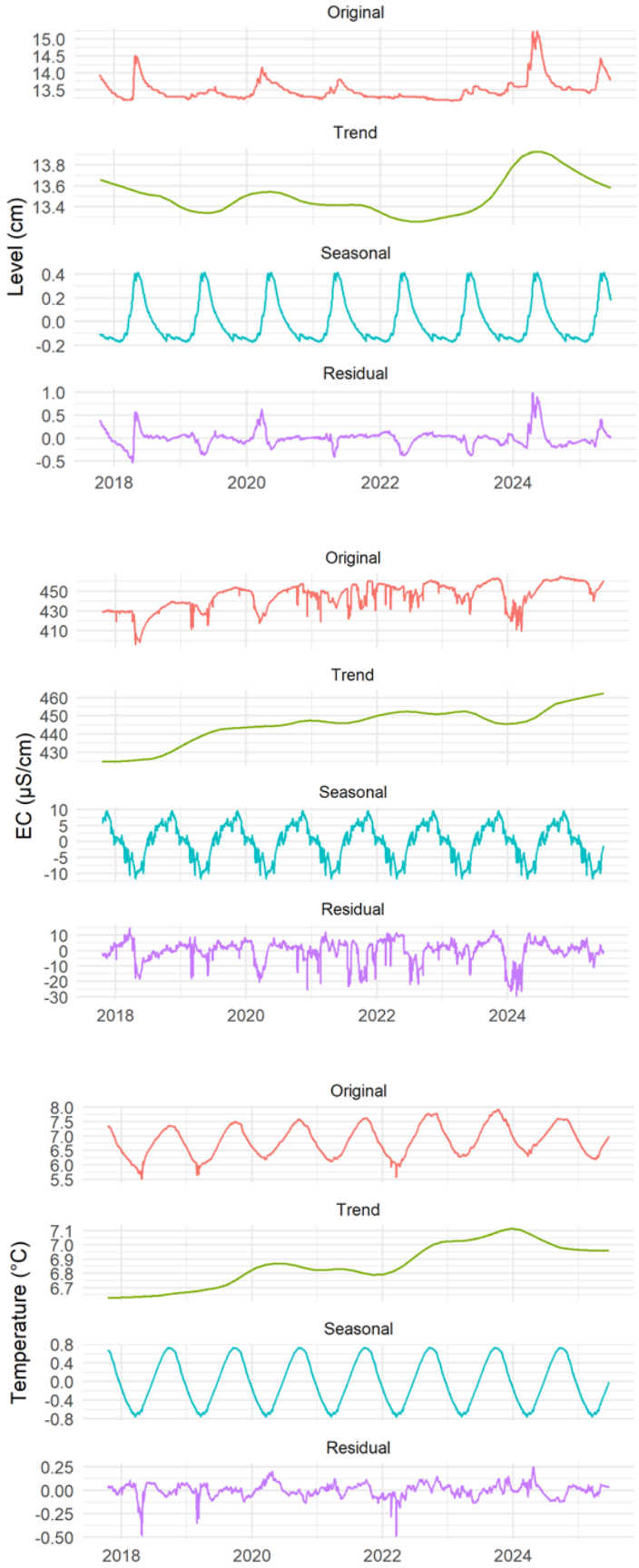

Figure 5.4 STL decomposition results of Thures 2 spring parameters.

Adopting the same approach as in Section 3.3.2, the ACF analysis is applied to both the raw time series of the spring parameters and their respective residuals Figure 5.5 and Figure 5.6) to determine whether the residuals contain cyclical patterns that the STL method was unable to filter out or if they are just noise. Notably, despite the identical ACF trend for temperature at both sites, which exhibit decorrelation in about 100 days, the ACF curve for Cordeminas shows a slight decrease in level and CE than Thures. However, ACF analysis of the residuals reveals decorrelation curves for level and EC that exhibit a sharp decrease, indicating a connection to random events. This trend is likely due to instantaneous variations caused by the occasional occurrence of intense, concentrated recharge events. The Cordeminas spring system is in fact highly sensitive to sporadic events. In contrast, the T curve appears to be barely affected, probably because temperature remains almost constant due to the slight difference between infiltrated water and the volume of groundwater stored within the aquifer system. This is particularly evident in Thures, where the residual curves show a smoother trend and a less sharp decrease than in Cordeminas.

The ACF values for Thures are quite higher (outside the limits of significance), indicating the persistence of cyclical patterns as shown by the curve of spring level residuals. This behaviour can be explained physically, as the Thures system is more resilient to random rainfall, as demonstrated by the absence of spikes, and is more influenced by regular snowmelt patterns. This suggests that significant water storage occurs due to the large recharge area and complex geometry of the aquifer, and that groundwater is gradually released from it. The distribution of snow cover thickness is characterised by an intermittent pattern linked to the alternation of snowy (winter) and non-snowy periods. Conversely, the precipitation regime appears to be more random than snow cover patterns. Given this assumption, the variability of the spring parameters and displacement time series can be explained by the combined effects of precipitation (the random component) and snowmelt (the systematic component).

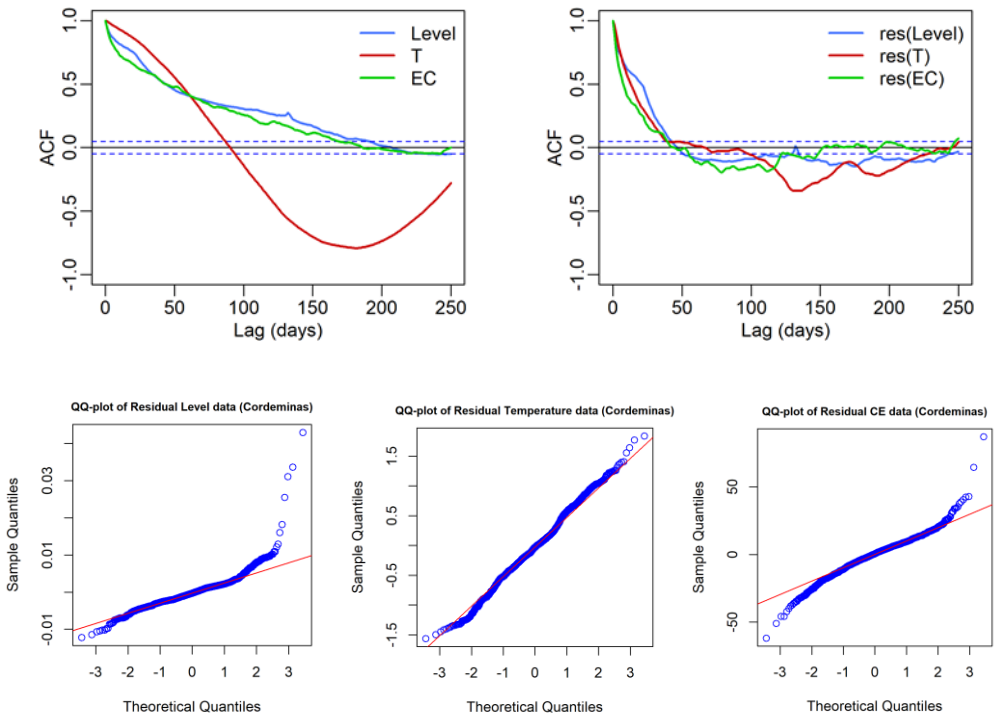

Figure 5.5 Cordeminas spring parameters: ACF curves of original times series and Q-Q plots of the residuals (the normal distribution is depicted as a red reference line).

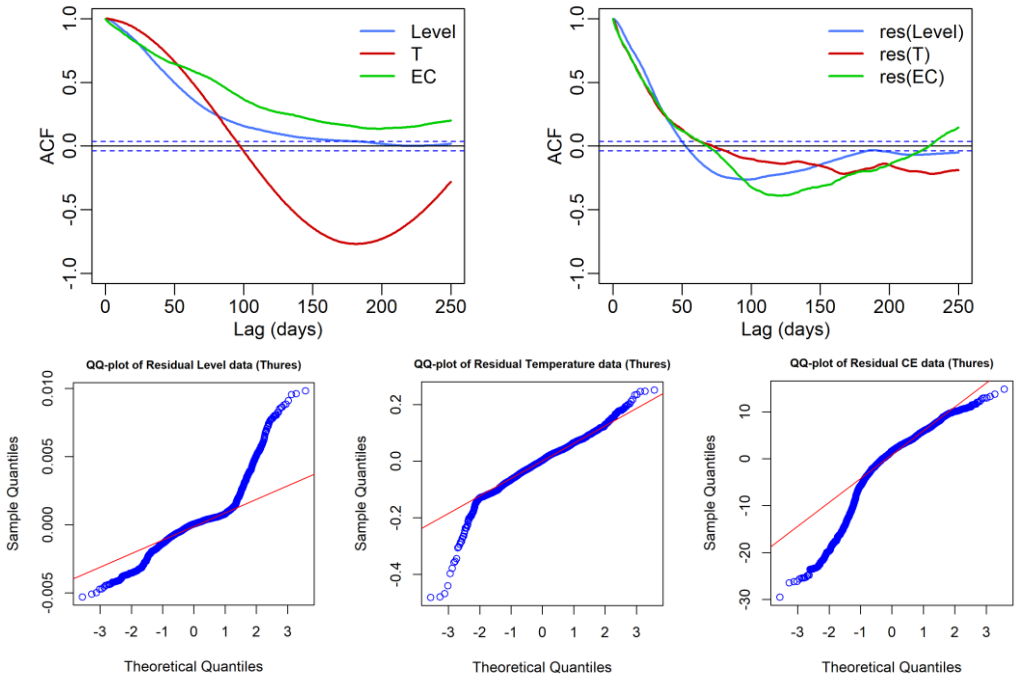

Figure 5.6 Thures 2 spring parameters: ACF curves of original times series and Q-Q plots of the residuals (the normal distribution is depicted as a red reference line).

The cross-correlation function (CCF) was applied to the seasonal and residual time series in order to evaluate recharge contribution separately, with the aim of integrating the results discussed in Section 3.4.1. The CCF curves in the Figure 5.7 are characterised by very high correlation values, suggesting a significant influence of the snow parameter on the aquifer regime and reactivation of movements. In particular, the shape of the curves shows that temperature and conductivity behave differently respect to levels and displacements. This is because the infiltration process resulting from reduced snow cover replenishes the aquifer, causing an increase in water levels and landslide activity. Conversely, the mixing of stored groundwater (base flow) and recharge water from snowmelt leads to a dilution effect, accompanied by a decrease in temperature and conductivity values.

The CCF was also applied to the residual component of the spring parameters using raw precipitation time series as input (Figure 5.8). The very low CCF values in both the original (Figure 3.6) and residual time series confirmed that precipitation contributes for only a limited amount of the overall recharge of the aquifer and that random precipitation only influences the residual behaviour of the Cordeminas and Thures source parameters.

However, the transient behaviour of precipitation inflow has made it possible to identify different recharge modes, which are fully or partially activated during heavy rainfall events. CCF analysis of the residuals confirm that the Cordeminas spring system (Figure 5.8a) is more impulsive and sensitive than the Thures system (Figure 5.8b). Furthermore, the deformations are poorly correlated with rainfall when considering individual events in both cases. Consequently, in order to ensure a more suitable and consistent assessment, it is required to consider the cumulative precipitation over a given time window.

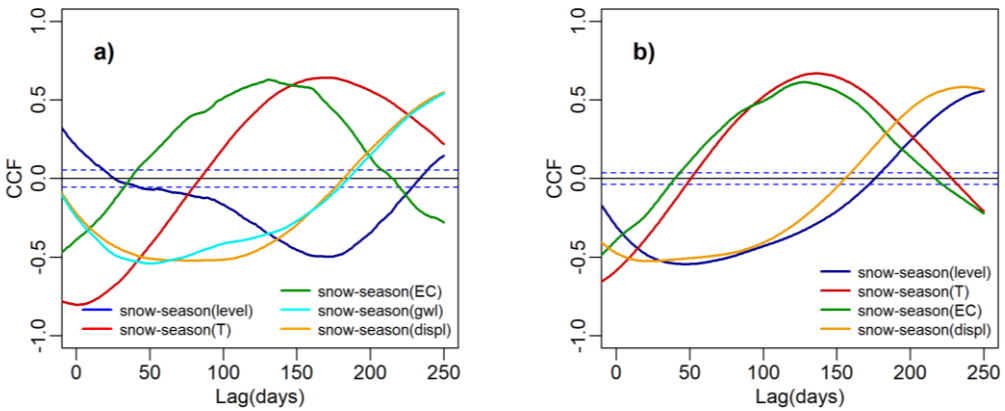

Figure 5.7 Raw snow-seasonal spring parameter CCF curves: a) Champlas du Col and b) Thures.

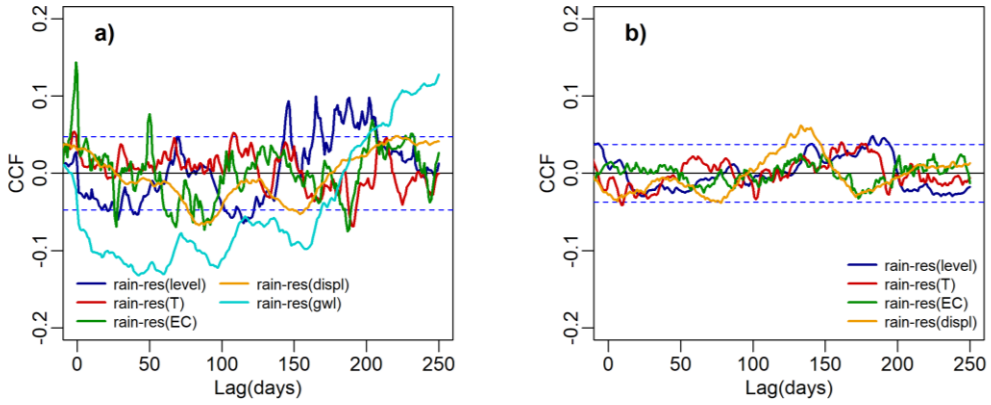

Figure 5.8 Raw rainfall-residual spring parameter CCF curves: a) Champlas du Col and b) Thures.

5.3.2 Observed and Predicted Displacement

Several key points can be highlighted from the reported findings for both sites. The observed and fitted time series are visualised, by distinguishing between the training and test samples, in order to assess whether the lag-optimised model correctly reproduces the timing and magnitude of displacement fluctuations, while maintaining performance on the test data. For the analysis purposes, the Champlas du Col dataset is limited to 10 June 2024 due to the constrained availability of the S6SSTC1A inclinometer time series (see Section 3.3.1). Conversely, the Thures dataset has been updated to the field measurement conducted on 20 June 2025.

Firstly, the relationships between hydrometeorological predictors and displacement components are clearly non-linear. As the primary objective of this analysis is to describe landslide movement patterns based on the most significant variables, it is reasonable to restrict the predictive analysis to second-degree polynomials, as higher-degree models could lead to overfitting. For each displacement component (trend, seasonal, residual), a multivariate regression model is constructed using explanatory variables with high maximum CCF values, wich are included as either linear or quadratic terms. This multi-predictor formulation considers the combined effects of groundwater levels, snow coverage and antecedent rainfall, rather than focusing on a single regressor, improving both the physical interpretability and, in several cases, the statistical performance of the regression (Ren & Ghazali, 2025; L. Wang et al., 2023).

At Champlas du Col (see Figure 5.9 and Table 5.2), cross-correlation analysis shows that seasonal displacements are strongly correlated with the seasonal component of groundwater levels (max CCF = 0.96, lag CCF = 6 days) followed by snow accumulation (max CCF = 0.91) and cumulative precipitation over 30 days (max CCF = -0.75). Meanwhile, the residual component of the groundwater level exhibits a moderate correlation with residual displacements (max CCF = 0.60). Despite the relatively weak correlation between long-term displacement variations and the snow trend (max CCF of 0.49), this variable remains the most informative predictor at the trend scale. During the lag calibration phase, the optimal delays

obtained through train–test optimisation are typically very close to the lags associated with the maximum CCF. For instance, the delay of the seasonal groundwater signal is precisely 6 days (lag CCF = lag opt) and the residual groundwater–displacement pair exhibits a lag of 15 days in both analyses. Regarding the relationship between the snow trend and trend displacement, optimisation adjusts the delay from 84 to 111 days. These relatively minor adjustments suggest that the global cross-correlation structure in Champlas du Col already accurately captures the average response time of the system and that performance-based refinement primarily involves local fine-tuning rather than a radical redefinition of the time alignment. From a physical perspective, this behaviour implies that the characteristic response time of the slope is relatively stable, despite the fact that the displacement magnitude is highly variable and can only be partially explained by the regressors. Seasonal displacements can be described by a second-order multivariate polynomial regression model, which achieves consistently high performance with R_{train}^2=0.96 and R_{test}^2=0.96. However, the trend component is less well defined, as the polynomial model linking the snow to the displacement trends produces relatively modest coefficients of determination (R_{train}^2 = 0.28, R_{test}^2 = 0.17). This suggests that the long-term behaviour of the Champlas du Col slope cannot be explained solely by snow. The residual component fits the training set reasonably well (R_{train}^2 = 0.52), but has very low predictive power for the test set (R_{test}^2 = 0.06), proving that short-term dynamics are highly variable.

When the total predicted displacement is reconstructed (Figure 5.10), the resulting model explains nearly 45% of the variance in the total displacement rate (R^2 = 0.45), with R_{train}^2 = 0.55 and R_{test}^2 = 0.36 and RMSE=0.015. These values demonstrate that even when additional predictors are selected from the CCF matrix, the Champlas du Col landslide exhibits complex and partly unpredictable kinematics. In this sense, the multivariate polynomial model provides a useful, albeit approximate, description of the system.

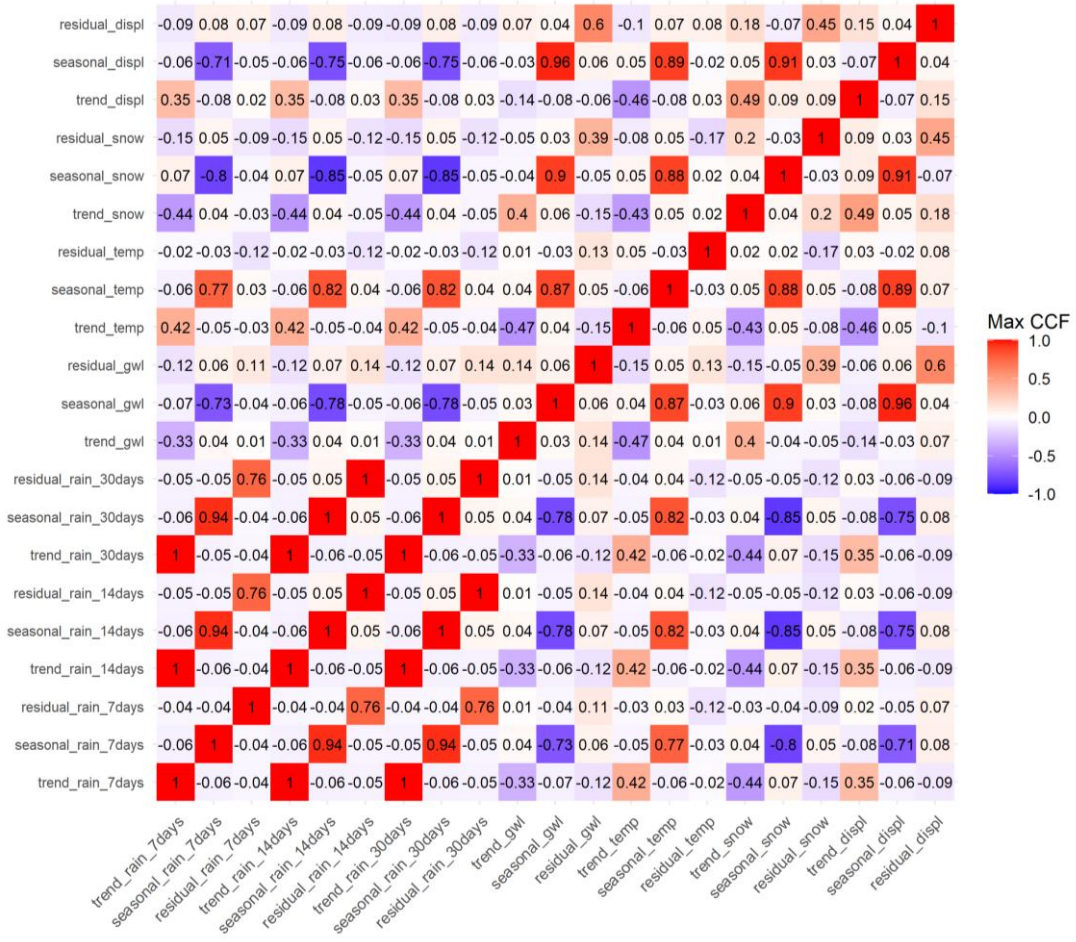

Figure 5.9 Cross-correlation coefficient matrix for Champlas du Col.

Table 5.2 Summary of the prediction results for Champlas du Col. The model equations (reference in bracket) and the estimated regression coefficients are reported in Appendix C.

Pair	Max CCF	Lag CCF	Lag opt	Model	R^2_{train}	R^2_{test}
Trend_snow, trend_displ	0.49	84	111	y_{trend} Eq. (C.1)	0.28	0.17
Seasonal_gwl, seasonal_displ	0.96	6	6	$y_{seasonal}$ Eq. (C.2)	0.96	0.96
Seasonal_snow, seasonal_displ	0.91	88	84			
Seasonal_rain_30days, seasonal_displ	-0.75	105	110			
Residual_gwl, residual_displ	0.60	15	15	$y_{residual}$ Eq. (C.3)	0.52	0.06

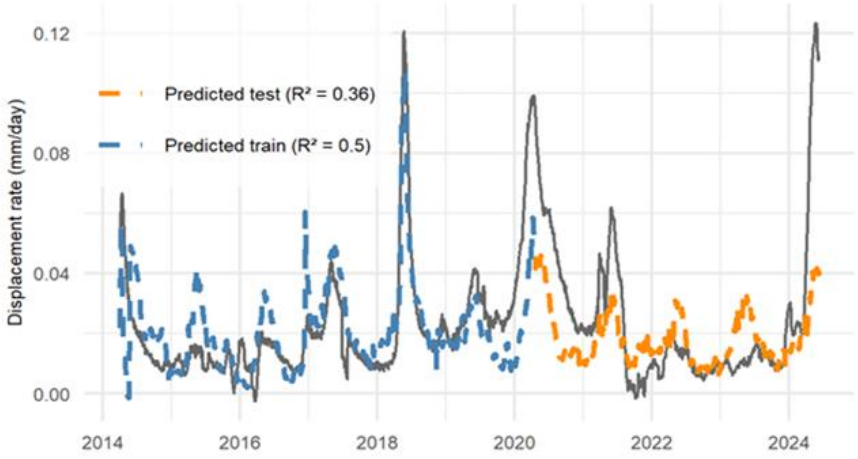

Figure 5.10 Observed displacement rates and predicted values for the training and test datasets at the Champlas du Col landslide.

At the Thures site (see Figure 5.11 and Table 5.3), the degree of cross-correlation between the predictive and displacement components is generally higher than at Champlas du Col, suggesting a more consistent coupling between the identified forcing factors and the slope response. The seasonal and trend components of spring water levels exhibit strong correlations with their corresponding displacement components (max CCF of 0.98 and 0.89, respectively), while the residual groundwater component remains strongly linked to residual displacements (max CCF = 0.71). A meaningful association with the seasonal snow is detected (max CCF = 0.86), and the displacement trend is closely dependent on 14-day precipitation long-term variability (max CCF = 0.82). Unlike the previous case, lag optimisation in Thures results in more significant adjustments to the maximum lag, particularly for trend-scale pairs. For example, the lag for the trend-level pair increases sharply from 45 to 193 days, whereas for the trend-precipitation pair it rises from 98 to 118 days. Seasonal pairs show only slight variations (from 21 to 22 days for the spring, and from 120 to 116 days for snow), whereas the lag between groundwater and residual displacement ranges from 27 to 37 days. These results suggest that the temporal alignment between the forcing and the most predictive response, as determined by train-test optimisation, corresponds to an effective memory time that is longer than that indicated by the raw cross-correlation for the trend components. This can be interpreted as evidence that long-term displacement responds to the gradual water accumulation in the fractured medium, changes in pore pressure over time, and progressive weakening along the sliding surface.

In summary, while the CCF reveals the overall linear correlation, the optimal delay identifies the time lags that most accurately align the primary deformation phases with the preceding hydrological conditions. This reveals a multiphase, non-stationary response on a trend scale. Meanwhile, the residual component can be adequately described by a second-order polynomial in groundwater residuals. The seasonal model achieves R_{train}^2 = 0.97 and R_{test}^2 = 0.97, confirming that displacement is mostly explained by the seasonal changes in groundwater levels

and snowfall time series. The trend model, driven by spring level trends and 14-day precipitation, gets a R_{test}^2 equal to 0.84, indicating that long-term displacement behaviour responds non-linearly to groundwater accumulation and previous precipitation. The groundwater displacement residual pair achieves $R_{train}^2 = 0.49$ and $R_{test}^2 = 0.36$, which is consistent with short-term fluctuations and local events that are more challenging to predict.

Aggregating the component forecasts, the final model (Figure 5.12) explains approximately 70% of the variance in total displacement ($R^2 = 0.70$), with $R_{train}^2 = 0.53$ and $R_{test}^2 = 0.69$ and RMSE=0.004. This indicates a robust and stable predictive relationship with limited overfitting, as the test performance is comparable or even slightly higher. Overall, the Thures landslide exhibits a highly predictable kinematic response to the selected hydrological drivers, particularly variations in spring levels, which remain the most informative descriptors of displacement across all components.

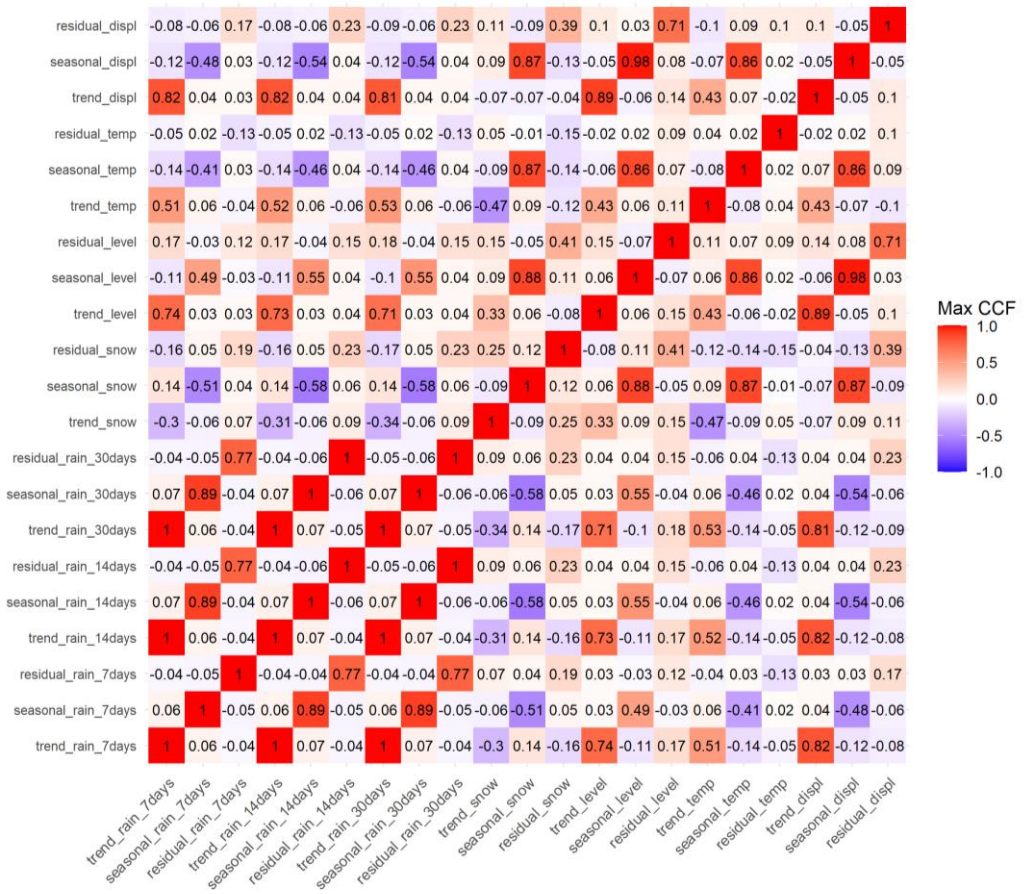

Figure 5.11 Cross-correlation coefficient matrix for Thures.

Table 5.3 Summary of the prediction results for Thures. The model equations (reference in bracket) and the estimated regression coefficients are reported in Appendix C.

Pair	Max CCF	Lag CCF	Lag opt	Model	R^2_{train}	R^2_{test}
Trend_level, trend_displ	0.89	45	193	y_{trend} Eq. (C.4)	0.45	0.84
Trend_rain 14days, trend_displ	0.82	118	98			
Seasonal_level, seasonal_displ	0.98	21	22	$y_{seasonal}$ Eq. (C.5)	0.97	0.97
Seasonal_snow, seasonal_displ	0.86	120	116			
Residual_level, residual_displ	0.71	27	37	$y_{residual}$ Eq. (C.6)	0.49	0.36

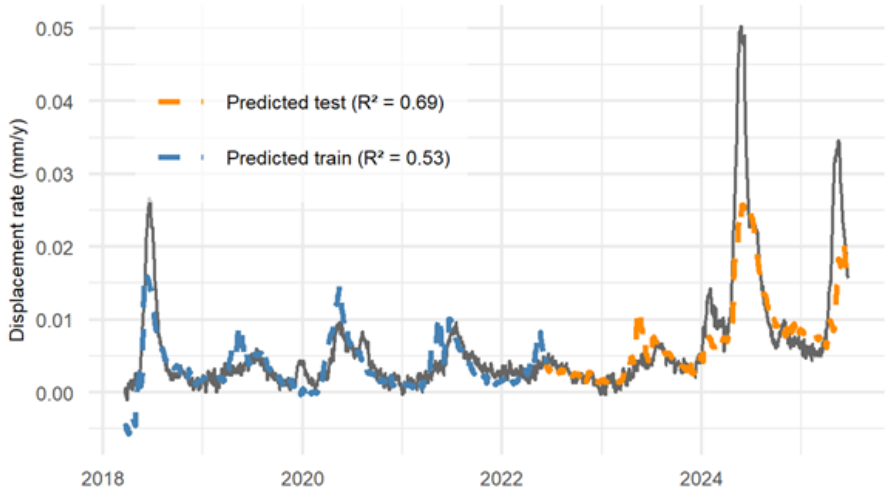

Figure 5.12 Observed displacement rates and predicted values for the training and test datasets at the Thures landslide.

5.4 Conclusions

The application of multivariate component models, which employ a series of explanatory variables for each selected component derived from the CCF matrix, brings two key advantages. From a statistical perspective, the multiple predictor formulation typically controls model complexity, thereby enhancing the performance of the individual components, especially on the independent test subset (e.g. the seasonal and trend components in Thures and the seasonal component in Champlas du Col). Furthermore, the model explicitly recognises that slope kinematics are controlled by simultaneous hydrometeorological processes (e.g. groundwater levels, snow loads, and cumulative precipitation) rather than by a single, dominant variable. In Champlas du Col, seasonal displacement is primarily affected by seasonal changes in groundwater levels, but is also significantly impacted by seasonal snowfall and 30-day precipitation levels. In Thures, however, the trend and seasonal components of displacement exhibit nonlinear responses to spring levels and precipitation indicators.

Overall, the two sites demonstrate of how the same methodological framework — based on time series decomposition, CCF-guided delay identification with train-test refinement, AIC-based selection of linear versus quadratic terms and component-level multivariate regression — can yield significantly different predictive outcomes based on local hydrogeological conditions and landslide kinematics. While statistically significant and physically plausible relationships were identified at both sites, the model is significantly weaker at Champlas du Col site, suggesting that it is subject to more complex and less stationary processes.

Despite the improvements introduced by multivariate polynomial regression and delay optimisation, it is important to note that the proposed model is only approximate. Some of the variability that cannot be described by the implemented model can reasonably be attributed to residual noise or processes not considered in this study. Therefore, applying more flexible approaches, such as machine learning and physically based models (Duan et al., 2023; Ren & Ghazali, 2025), could more effectively capture nonlinearities while maintaining the physical structure and interpretability of the current framework.

Chapter 6

Numerical modelling: Champlas du Col landslide

The work described in this chapter was summarised in the paper "Numerical modelling for hydrogeological analysis: a case study of the Champlas du Col landslide (NW Alps, Italy)", submitted in the journal Engineering Geology and currently under review.

6.1 Introduction

Although significant progress has been made in understanding landslide behaviour, substantial knowledge gaps remain, particularly regarding the role of subsurface hydrology. Parameters such as the soil–water characteristic curve (SWCC), saturated and unsaturated flow regimes, and the rate at which water content varies are critical in determining pore water pressure distribution during infiltration events. However, these factors are not yet fully understood or adequately quantified in many models (Song et al., 2015; L. L. Zhang et al., 2011).

Numerous studies have highlighted the key role of rainfall intensity in triggering slope failures (Marino et al., 2021; Moreno et al., 2024). High-intensity rainfall events can lead to rapid pore pressure development, reduced soil cohesion and a decreased internal friction angle, all of which reduce overall slope stability (Bustamante et al., 2025). In unsaturated soils, the reduction of matric suction and the development of positive pore water pressure are primary failure mechanisms during infiltration (Natalia & Yang, 2025). These findings emphasize the need to consider both saturated and unsaturated flow regimes in any comprehensive slope stability assessment.

Despite growing awareness, developing reliable models to predict the behaviour of deep-seated landslides remains highly complex. This requires integrating of high-resolution geomechanical, hydrogeological and climatic data, often in environments that are both heterogeneous and data-deficient (Schweiger et al., 2019). Therefore, to implement early warning systems and improve risk mitigation policies, it is essential to identify vulnerable areas, characterise the failure mechanisms, and understand the interaction between external triggers and internal slope properties (Phakdimek et al., 2025).

Given these considerations, this study aims to investigate the hydromechanical response of the Champlas du Col landslide, which is subjected to slowly evolving

deformations under different hydro-meteorological conditions, using finite element method analyses on a slope model. Three scenarios were simulated: the spring seasons 2018 and 2024, and the heavy rainfall event in November 2016. The study assessed the transient pore pressure variations resulting from the gradual rise of the groundwater table, coupled with an infiltration model (Amarasinghe et al., 2024), and their effects on landslide displacements pattern. The framework of unsaturated soil mechanics (Mburu et al., 2022; Pirone et al., 2023) was incorporated into the numerical modelling to investigate soil behaviour during rainfall and snowmelt, key hydrogeological processes driving slope movements.

6.2 Data collection

As previously outlined in Section 3.2, a simplified geological cross-section (A-A′) was developed near Champlas du Col and the SP23R road (Figure 6.1).
The slope consists of two main soil layers which will be used to set the spatial domain of the model:

(i) an upper layer of glacial and alluvial deposits, primarily silty sand with gravel;

(ii) a lower layer of fractured calcschists in a clay matrix (of Cretaceous period), overlying the bedrock.

Due to the limited depth of the boreholes (Table 6.1), the thickness of the layers and the depth of groundwater table, ranging between 10 and 20 m along the slope, were estimated by combining borehole data with in-situ geological observations.

Table 6.1 Boreholes along the cross-section A-A'.

ID code	Elevation (m a.s.l)	Depth (m)	Groundwater level (m a.s.l.)
S1	1860	33	1840.2
C1	1760	65	1748
C2	1720	75	1710
SCC3	1590	110	1550

Geognostic surveys ad stratigraphic data reveal a complex system with multiple sliding surfaces, attributed to the presence of the fractured calcschist layer, which contributes to the infiltration of meteoric water inputs. Slope-scale failure is governed by a viscous-plastic mechanism, with creep movements affecting a large portion of the rock mass. As a result, the landslide exhibits a dominant sliding component along several planes of structural discontinuities (Fioraso et al., 2011).

Upstream of the SP23R, displacement occurs along horizons with different hydraulic conductivity, due to the presence of alternating gravel, silt and sand. These incoherent soils, locally enriched by glacial deposits formed during the Last Glacial Maximum, cover the fractured bedrock with an estimated thickness of about

100 m (Figure 6.1b). On the other hand, the lower part of the landslide, toward the valley floor, is predominantly composed of more consistent alluvial deposits.

Because of the heterogeneous nature of surface deformations, landslide displacements of different magnitude are detected. In particular, in the western sector of the landslide, movement rates range between 2 and 4 cm/year, while in the eastern sector, displacements are more pronounced, reaching approximately 6-7 cm/year (Arpa Piemonte, 2023c).

The S6SSTC1A inclinometer and the P6SSTC4 piezometer Table 3.1, which provide cumulative displacement and daily depth to groundwater level values respectively, are used to calibrate the numerical models.

Climatic data, such as daily data on rainfall, snow depth and temperatures, are collected from the nearby Sestriere weather station, selected for its proximity to the study site and its relevance in identifying triggering events for slope movement.

Drilling data for the area are limited in terms of quantitative geotechnical properties, which constrains their use in detailed modelling. Standard Penetration Tests (SPTs) were performed in a few boreholes and limited to the upper 30 m, reducing the overall data resolution. However, Lefranc tests conducted in boreholes S1 and SSC3 provided hydraulic conductivity values of $4.5*10^{-6}$ m/s and $1.07*10^{-5}$ m/s at 20 m depth, respectively. Similar values, $4.5*10^{-6}$ – $1.2*10^{-5}$ m/s were confirmed in nearby sites, with hydraulic conductivity decreasing with depth due to increasing clay content.

To supplement these data, geomechanical properties were retrieved from literature. Monte et al. (2024) provided simple descriptive statistics that have been used to assign the geotechnical parameters to different lithological classes, which in the current case are i) rocks of sedimentary origin and ii) schistose metamorphic rocks. It is necessary to point out that the values given are not suitable for local-scale applications, as they are derived from small-scale cartography and are not capable and reliable to accurately represent local lithotype variations. Nevertheless, they provide a good reference for the purposes of this study. Further data were collected by (Barla et al., 1986), dealing with the experimental determination of some mechanical values for a series of lithotypes, including the calcschists of the Upper Susa Valley.

Cohesion values of 20 to 40 MPa are attributed to the pre-Quaternary basement (calcschists), while values around 40 kPa are assigned to glacial deposits of mixed origin (Fontan, 2022). Assumptions were required for the fractured calcschist blocks in an abundant clay matrix, which shows reduced strength and cohesion due to its structure.

In terms of hydromechanical behaviour, the upper layer has good drainage properties, being composed of compacted sands and gravels, while the lower layer, in contact with impermeable rock, retains more water. This stratification significantly influences infiltration processes and, in turn, slope stability.

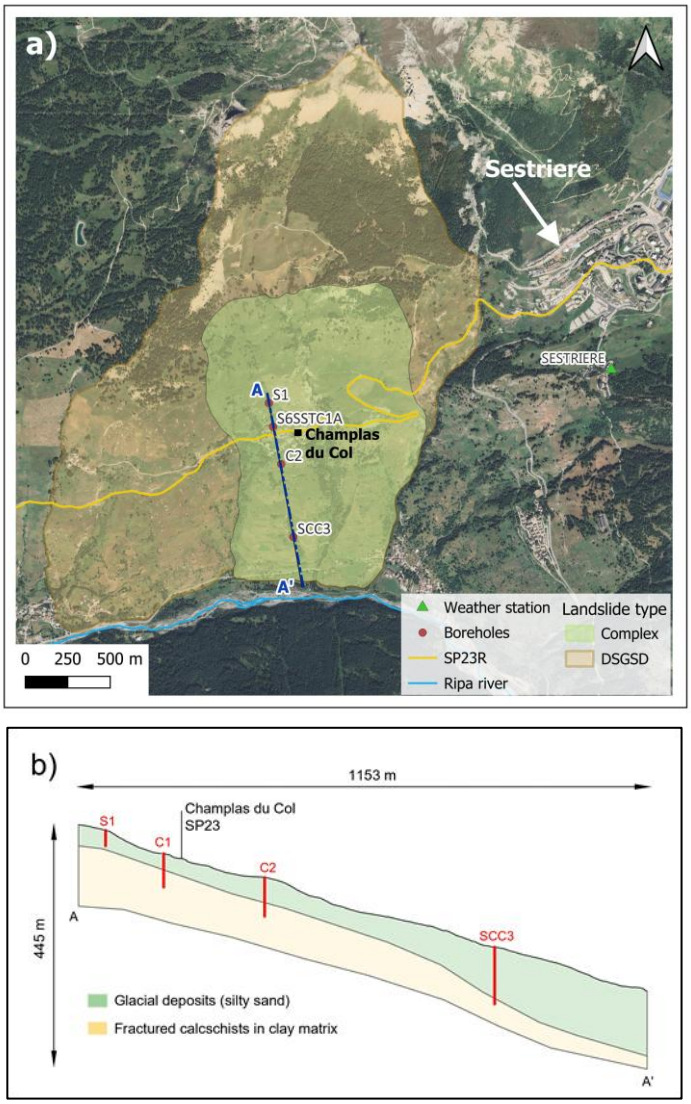

Figure 6.1 (a) Champlas du Col landslide with the boreholes used to define the (b) cross-section A-A'.

6.3 Numerical model set-up

A set of numerical analyses was conducted using Plaxis® 2D software (Version 2024.2.0.1144) to assess the hydromechanical response of the slope under different scenarios. The simulations aimed to model the transient evolutions of pore water pressure, degree of saturation and displacements. Plaxis 2D was selected as the modelling tool due to its proven capability to simulate the combined effects of infiltration processes and soil mechanical properties, as demonstrated in several previous studies (Bustamante et al., 2025 and reference herein).

6.3.1 Slope geometry and boundary conditions

For the purposes of the analysis, the slope geometry used in Plaxis® 2D was derived from the cross-section A-A', extending up to SCC3 borehole, for a total length of 850 m. Based on this geometry, a finite element mesh was generated (Figure 6.2).

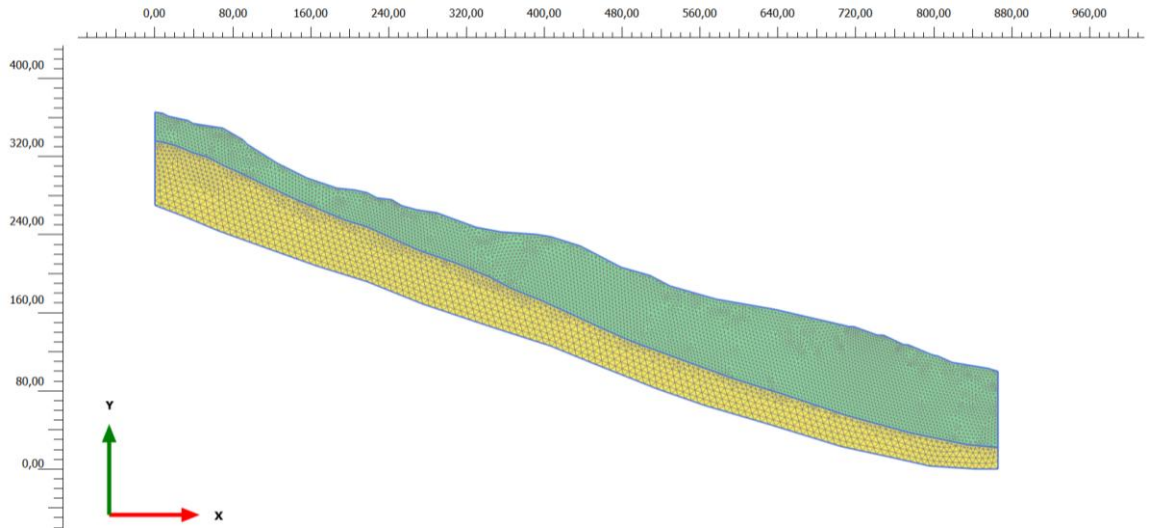

Figure 6.2 Geometry of the model.

With regard to the boundary conditions, the lateral boundaries were set as normally fixed, while the bottom boundary was set as fully fixed. Although the landslide is part of a DSGSD, the limited depth of available boreholes does not provide information on deep deformations. As a result, applying alternative boundary conditions would remain a purely numerical exercise, lacking any validation from field measurements.

For the hydraulic boundary conditions, a zero flow was applied along the bottom edge of the model, representing the impermeable bedrock. A global water level was used to define the initial groundwater head distribution within the slope (Figure 6.3), with values interpolated from borehole stratigraphies and piezometric data. Under seepage condition, water flow was permitted through the lateral and lower boundaries, while the top boundary was configured to simulate infiltration by applying an infiltration rate (q) during rainfall or snowmelt scenarios.

As a result, groundwater flow through the slope was governed by the global water level: a prescribed hydraulic head was applied below the water level, while seepage conditions were imposed above it to simulate unsaturated flow.

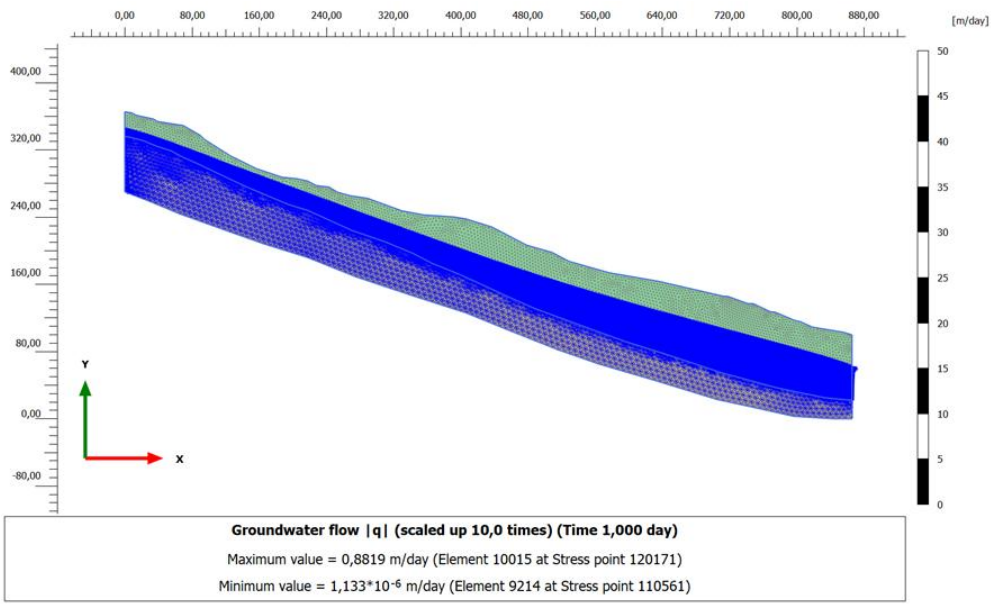

Figure 6.3 Groundwater flow through the model section.

6.3.2 Soil properties and hydraulic model

As previously discussed, selecting appropriate values for the mechanical and hydraulic properties posed a significant challenge during numerical modelling (A. Ahmed & Hossain, 2022). Therefore, a simplified model was adopted, based on available data retrieved from previous studies in the area and geological observations carried out by the authors.

Table 6.2 shows the soil parameters used in the modelling. The spatial distribution of these values was assumed to be uniform across both layers; thus, soil heterogeneity and anisotropy were neglected. Since no site-specific measurements of hydraulic conductivity were available for the study area, the default values suggested by Plaxis® were initially considered reasonably adequate to represent the drainage characteristics of both soil layers, particularly the upper layer, for which a value of 1 m/day was adopted. However, as better explained in Section 6.3.4, these values were subsequently calibrated to reproduce the spring 2018 scenario (Apuani et al., 2007).

Table 6.2 Mechanical and hydraulic parameters adopted in the modelling: unsaturated (γ_{unsat}) and saturated (γ_{sat}) unit weight, porosity (n), Elastic Modulus (E), Poisson's ratio (υ), cohesion (c), friction angle (ϕ), hydraulic conductivity (K) and USDA parameters.

Layer	General			Mechanical				Groundwater					
	γ_{unnsat} (kN/m^3)	γ_{sat} (kN/m^3)	n	E (kN/m^2)	υ	c (kN/m^2)	ϕ (°)	Soil class (USDA)	K (m/day)	S_{res}	g_n	g_a	g_l
Upper	21	23	0.3	100*10^3	0.25	20	30	Sandy loam	1	0.16	1.7	1	0.4
Lower	24	26	0.4	30*10^6	0.2	400	34	Clay loam	0.6	0.23	1.3	1.9	0.5

Plaxis® incorporates modelling of Soil Water Characteristic Curve (SWCC) to simulate the water flow in unsaturated soil.

To facilitate the selection of SWCC parameters, Plaxis® provides predefined datasets for common soil types (Shafieiganjeh et al., 2024). These datasets are based on standardised soil classification systems. In this study, the USDA international classification system was adopted.

The hydraulic parameters used in the USDA dataset are based on the model proposed by Van Genuchten (1980), which describes the hydraulic behaviour of unsaturated soils under the following equation

$$\theta_w = \theta_r + \frac{(\theta_s - \theta_r)}{[1+(\alpha'\Psi)^n]^m} \quad (6.1)$$

$$m = 1 - \frac{1}{n} \quad (6.2)$$

where:

- θ_w, θ_r and θ_s are the total, the residual and the saturated volumetric water content, respectively;
- α', n and m are curve fitting parameters. In particular, α' is the reciprocal of the air-entry value with units of 1/kPa, and n control the shape of the θ_w plot after the sir-entry value.

Similarly, the closed-form relationship for the functional form K(Ψ) is given by the following equation:

$$K_w(\Psi) = K_{sat} \frac{\left\{1-(\alpha'\Psi)^{n-1}\cdot\left[1+(\alpha'\Psi)^n\right]^{-m}\right\}^2}{[1+(\alpha'\Psi)^n]^{\frac{m}{2}}} \quad (6.3)$$

where:

- K_{sat} is the saturated hydraulic conductivity;
- Ψ ist he matric suction.

Plaxis 2D uses g_a, g_n, g_c and g_l and K_{rel} and K_{sat} as input fitting parameters for the functional form S(Ψ) and $K_{rel}(\Psi)$ as explained in the following equations. Especially, the closed-form relationships for the functional forms S(Ψ) and $K_{rel}(\Psi)$ are given by:

$$S(\Psi) = S_{res} + (S_{sat} - S_{res}) \cdot [1 + (g_a|\Psi|)^{g_n}]^{g_c} \quad (6.4)$$

$$K_{rel}(S) = \max\left[S_{eff}^{gl}\left(1 - \left[1 - S_{eff}^{\frac{gn}{gn-1}}\right]^{\left(\frac{gn}{gn-1}\right)}\right)^2, 10^{-4}\right] \quad (6.5)$$

where:

- S_{res} is the residual degree of saturation;
- S_{sat} is the saturated degree of saturation;

- g_a is reciprocal of air-entry value similar to α' with units of 1/m so its value is determined by dividing α' by the unit weight of water;
- g_n controls the shape of the S(Ψ) plot after the air-entry value sog_n= n;
- $g_c = \frac{1-g_n}{g_n}$;
- g_l is a fitting parameter controlling the shape of the $K_{rel}(\Psi)$ plot and affects the effective degree of saturation S_{eff};
- K_{rel} is the relative hydraulic conductivity;
- $S_{eff} = \frac{S_r(\psi) - S_{res}}{S_{sat} - S_{res}}$.

In the context of partially saturated soils, such as those observed in the study area following rainfall events or snowmelt (see Section 6.3.4), the hydraulic conductivity changes with water content. This variation occurs because matric suction affects the amount of water retained within soil pores, thereby influencing the soils ability to transmit water. The major difference between water flow in saturated and unsaturated soils is that the coefficient of permeability (hydraulic conductivity), which is conventionally assumed to be a constant in saturated soils, is a function of degree of saturation or matric suction in the unsaturated soils (Ng & Shi, 1998).

6.3.3 Procedure and calculation phases

The analysis focused on understanding the mechanisms that lead to slope saturation and, thus, contribute to increase slope displacement rates. Two primary processes were identified: (i) the rise of groundwater table within the soil cover and (ii) the downward advancement of a wetting front from the ground surface due to rainfall or snowmelt infiltration.

For this aim, a numerical model was developed to simulate groundwater flow variations induced by rainfall infiltration and snowmelt, according to the following assumptions and settings:

- the Hardening Soil (HS) model (Mohsan et al., 2021; Schanz at al., 1999), an advanced elastoplastic soil constitutive model, was used to describe the long-term plastic behaviour of subsoil. This model is well-suited for predicting of deformations in slow-moving landslide;
- the soils behaviour was modelled under drained conditions;
- slope stability was assessed by applying the strength reduction method;
- in traditional slope stability analyses, rainfall effects are often included by changing the groundwater flow patterns, typically assuming increased pressure heads and a rising water table. For extensive slopes, it is often simplified by assuming a groundwater table parallel to the slope surface that rises uniformly, thereby reducing slope stability (Pisani, 2009). In this study, direct piezometric data were only available from piezometer P6SSTC4. Consequently, the hydraulic head along the slope was extrapolated from this dataset;

- a steady-state seepage condition was assumed as the initial condition prior to conducting transient hydromechanical simulations;
- a fully coupled transient hydromechanical analysis was then performed to simultaneously assess the evolution of pore water pressure and slope displacements induced by infiltration due to rainfall and/or snowmelt.

On this last point, it is worth clarifying a few aspects. The fully coupled flow-deformation analysis considers unsaturated behaviour of soil and the effect of matric suction above the groundwater table. This is the most advanced and realistic type of analysis that considers a reduced hydraulic conductivity and degree of saturation in the unsaturated zone to model the complex behaviour of slopes under rainwater/snowmelt infiltration conditions.

This means that fine-grained soils above the groundwater table may become nearly saturated due to capillary rise, whereas other portions of the unsaturated zoned may remain only partially saturated.

In this case study, capillary effects and matric suction were considered due to the low hydraulic conductivity of the upper layer, characterized mainly by silty sand.

Under steady-state groundwater conditions, tensile pore water stresses (suction) are generated above the groundwater level. Although suction is a real and significant phenomenon, its inclusion in deformation analysis may lead to an artificial increase in soil shear strength (Plaxis - Reference Manual). During rainfall events, infiltration causes a transient redistribution of pore water pressure as water percolates through the soil. prolonged or intense rainfall can lead to the formation of a wetting front, which propagates downward through the slope, reducing soil suction and consequently decreasing soil shear strength (Pisani, 2009).

In Plaxis®, pore pressure distribution is distinguished as follows:

- $p_{water} > 0$ (i.e., $\gamma_{unsat} \leq \gamma \leq \gamma_{sat}$): above the groundwater level, positive pore pressure values may occur due to the suction effect. During infiltration, these values are expected to decrease as the degree of saturation increases;
- $p_{water} \leq 0$ (i.e., $\gamma = \gamma_{sat}$): corresponds to conditions on or below the groundwater level where pore pressures are typically hydrostatic or higher.

6.3.4 Calculation scenarios

To investigate the effects of groundwater fluctuations, coupled with seepage processes, on variations in pore water pressure, ground deformation and slope stability, the numerical model was applied to a selected time window characterised by significant increases in the piezometric level, condition under which landslide acceleration is expected.

To evaluate a range of realistic possible scenarios, the most impactful events were identified from the available precipitation time series recorded over the past decades at the Sestriere weather station. In particular, the selected time periods

ensured temporal overlap between rainfall and snow depth data and the sub-surface deformation measurements provided by the available inclinometer.

As shown in Figure 6.4, which compares snow cover height (cyan bars) with the pattern of landslide displacements (red line), the spring seasons of 2018 and 2024 show marked acceleration of slope movement, primarily attributed to heavy winter precipitation and subsequent spring snowmelt.

Given the typical long-term evolution of slow-moving landslide, the daily displacement is very low (< 0.05 mm), but conversely, more significant displacement rates can be observed over a larger time window. Therefore, the cumulative values were processed by considering the displacement rates over a 30-days moving time window, using the equation (3.3).

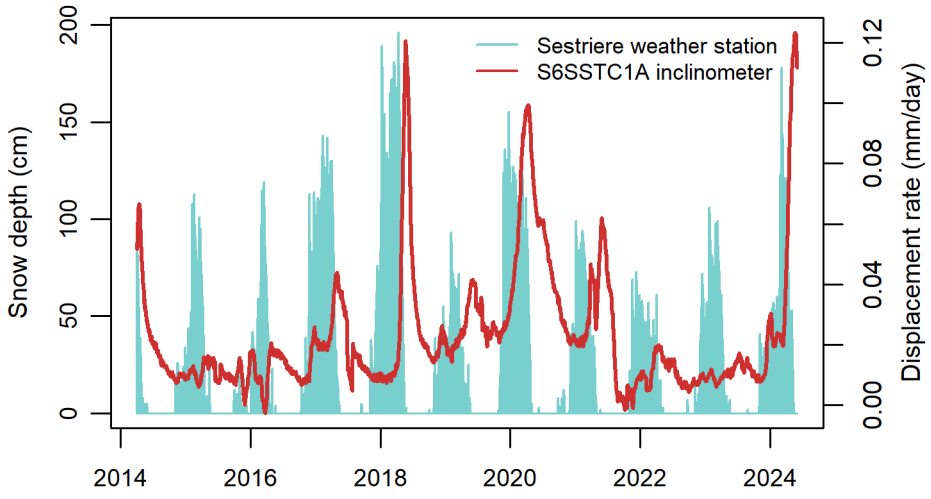

Figure 6.4 Daily cumulative snow depth and landslide displacement rates.

Similarly, to define the effects of a heavy rainfall event, the highest recorded rainfall peak corresponding to 24/11/2016 was selected as a representative extreme scenario (Figure 6.5).

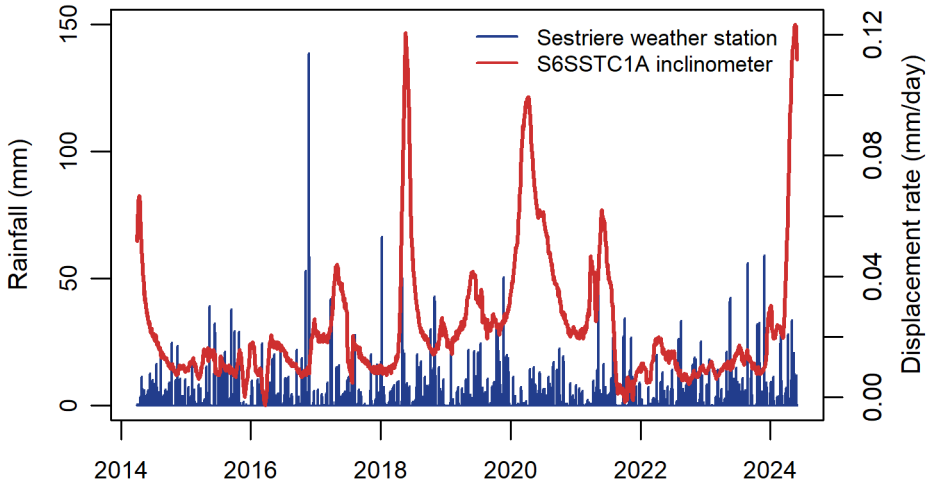

Figure 6.5 Daily rainfall and landslide displacement rates.

The characteristics and simulation details of the selected scenarios are described in detailed in the following sections.

For each of the three proposed scenarios, the numerical simulation was structured into multiple calculation phases to simulate the progressive rise of groundwater level due to rainfall and/or snowmelt infiltration. The selected time windows were then discretised into sequential sub-intervals, creating a cascading infiltration effect. This approach enables a time-dependent assessment of pore water pressure evolution and saturation patterns, starting from pre-event conditions. Furthermore, deformation evolution is tracked to evaluate the landslide response.

Each simulation starts with an initial phase (day 1) to establish the initial stress state of the slope, accounting for soils self-weight, groundwater conditions and the geostatic stress history. This initial stress distribution was generated using the gravity loading, in accordance with procedures described in the Plaxis – Reference Manual.

Spring 2018

The spring 2018 scenario was identified as the most representative case, within the available time series, for simulating the transient evolution of measured groundwater levels and landslide displacements. A significant reactivation of the landslide occurred during this period, resulting in the interruption of the SP23R road (Cignetti et al., 2019). This scenario is the most typical situation observed in spring, when progressive soil saturation is principally due to snow melting at the end of the winter season, combined with rainfall.

During the spring 2018, piezometer P6SSTC4 recorded an increase in the groundwater level of approximately 5 m (from -13.07 m on 04/03/2018 to -8.71 m on 10/05/2018), due both to the abundant snowfall of the previous winter and to heavy rainfall in May 2018 (Arpa Piemonte, 2024d).

For computational efficiency, the numerical analysis focused on a shorter time window (Figure 6.6), which was nonetheless meaningful for the interpretation of the phenomenon. Based on the trend shown in Figure 6.6, three main phases were identified and subsequently used in the numerical simulations, as summarised in Table 6.3:

- Phase 1, in which a moderate groundwater table rise of approximately 1 m was observed over 15 days. A time-dependent groundwater head was applied as a boundary condition to reproduced this behaviour.
- Phase 2, characterised by a significant groundwater rise of about 3 m in 7 days (17/04/2018 to 24/04/2018) due to intense snowmelt and infiltration process. To ensure convergence in the numerical simulation, this phase was divided into 7 sub-phases. For each sub-phase, a constant infiltration rate of 0.05 m/day and a constant groundwater head were set to reach the target groundwater level at the end of the 7-day period.
- Phase 3, where an average increase of 1 m occurred, which was assumed to be constant over the time interval in the model. A time-dependent infiltration rate

was applied to account for significant rainfall contributions of about 0.01 m/day recorded between 03/05 and 13/05.

During these three phases, a cumulative displacement of approximately 4 mm was observed at the inclinometer. This value was used as a target for calibrating the numerical model.

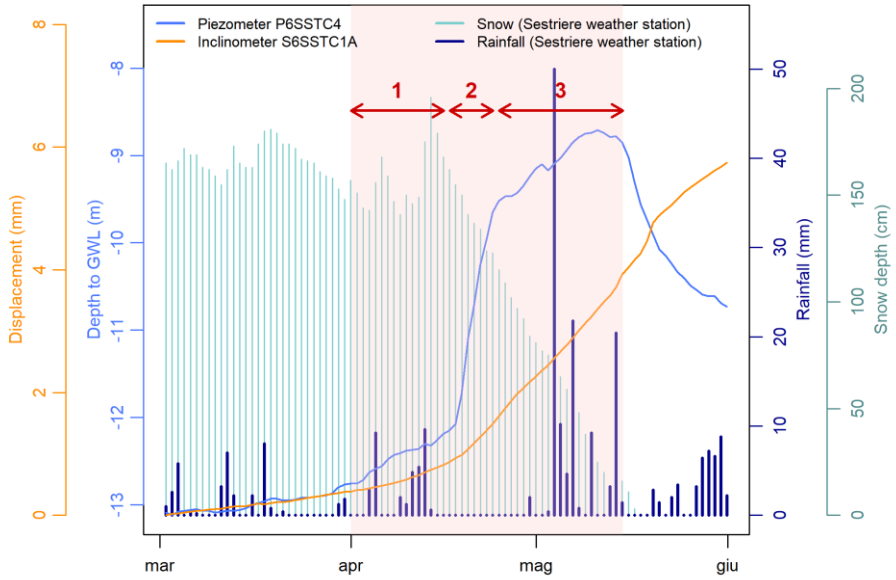

Figure 6.6 Calculation phases for the spring 2018.

Table 6.3 Staged construction for the spring 2018 in PLAXIS.

Phase	Time interval	Scenario	Rising GWL	Boundary condition
1	15 days	-	1 m	Time-dependent groundwater head
2	7 days	Snowmelt (0.05 m/day)	3 m	Constant infiltration rate and constant groundwater head for each sub-phase
3	20 days	Rainfall (0.01 m/day)	1 m	Time-dependent infiltration rate and constant global level

The simulation of this scenario was crucial for calibrating the model input parameters, in particular the hydraulic properties. It was used as a back-analysis of the event: through a trial-and-error procedure, the hydraulic properties were adjusted to minimise the difference between simulated and observed measurements. By discretising the investigated time window into several sub-phases, it was possible to iteratively refine the hydraulic conductivity and porosity values until the most appropriate ones were obtained (Table 6.2), ensuring a realistic representation of the groundwater flow over time.

Spring 2024

Noteworthy is the scenario of spring 2024, when prolonged and heavy rainfall affected the Piedmont Region (Arpa Piemonte, 2024f). At the beginning of March, the Sestriere station had already recorded 75% of the average monthly rainfall. Winter 2024 was marked by heavy snowfall at the end of the season and interested by the warmest temperatures recorded in the last 67 years (Arpa Piemonte, 2024b).

Given these conditions, the numerical analysis focused on a 42-day time window, similar to that used for 2018, enabling a direct comparison of the two scenarios, both characterised by prolonged rainfall and intense snowmelt. Analogously to spring 2018, three phases were identified as shown in Table 6.4. Here, the impact of the rainy period at the end of March (phase 1) was assessed, followed by the snowmelt process (phase 2). Finally, the contribution of heavy rainfall was simulated (phase 3).

As it can be seen in the Figure 6.7, the groundwater level increased by only 1 m (from -13.8 m on 01/03/2024 to -12.72 m on 16/05/2024), but the most significant increase occurred from 22/03/2024 (-13.75 m) to 29/03/2024 (-13.10 m), as defined in the phase 2, due to an increase in average temperature from -3.5 °C on 11/03/2024 to 8°C on 22/03/2024.

Compared to the spring 2018 case study, the initial displacement rate was higher (0.07 mm/day versus 0.01 mm/day) and doubled during Phase 2 as a consequence of snowmelt, reaching 0.14 mm/day. This occurred despite only a moderate increase in the recorded piezometric level.

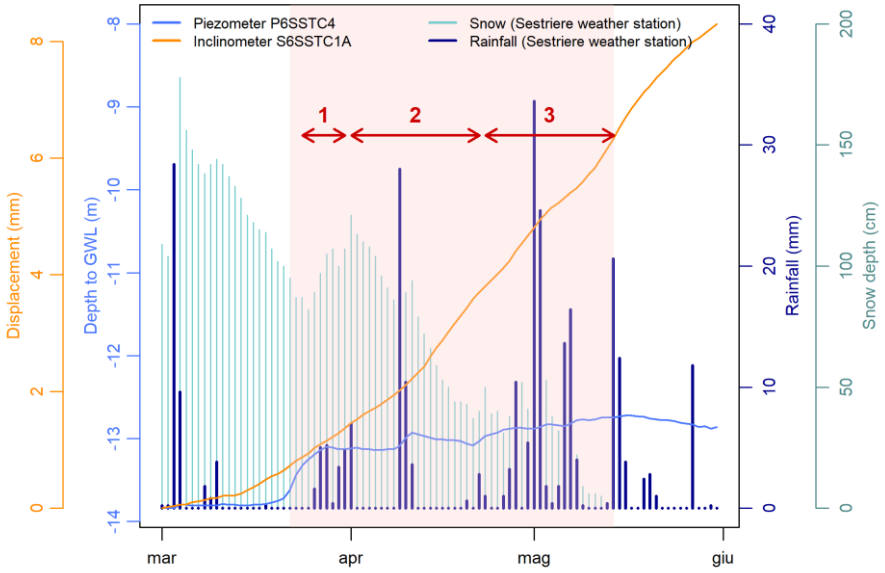

Figure 6.7 Calculation phases for the spring 2024.

Table 6.4 Staged construction for the spring 2024 in PLAXIS.

Phase	Time interval	Scenario	Rising GWL	Boundary condition
1	6 days	Rainfall (0.05 m/day)	-	Constant infiltration rate and constant groundwater head
2	21 days	Snowmelt (0.02 m/day)	1 m	Constant infiltration rate and time-dependent groundwater head
3	15 days	Rainfall (0.02 m/day)	-	Constant infiltration rate and constant groundwater head

November 2016

The event of 24th November 2016 was the third heaviest rainfall day in Piedmont since 1958 (Arpa Piemonte, 2024g).

Compared to the previous case study, here only two phases were considered in the numerical modelling (Figure 6.8 and Table 6.5):

- Phase 1 refers to the initial stage, corresponding to the day before the rainfall event.
- Phase 2, characterised by a pronounced groundwater rise of about 3 m over two days (24/11-25/11) was divided into 2 sub-phases. For the first and the second sub-phases, constant rainfall intensities of 0.2 m/day and 0.05 m/day, respectively, were applied. In the same way, groundwater head increases of 2 m and of 1 m were imposed. A discretization approach of the time window was adopted by the authors because, when both infiltration and groundwater head are time-dependent, numerical simulations can encounter convergence issues.

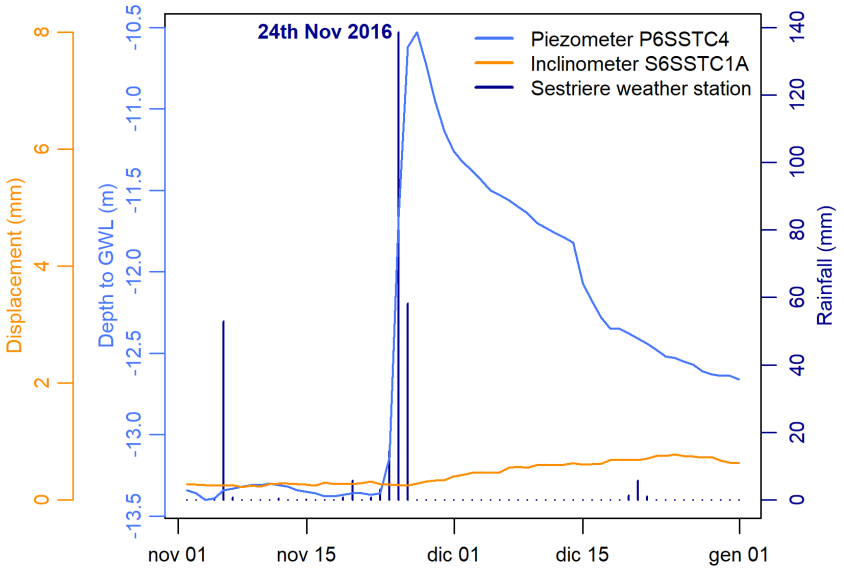

Figure 6.8 Calculation phases for the November 2016 event.

Table 6.5 Staged construction for the November 2016 event in PLAXIS.

Phase	Time interval	Scenario	Rising GWL	Boundary condition
1	1 day	-	-	Constant groundwater head
2	2 days	Heavy rainfall (0.2 m on 24/11 and 0.05 m on 25/11)	3 m	Constant infiltration rate and groundwater head for each sub-phase

6.4 Results and Discussion

Due to the large number of outputs, the analysis focused on the area near Champlas du Col, where both the inclinometer and piezometer are located (see Figure 3.1a). This choice was made for two reasons:

- estimating the groundwater depth across the entire model domain was challenging, given the availability of only one monitoring point. A more realistic scenario could therefore be obtained by directly comparing the precise groundwater level and displacement values measured by the instruments with those derived from the simulation.
- the area holds strategic importance due to the presence of the SP23R road, making it essential to assess the hydrogeological dynamics responsible for the continuous ground deformation at this location (Barla, 2018).

For this aim, the variation of the investigated parameters was analysed through calculation steps at specific control points in the model. Figure 6.9 shows the control points in the mesh, from which more detailed curves of pore water pressure and relative hydraulic conductivity were extracted at the end of each simulation. Since the analysis focuses on unsaturated soil behaviour, variations in these parameters were examined above the groundwater table. Points in the saturated zone were neglected, as a predictable increase in negative pressure values is expected there.

For all three scenarios, the results related to changes in pore water pressure, degree of saturation, relative hydraulic conductivity and displacements are presented. In particular, the spring 2018 and 2024 scenarios are compared, as the investigation covers the same time window.

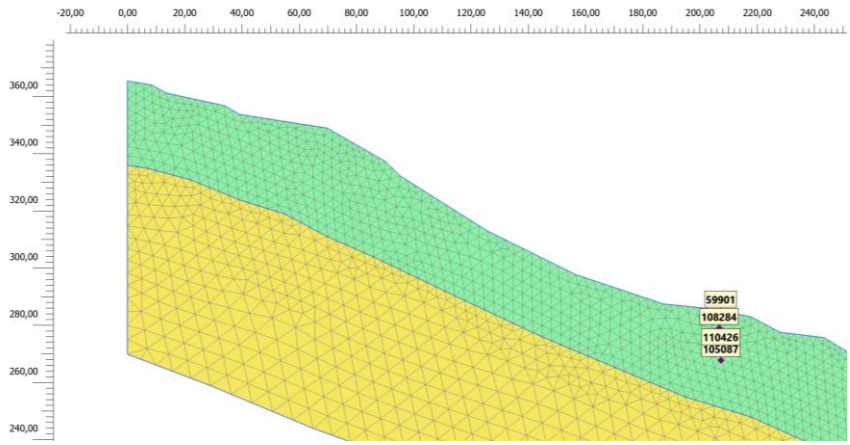

Figure 6.9 Control points at the same location of the SP23R road and the S6SSTC1A inclinometer.

6.4.1 Snowmelt and prolonged rainfall: spring 2018 and 2024

Due to rainfall infiltration into the slope, a significant increase in the degree of saturation was observed in both cases. Initially, the slope was partially saturated, with a degree of around 20%. As rainwater infiltrated, this saturation progressively increased, reaching values close to 70% in the unsaturated zone (Figure 6.10). In spring 2024, when more intense and sustained rainfall was recorded, the saturation front advanced deeper into the slope rather than remaining confined to the surface (Figure 6.11). This led to higher pore water pressures, reduced suction and a significant alteration of the slope's hydro-mechanical conditions.

Figure 6.12a illustrates the evolution of pore water pressure in the unsaturated zone over time at stress points 59901 and 108284. A comparison between the two years reveals that the pressure drop in 2024 was much more rapid and pronounced, with values peaking early and remaining persistently high throughout the observation period. This behaviour contrasts with 2018, when the rise in pore water pressure was more gradual, with a lower and delayed peak. The 2024 scenario indicates a more severe hydraulic response, with rapid saturation and sustained high pressures potentially leading to a substantial decrease in matric suction and, consequently, reduced slope shear strength.

The graph in Figure 6.12b further supports this interpretation by showing the relative hydraulic conductivity, K_{rel}, versus time at the control points. This analysis was crucial for observing the increase in saturation over time and for understanding the slope's behaviour under different infiltration levels (Yang et al., 2021). Initially, water is strongly retained in the soil by capillary forces. When it rains and water infiltrates, K_{rel} starts to rise as the wetting front advances. If inflows exceed outflow, matric suction decreases, consequently reducing soil strength. Infiltrated water can also cause seepage forces that might destabilise the slope. Conversely, when rainfall ceases, suction may increase again, thereby improving slope stability (Natalia & Yang, 2025).

In 2024, relative hydraulic conductivity rose more quickly and at an earlier stage, particularly in the upper slope zones, indicating a rapid and deep wetting front. By contrast, in 2018, the increase was more gradual, suggesting slower infiltration dynamics. Saturation propagation from shallow to deeper zones was clear in both scenarios, but it was far more pronounced in 2024.

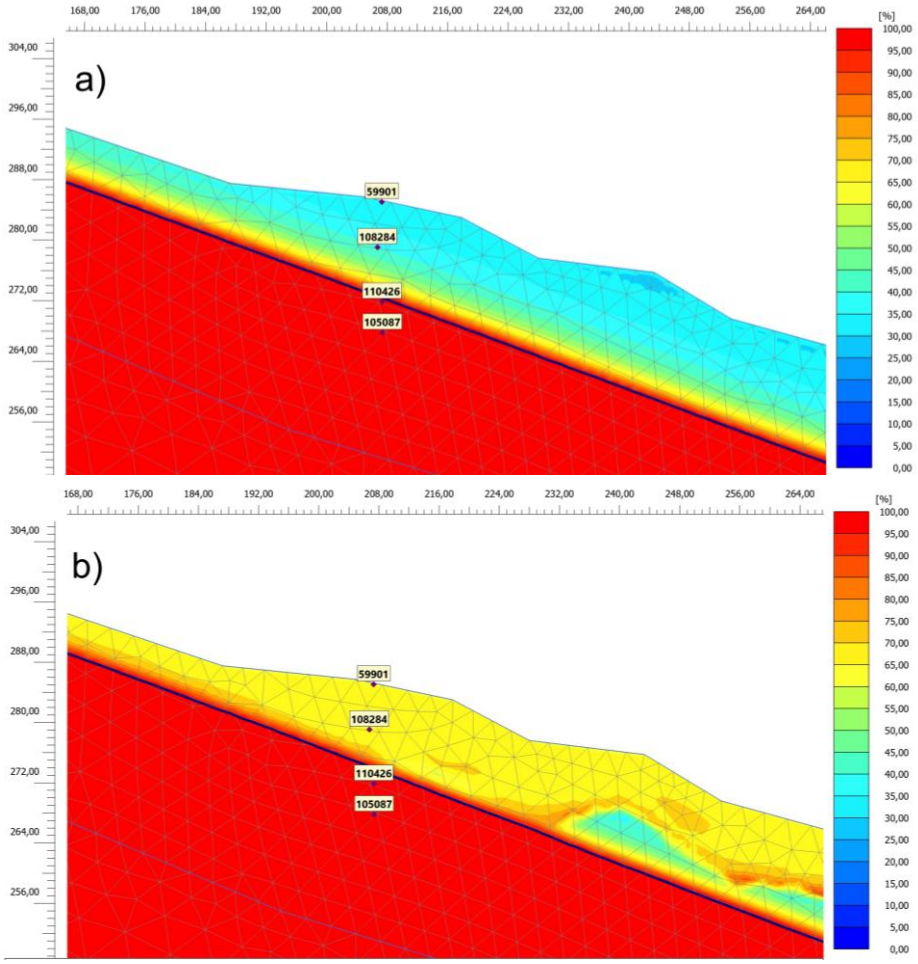

Figure 6.10 Saturation degree in spring 2018: (a) initial stage - day 1 and (b) at the end of simulation - day 43.

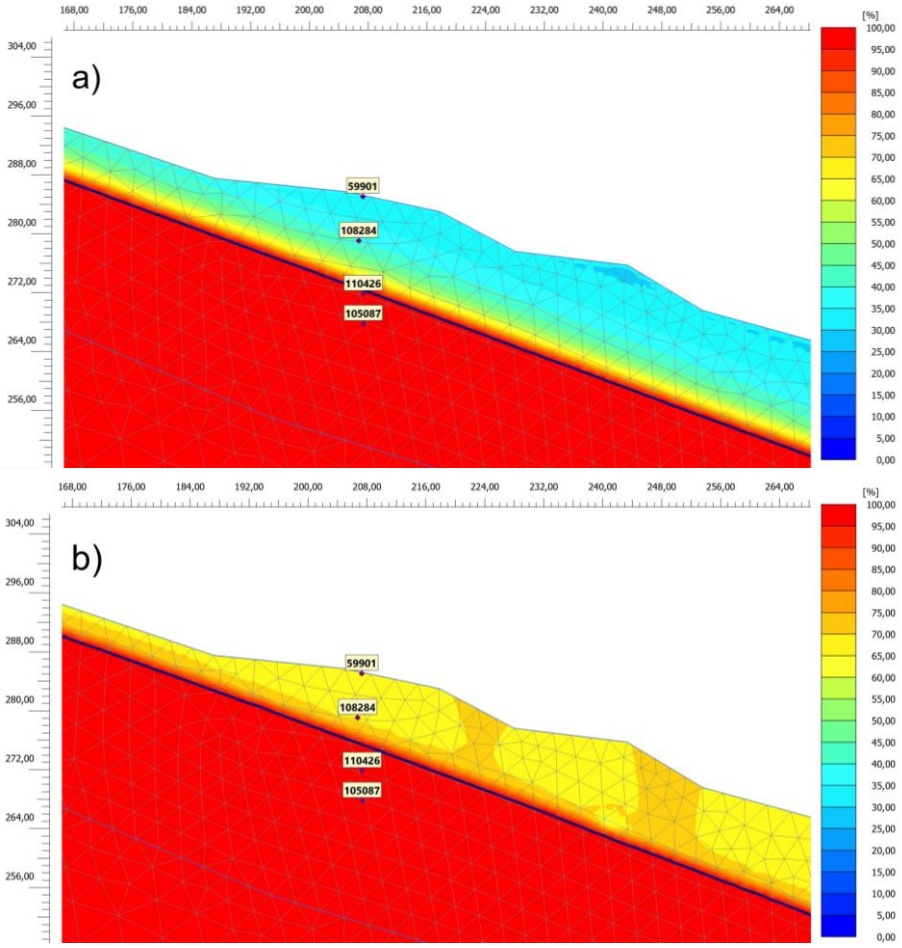

Figure 6.11 Saturation degree in spring 2024: (a) initial stage - day 1 and (b) at the end of simulation - day 43 (right).

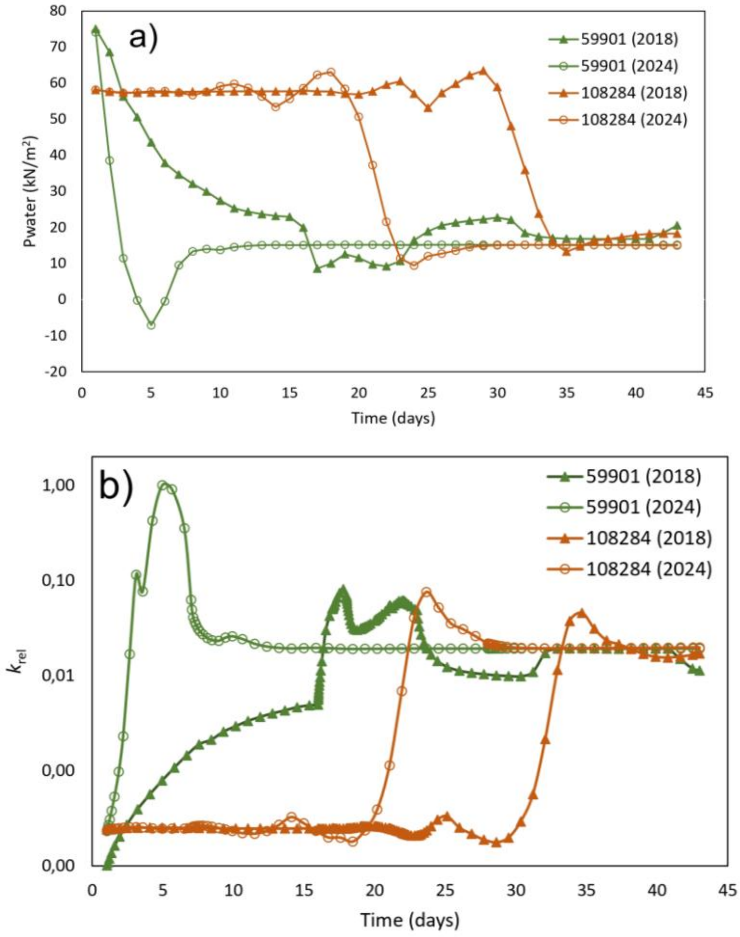

Figure 6.12 Comparison of trends in (a) pore water pressure (p_{water}) and (b) relative permeability (k_{rel}) in the unsaturated zone for spring 2018 and 2024.

The hydrodynamic response has important implications for slope stability, potentially reducing soil shear strength and influencing deformation rates (Chatra et al., 2019). However, the 2018 event produced more limited and temporally distributed infiltration, probably leading to less critical conditions. Overall, comparing the two years highlights how variations in rainfall intensity and duration can strongly influence the hydromechanical dynamics of an active landslide, increasing its susceptibility to reactivation.

A comparison between inclinometric displacement observations and corresponding finite element model outputs (Figure 6.13) shows good agreement in terms of both the temporal evolution and magnitude of movements at the monitored location (node 16357 in the mesh, where the fixed-probe inclinometer is installed at 18 m depth). As shown in Figure 6.14, displacement curves for both years show consistent trends between measured and modelled data. In 2018, inclinometer readings showed slightly higher cumulative displacements than those predicted for the same node.

Movement rate analyses from inclinometer data show that in both cases, and especially in 2024, the average daily displacement (0.01 mm/day) was greatly exceeded (see Table 6.6).

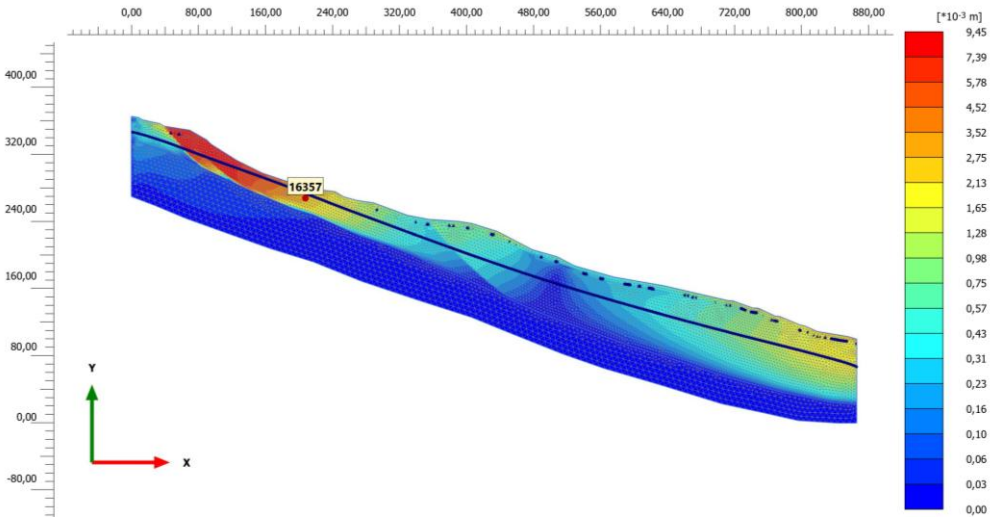

Figure 6.13 Total displacement pattern in spring 2024. The node 16357 at the inclinometer location is depicted.

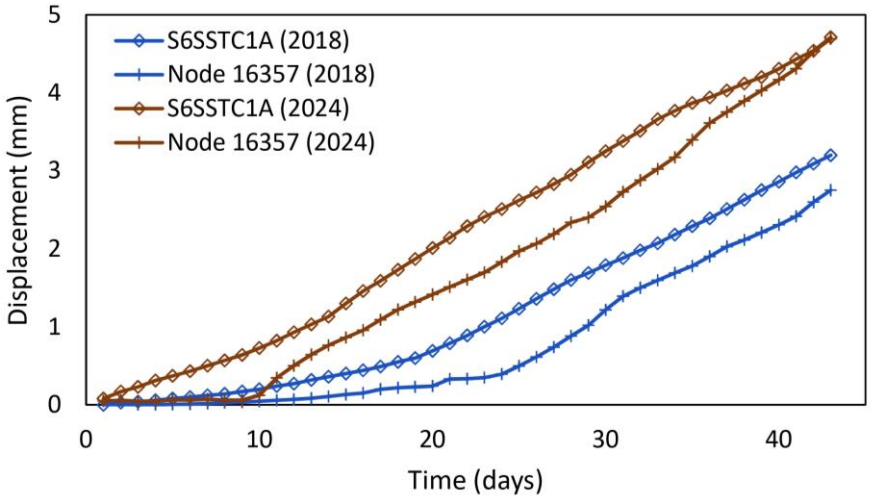

Figure 6.14 Cumulative displacements in spring 2018 and 2024: inclinometric measurements and model output.

Table 6.6 Observed and predicted landslide displacements (1 April -13 May).

	Displacement (mm)		Rate (mm/day)
	Model (node 16357)	Inclinometer S6SSTC1A	
2018	2.75	3.21	0.06
2024	4.69	4.71	0.11

The worst-case scenario in spring 2024 can be directly attributed to increased soil saturation caused by heavy rainfall in early spring. These hydromechanical changes triggered faster and more continuous ground movements during the

monitoring period. The numerical model successfully reproduced this acceleration, confirming its sensitivity to hydraulic forcing.

The strong consistency between measured and simulated displacement trends validates the reliability of the numerical outputs and the model's capacity to accurately capture the slope's hydrogeological and mechanical behaviour. Overall, these findings emphasise the importance of integrating monitoring data with numerical modelling to accurately interpret slope responses and assess stability under different boundary conditions.

6.4.2 Heavy rainfall event: November 2016

The dynamics observed during the heavy rainfall event differed markedly from those in the previous two cases. The results suggest that slope saturation occurred only moderately during this short-term precipitation event (see Figure 6.15). As can be seen from the pore water pressure at point 108284 (Figure 6.16a) the suction remained persistently high in the subsoil throughout the simulation. However, a noticeable decrease in suction was observed at a few depths, accompanied by a corresponding increase in relative permeability. Indeed, Figure 6.16b shows that permeability varied minimally over time at depth, further confirming that subsurface conditions remained essentially unchanged. Due to the limited duration of the rainfall, surface infiltration was insufficient to advance the wetting front significantly, thus preventing moisture from reaching the subsoil. This pattern of shallow infiltration preserved negative pore pressures in the lower parts of the slope, contributing to a more stable hydromechanical regime throughout the simulation, as proven by the negligible displacement rate increase (Table 6.7).

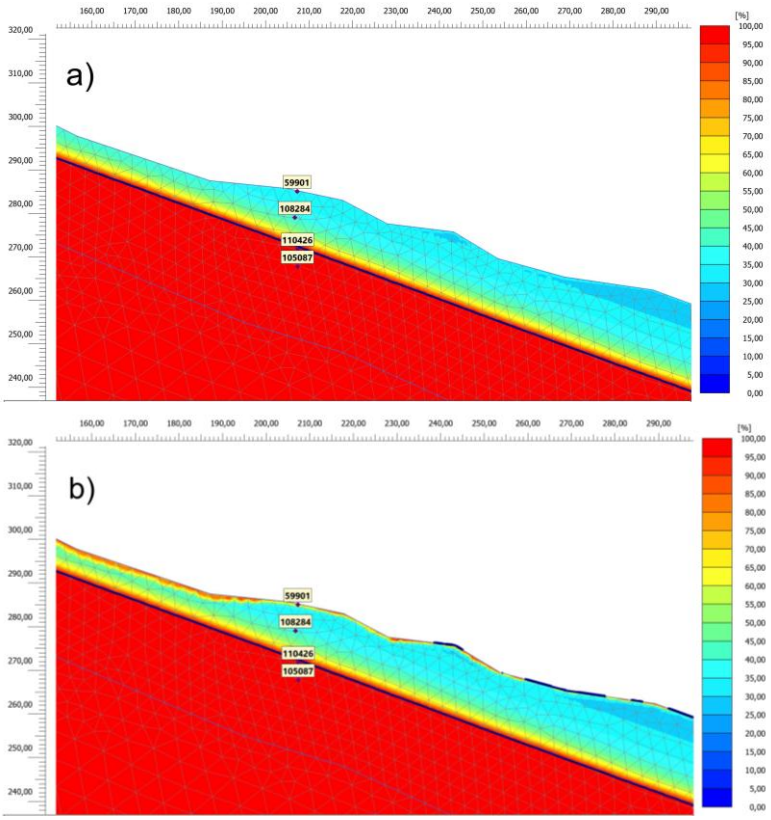

Figure 6.15 Saturation degree in November 2016: (a) initial stage - day 1 (left) and (b) at the end of simulation - day 3 (right).

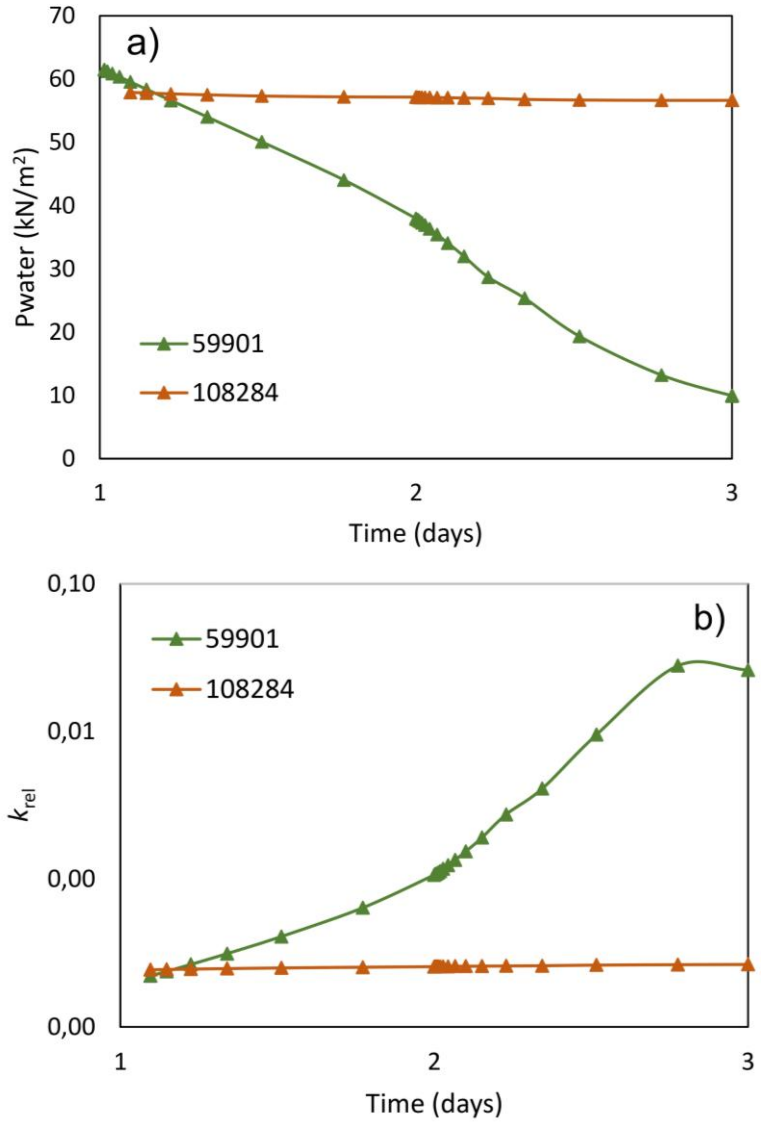

Figure 6.16 Trends in (a) pore water pressure (p_{water}) and (b) relative permeability (k_{rel}) in the unsaturated zone for the November 2016 event

Table 6.7 Observed and predicted landslide displacements in the November 2016 event.

Displacements (mm)	
Model (node 16357)	**Inclinometer S6SSTC1A**
0.42	0.16

6.5 Conclusions

Given the model findings, some considerations can be drawn that apply to all three cases. The simulations proved that the infiltration of rainfall and snowmelt induces complex hydromechanical dynamics within the slope. In fact, during this process a wetting front propagates vertically downwards through the unsaturated zones, inducing changes in the pore pressure regime. It was observed that, as the soil above the groundwater level gradually gets saturated, positive pore pressures decrease due to the loss of suction, while the rise of groundwater level leads to the development of negative pressures at deeper levels.

The analysis also highlighted that prolonged periods of rainfall and snowmelt have a greater impact on soil saturation than a single rainfall event. Continuous and sustained infiltrative input reduces the slope stability, leading to a significant increase in the displacements pattern of the landslide body.

In the 2024 case, the higher degree of saturation compared to 2018 was a consequence of abundant rainfall in March, followed by the snowmelt period. This scenario was singular because the warm winter temperatures caused early snowmelt, leading to soil saturation in early spring. Under these conditions, the rise in water table was limited because the infiltrating water from prolonged rainfall did not percolate downwards as quickly as it would have in unsaturated soil.

On the contrary, the 2016 case showed that a single heavy rainfall event caused a marked rise in the water table, resulting in significant changes in the pore water pressure regime. However, this did not substantially affect slope stability.

In conclusion, the results proved that slope stability is directly influenced by variations in pore water pressure, which is a function of rainfall intensity, infiltration rate, the hydraulic properties of saturated and unsaturated soil and slope geometry. Studying the hydrogeological processes that influence landslide acceleration requires appropriate geomechanical and geotechnical input data. However, since many of these parameters were not available, assumptions and simplifications were necessary to set up the model.

It is possible to state that a good agreement was achieved between the model outputs and field-based prediction, such as the available inclinometer data used to locally validate the displacements. Nevertheless, it is therefore necessary to refine the model in order to achieve more reliable results.

Chapter 7

Conclusions

Most of the achievements of this thesis stem from the adoption of suitable methodological approaches to investigate the hydrogeological processes underlying slow-kinematic slope instability. The work was carried out to provide an updated overview of the analytical techniques currently available, taking as examples a few representative landslide sites located in the Susa Valley (Piedmont region, North-Western Italy).

The state of the art of slow-moving landslides features and investigation approaches is presented in Chapter 1. The Western Italian Alps are widely affected by extensive gravitational phenomena due to their geomorphological characteristics and intense post-glacial erosion. In this setting, groundwater regime is the main driver of large deep-seated landslides. Although these ground instabilities react slowly to precipitation and move at imperceptible velocities, they can reshape landscape over time. Additionally, the evolving climatic conditions of the mountain environment contribute to slope instability, thereby accelerating movements.

As discussed in Chapter 2, the magnitude and frequency of landslides are increasingly likely to change in relation to a constanly changing climate. Mountains are "sentinels of changes" and respond more promptly and effectively than other geographical environments (Gariano & Guzzetti, 2016). In this framework, attention is paid to slow-moving landslides as they provide an interesting learning examples for the dynamics governing their behaviour. The merging between in situ and remote monitoring techniques enhance the interpretation of slope instabilities, but it requires a preliminary data processing due to the different spatial and temporal acquisition procedures before comparison can be made. In this regard, analytical models based on spatial interpolation could be implemented to overcome issues associated with comparing GPS and InSAR data as well as the installation of GPS benchmark with automated acquisition and non-annual readings could ensure a more reliable interpretation of deformation evolution. Statistical approaches could certainly provide valuable insights into the relationship between climatic factors and the triggering of slope failures and displacement mechanisms.

In Chapter 3, the analysis conducted on Champlas du Col and Thures landslides was addressed to this perspective, seeking to clarify the dynamics that govern the interaction between climate and landslide displacement. The main findings obtained through the undertaken statistical methods demonstrate that the groundwater fluctuations can be considered an indicator of landslide behaviour, emphasising the role of water springs. Specifically, annual displacement and

groundwater level trends, both of which are regulated by snowmelt processes, exhibit close temporal and proportional correlations. Accelerations in displacement occur shortly after rises in the water level, with the same intensity. The impact of prolonged and heavy rainfall on groundwater behaviour and, consequently, on increased displacement has also been identified. These findings raise a key question: to what extent can the innovative approach be reliably applied to other slow-moving landslides in comparable hydrogeological and climatic contexts? A promising outcome would be the development of a semi-automated tool to support consistent and repeatable assessments of landslide sites in mountainous and hilly environments by integrating groundwater and deformation data from a suitable monitoring network. Therefore, understanding groundwater circulation patterns within DSGSD contexts is essential for developing predictive models.

The results of the hydrochemical analyses discussed in Chapter 4 reinforce the interpretation of deep-water circulation inferred from the analysis of spring levels. Monitoring water temperature and mineralisation over time has revealed similar values for the springs located on the Champlas du Col and Thures slopes, suggesting the existence of interconnected water pathways within the landslide body. However, to improve the reliability of the aquifer dynamics assessment and to correctly detect the groundwater flow circuit, isotopic analyses and tracer tests could be performed. Furthermore, springs could be equipped with instruments to enable continuous monitoring of hydrogeological parameters.

Chapter 5 deals with time series decomposition and predictive analyses, providing further insight into the effect of hydrogeological forces on displacement. Overall, groundwater level is one the most informative descriptors of displacement variability, capturing a substantial fraction of the signal even without additional predictors. At the Thures site, the spring essentially fully represents this explanatory role, which further supports its value as a proxy for hydro-mechanical controls on displacement. In slow-moving landslides, the deformation response is usually delayed. Acceleration phases do not occur simultaneously with extreme weather conditions or rising groundwater levels, but rather after a delay period dependent on infiltration, progressive soil saturation, and pore pressure redistribution. In order to account for this non-instantaneous behaviour, the predictive model treats the delay parameter as a calibration variable. In this context, optimising the delay parameter effectively calibrates the model to meet the analysis requirements and simulate realistic processes. However, the delay that maximises cross-correlation may differ from the delay that minimises prediction errors, which suggests time-varying or multiphase hydrological responses. Finally, predictive performance is site-dependent, indicating that statistical results should be interpreted in light of local physical processes and boundary conditions.

Although the adopted regression framework provides useful preliminary information, it remains only indicative. Therefore, future developments should explore more advanced machine learning approaches to improve forecasting and capture nonlinearities, interactions and regime shifts more effectively, provided the datasets are sufficiently long, consistent and quality-controlled.

As described in Chapter 6, the numerical modelling of the Champlas du Col landslide integrates statistical and hydrochemical analyses, revealing that precipitation and water infiltration from snowmelt lead to complex, transient hydromechanical processes within the slope. The fully coupled hydromechanical model successfully reproduced the behaviour of a slow-moving landslide subject to creep deformation. Although the scarcity of input data compromised the accuracy of the results, modelling provided valuable insights into processes leading to slope instability in the event of persistent infiltration, thus improving the understanding of these phenomena from a mitigation perspective. However, the results could not be fully validated due to a lack of adequate instrumentation for monitoring soil water content and changes in pore pressure. A warning system could therefore be implemented to alert the relevant authorities in the event of anomalous precipitation, which could lead to rock mass oversaturation and increase slope instability.

Leveraging displacement and mountain spring monitoring, hydrochemical analyses, and complementary statistical–numerical tools, this dissertation proposed an integrated and flexible workflow to enhance the local-scale hydrogeological characterisation of slow-moving landslides. The findings showed that springs can effectively explain slope hydrogeological processes, enabling the interpretation of long-term deformation patterns even where monitoring networks are spatially limited. The cross-validation of independent datasets, combined with a representation of delayed responses, can support the extraction of comparable indicators with predictive value for risk-mitigation purposes. Future works could exploit DSGSD bodies as groundwater reservoirs, pointing to targeted drainage and water management measures as viable options to limit pore-pressure build-up and slow slope movements.

References

Agliardi, F., Crosta, G., & Zanchi, A. (2001). Structural constraints on deep-seated slope deformation kinematics. *Engineering Geology*, *59*(1–2), 83–102. https://doi.org/10.1016/S0013-7952(00)00066-1

Agliardi, F., Zanchi, A., & Crosta, G. B. (2009). Tectonic vs. gravitational morphostructures in the central Eastern Alps (Italy): Constraints on the recent evolution of the mountain range. *Tectonophysics*, *474*(1–2), 250–270. https://doi.org/10.1016/j.tecto.2009.02.019

Ahmed, A., & Hossain, S. (2022). Field Determination of Unsaturated Permeability and Flow Properties through Subgrade Instrumentation. *Geosciences*, *12*(2), 95. https://doi.org/10.3390/geosciences12020095

Ahmed, W., Ali, T., & Khattak, A. (2025). A Signal-Decomposed Ensemble Forecasting and Classification Framework for Household Power Consumption: An STL-Inspired Machine Learning Approach. *International Journal of Innovations in Science and Technology*, 1503–1517. https://doi.org/10.33411/ijist/20257315031517

Akaike, H. (1973). Information theory and an extension of the maximum likelihood principle. *B. N. Petrov & F. Csaki (Eds.),2nd International Symposium on Information Theory*, 267–281.

Alberto, W., Carraro, F., & Giardino, M. (2008). *Specificità e implicazioni applicative dell'evoluzione del fenomeno gravitativo di Cima Bosco (alta Valle di Susa, Alpi Occidentali)*.

Alfio, M. R., Pisinaras, V., Panagopoulos, A., & Balacco, G. (2024). Groundwater level response to precipitation at the hydrological observatory of Pinios (central Greece). *Groundwater for Sustainable Development*, *24*, 101081. https://doi.org/10.1016/j.gsd.2024.101081

Amanzio, G., Bertolo, D., De Maio, M., Lodi, L. P., Pitet, L., & Suozzi, E. (2015). Global Warming in the Alps: Vulnerability and Climatic Dependency of Alpine Springs in Italy, Regione Valle d'Aosta and Switzerland, Canton Valais. In G. Lollino, A. Manconi, F. Guzzetti, M. Culshaw, P. Bobrowsky, & F. Luino (A c. Di), *Engineering Geology for Society and Territory—Volume 5* (pp. 1375–1378). Springer International Publishing. https://doi.org/10.1007/978-3-319-09048-1_263

Amarasinghe, M. P., Robert, D., Kulathilaka, S. A. S., Zhou, A., & Jayathissa, H. A. G. (2024). Slope stability analysis of unsaturated colluvial slopes based on case studies of rainfall-induced landslides. *Bulletin of Engineering Geology and the Environment*, *83*(11), 476. https://doi.org/10.1007/s10064-024-03933-1

Anson, R., & Hawkins, A. (2002). Movement of the Soper's Wood landslide on the Jurassic Fuller's Earth, Bath, England. *Bulletin of Engineering Geology and the Environment*, *61*(4), 325–345. https://doi.org/10.1007/s10064-002-0151-8

Apuani, T., Masetti, M., & Rossi, M. (2007). Stress–strain–time numerical modelling of a deep-seated gravitational slope deformation: Preliminary results. *Quaternary International*, *171–172*, 80–89. https://doi.org/10.1016/j.quaint.2007.01.014

Ardizzone, F., Gariano, S. L., Volpe, E., Antronico, L., Coscarelli, R., Manunta, M., & Mondini, A. C. (2023). A Procedure for the Quantitative Comparison

of Rainfall and DInSAR-Based Surface Displacement Time Series in Slow-Moving Landslides: A Case Study in Southern Italy. *Remote Sensing*, *15*(2), 320. https://doi.org/10.3390/rs15020320

Arpa Piemonte. (2023a). *Scheda SIFraP II livello frana Sauze d'Oulx*. https://bdgm.arpa.piemonte.it/sifrap/sifrap_ii_liv_scheda.php?cod_frana=001-00756-01

Arpa Piemonte. (2023b). *Scheda SIFraP II livello frana Pragelato*. https://bdgm.arpa.piemonte.it/sifrap/sifrap_ii_liv_scheda.php?cod_frana=001-75366-00

Arpa Piemonte. (2023c). *Scheda SIFraP II livello frana Sestriere*. https://webgis.arpa.piemonte.it/geodissesto/sifrap/sifrap_ii_liv_scheda.php?cod_frana=001-76807- 00

Arpa Piemonte. (2023d). *Il clima in Piemonte—2022*. https://www.arpa.piemonte.it/pubblicazione/clima-piemonte-anno-2022

Arpa Piemonte. (2024a). *Scheda SIFraP II livello frana Cima del Bosco*. https://bdgm.arpa.piemonte.it/sifrap/sifrap_ii_liv_scheda.php?cod_frana=001-75537-00

Arpa Piemonte. (2024b). *Il clima in Piemonte—Inverno 2022*. https://www.arpa.piemonte.it/pubblicazione/clima-piemonte-inverno-2022#:~:text=In%20Piemonte%20l'inverno%202021,storica%20degli%20ultimi%2065%20anni

Arpa Piemonte. (2024c). *Il clima in Piemonte—Inverno 2024*. https://www.arpa.piemonte.it/pubblicazione/clima-piemonte-inverno-2024

Arpa Piemonte. (2024d). *Il clima in Piemonte—Primavera 2018*. https://www.arpa.piemonte.it/pubblicazione/clima-piemonte-primavera-2018

Arpa Piemonte. (2024e). Primavera 2024. https://www.arpa.piemonte.it/notizia/primavera-2024-battuto-record-storico-precipitazioni-degli-ultimi-70-anni

Arpa Piemonte. (2024f). *Il clima in Piemonte—Primavera 2024*. https://www.arpa.piemonte.it/pubblicazione/clima-piemonte-primavera-2024

Arpa Piemonte. (2024g). *Il clima in Piemonte – Novembre 2016*. https://www.arpa.piemonte.it/pubblicazione/clima-piemonte-novembre-2016

Arpa Piemonte. (2024h). *Il clima in Piemonte—Primavera 2022*. https:// www. arpa. piemo nte. it/ pubbl icazi one/ clima- piemo nte- prima vera- 2022

Athamena, A., Gaagai, A., Aouissi, H. A., Burlakovs, J., Bencedira, S., Zekker, I., & Krauklis, A. E. (2022). Chemometrics of the Environment: Hydrochemical Characterization of Groundwater in Lioua Plain (North Africa) Using Time Series and Multivariate Statistical Analysis. *Sustainability*, *15*(1), 20. https://doi.org/10.3390/su15010020

Audisio, C., Nigrelli, G., Pasculli, A., Sciarra, N., & Turconi, L. (2017). A gis spatial analysis model for landslide hazard mapping application in alpine area. *International Journal of Sustainable Development and Planning*, *12*(05), 883–893. https://doi.org/10.2495/SDP-V12-N5-883-893

Autorità di Bacino del fiume Po. (2023a). *Linee generali di assetto idrogeologico e quadro degli interventi (Bacino della Dora Riparia)*. https://www.adbpo.it/PAI/3%20- % 2 0Linee%20generali%20di%20assetto%20idraulico%20e%20idrogeologico /3.3%20- %20Elaborato%20Piemonte/Dora_Riparia.pdf

Balazs, G. H., & Chaloupka, M. (2004). Thirty-year recovery trend in the once depleted Hawaiian green sea turtle stock. *Biological Conservation*, *117*(5), 491–498. https://doi.org/10.1016/j.biocon.2003.08.008

Bao, S., Liu, J., Wang, L., & Zhao, X. (2022). Application of Transformer Models to Landslide Susceptibility Mapping. *Sensors*, *22*(23), 9104. https://doi.org/10.3390/s22239104

Barbato, G., Barini, E. M., Genta, G., & Levi, R. (2011). Features and performance of some outlier detection methods. *Journal of Applied Statistics*, *38*(10), 2133–2149. https://doi.org/10.1080/02664763.2010.545119

Barcelona, M. J., Holm, T. R., Schock, M. R., & George, G. K. (1989). Spatial and temporal gradients in aquifer oxidation-reduction conditions. *Water Resources Research*, *25*(5), 991–1003. https://doi.org/10.1029/WR025i005p00991

Barla, G. (2018). Numerical modeling of deep-seated landslides interacting with man-made structures. *Journal of Rock Mechanics and Geotechnical Engineering*, *10*(6), 1020–1036. https://doi.org/10.1016/j.jrmge.2018.08.006

Barla G., Forlati F., Scavia C. (1986). *Rivista italiana geotecnica*, 219–235.

Bernardie, S., Desramaut, N., Malet, J.-P., Gourlay, M., & Grandjean, G. (2015). Prediction of changes in landslide rates induced by rainfall. *Landslides*, *12*(3), 481–494. https://doi.org/10.1007/s10346-014-0495-8

Berti, M., Martina, M. L. V., Franceschini, S., Pignone, S., Simoni, A., & Pizziolo, M. (2012). Probabilistic rainfall thresholds for landslide occurrence using a Bayesian approach. *Journal of Geophysical Research: Earth Surface*, *117*(F4), 2012JF002367. https://doi.org/10.1029/2012JF002367

Bogaard, T., Guglielmi, Y., Marc, V., Emblanch, C., Bertrand, C., & Mudry, J. (2007). Hydrogeochemistry in landslide research: A review. *Bulletin de La Société Géologique de France*, *178*(2), 113–126. https://doi.org/10.2113/gssgfbull.178.2.113

Bonomo N. (2023). *Multidisciplinary study on the gravitational phenomena of Thures and Champlas du Col in the upper Susa Valley*. Politecnico di Torino.

Bordoni, M., Vivaldi, V., Bonì, R., Spanò, S., Tararbra, M., Lanteri, L., Parnigoni, M., Grossi, A., Figini, S., & Meisina, C. (2023). A methodology for the analysis of continuous time-series of automatic inclinometers for slow-moving landslides monitoring in Piemonte region, northern Italy. *Natural Hazards*, *115*(2), 1115–1142. https://doi.org/10.1007/s11069-022-05586-3

Borgogno Mondino, E., Giardino, M., & Perotti, L. (2009). A neural network method for analysis of hyperspectral imagery with application to the Cassas landslide (Susa Valley, NW-Italy). *Geomorphology*, *110*(1–2), 20–27. https://doi.org/10.1016/j.geomorph.2008.12.023

Box, G. E., Jenkins, G. M., & MacGregor, J. F. (1974). Some recent advances in forecasting and control. *Journal of the Royal Statistical Society: Series C (Applied Statistics)*, *23*(2), 158–179.

Box, G. E., Jenkins, G. M., Reinsel, G. C., & Ljung, G. M. (2015). *Time series analysis: Forecasting and control.*

Brighenti, S., Engel, M., Tolotti, M., Bruno, M. C., Wharton, G., Comiti, F., Tirler, W., Cerasino, L., & Bertoldi, W. (2021). Contrasting physical and chemical conditions of two rock glacier springs. *Hydrological Processes*, *35*(4), e14159. https://doi.org/10.1002/hyp.14159

Briški, M., Stroj, A., Kosović, I., & Borović, S. (2020). Characterization of Aquifers in Metamorphic Rocks by Combined Use of Electrical Resistivity Tomography and Monitoring of Spring Hydrodynamics. *Geosciences*, *10*(4), 137. https://doi.org/10.3390/geosciences10040137

Bustamante, J., Gallardo-Sepúlveda, R., Atencio, E., & Parra, P. F. (2025). Sensitivity Analysis of the Influence of Heavy-Intensity Rain Duration on the Stability of Granular Soil Slopes Under Unsaturated Conditions. *Applied Sciences*, *15*(11), 6074. https://doi.org/10.3390/app15116074

Calvin, K., Dasgupta, D., Krinner, G., Mukherji, A., Thorne, P. W., Trisos, C., Romero, J., Aldunce, P., Barrett, K., Blanco, G., Cheung, W. W. L., Connors, S., Denton, F., Diongue-Niang, A., Dodman, D., Garschagen, M., Geden, O., Hayward, B., Jones, C., … Ha, M. (con un contributo di Lee, H.). (2023). *IPCC, 2023: Climate Change 2023: Synthesis Report. Contribution of Working Groups I, II and III to the Sixth Assessment Report of the Intergovernmental Panel on Climate Change [Core Writing Team, H. Lee and J. Romero (eds.)]. IPCC, Geneva, Switzerland.* (P. Arias, M. Bustamante, I. Elgizouli, G. Flato, M. Howden, C. Méndez-Vallejo, J. J. Pereira, R. Pichs-Madruga, S. K. Rose, Y. Saheb, R. Sánchez Rodríguez, D. Ürge-Vorsatz, C. Xiao, N. Yassaa, J. Romero, J. Kim, E. F. Haites, Y. Jung, R. Stavins, … C. Péan, A c. Di; First). Intergovernmental Panel on Climate Change (IPCC). https://doi.org/10.59327/IPCC/AR6-9789291691647

Cantonati, M., Lichtenwöhrer, K., Leonhardt, G., Seifert, L., Mustoni, A., Hotzy, R., Schubert, E., Blattner, L., Bilous, O., Lotz, A., Poschlod, B., & Gerecke, R. (2022). Using Springs as Sentinels of Climate Change in Nature Parks North and South of the Alps: A Critical Evaluation of Methodological

Aspects and Recommendations for Long-Term Monitoring. *Water*, *14*(18), 2843. https://doi.org/10.3390/w14182843

Cappa, F., Guglielmi, Y., Viseur, S., & Garambois, S. (2014). Deep fluids can facilitate rupture of slow-moving giant landslides as a result of stress transfer and frictional weakening. *Geophysical Research Letters*, *41*(1), 61–66. https://doi.org/10.1002/2013GL058566

Carlà, T., Tofani, V., Lombardi, L., Raspini, F., Bianchini, S., Bertolo, D., Thuegaz, P., & Casagli, N. (2019). Combination of GNSS, satellite InSAR, and GBInSAR remote sensing monitoring to improve the understanding of a large landslide in high alpine environment. *Geomorphology*, *335*, 62–75. https://doi.org/10.1016/j.geomorph.2019.03.014

Carslaw D.C. (2005). On the changing seasonal cycles and trends of ozone at Mace Head, Ireland. *Atmos Chem Phys*, *5*, 3441–3450.

Cascini, L., Cuomo, S., Pastor, M., & Sorbino, G. (2010). Modeling of Rainfall-Induced Shallow Landslides of the Flow-Type. *Journal of Geotechnical and Geoenvironmental Engineering*, *136*(1), 85–98. https://doi.org/10.1061/(ASCE)GT.1943-5606.0000182

Cerino Abdin, E., Taddia, G., Gizzi, M., & Lo Russo, S. (2021). Reliability of spring recession curve analysis as a function of the temporal resolution of the monitoring dataset. *Environmental Earth Sciences*, *80*(7), 249. https://doi.org/10.1007/s12665-021-09529-2

Cervi, F., Ronchetti, F., Martinelli, G., Bogaard, T. A., & Corsini, A. (2012). Origin and assessment of deep groundwater inflow in the Ca' Lita landslide using hydrochemistry and in situ monitoring. *Hydrology and Earth System Sciences*, *16*(11), 4205–4221. https://doi.org/10.5194/hess-16-4205-2012

Chalikakis, K., Plagnes, V., Guerin, R., Valois, R., & Bosch, F. P. (2011). Contribution of geophysical methods to karst-system exploration: An overview. *Hydrogeology Journal*, *19*(6), 1169–1180. https://doi.org/10.1007/s10040-011-0746-x

Chaloupka, M. (2001). Historical trends, seasonality and spatial synchrony in green sea turtle egg production. *Biological Conservation*, *101*(3), 263–279. https://doi.org/10.1016/S0006-3207(00)00199-3

Chatra, A. S., Dodagoudar, G. R., & Maji, V. B. (2019). Numerical modelling of rainfall effects on the stability of soil slopes. *International Journal of Geotechnical Engineering*, *13*(5), 425–437. https://doi.org/10.1080/19386362.2017.1359912

Cheng, Z., Liu, S., Fan, X., Shi, A., & Yin, K. (2023). Deformation behavior and triggering mechanism of the Tuandigou landslide around the reservoir area of Baihetan hydropower station. *Landslides*, *20*(8), 1679–1689. https://doi.org/10.1007/s10346-023-02093-9

Chiaudani, A., Di Curzio, D., & Rusi, S. (2019). The snow and rainfall impact on the Verde spring behavior: A statistical approach on hydrodynamic and hydrochemical daily time-series. *Science of The Total Environment*, *689*, 481–493. https://doi.org/10.1016/j.scitotenv.2019.06.433

Cigna, F., Del Ventisette, C., Liguori, V., & Casagli, N. (2011). Advanced radar-interpretation of InSAR time series for mapping and characterization of geological processes. *Natural Hazards and Earth System Sciences*, *11*(3), 865–881. https://doi.org/10.5194/nhess-11-865-2011

Cignetti, M., Godone, D., Notti, D., Lanteri, L., & Giordan, D. (2024). Impacts on mountain settlements of a large slow rock-slope deformation: A multi-

temporal and multi-source investigation. *Landslides*, *21*(2), 327–337. https://doi.org/10.1007/s10346-023-02163-y

Cignetti, M., Godone, D., Wrzesniak, A., & Giordan, D. (2019). Structure from Motion Multisource Application for Landslide Characterization and Monitoring: The Champlas du Col Case Study, Sestriere, North-Western Italy. *Sensors*, *19*(10), 2364. https://doi.org/10.3390/s19102364

Cignetti, M., Godone, D., Zucca, F., Bertolo, D., & Giordan, D. (2020). Impact of Deep-seated Gravitational Slope Deformation on urban areas and large infrastructures in the Italian Western Alps. *Science of The Total Environment*, *740*, 140360. https://doi.org/10.1016/j.scitotenv.2020.140360

Cleveland, R.B., Cleveland, W.S., McRae, J.E., Terpenning, I. (1990). STL: a seasonal-trend decomposition procedure based on loess. *J. Off. Stat*, *6*, 3–73.

Cloke, H. L., Pappenberger, F., & Renaud, J. -P. (2008). Multi-method global sensitivity analysis (MMGSA) for modelling floodplain *hydrological processes*. *Hydrological Processes*, *22*(11), 1660–1674. https://doi.org/10.1002/hyp.6734

Colombero, C., Baillet, L., Comina, C., Jongmans, D., Larose, E., Valentin, J., & Vinciguerra, S. (2018). Integration of ambient seismic noise monitoring, displacement and meteorological measurements to infer the temperature-controlled long-term evolution of a complex prone-to-fall cliff. *Geophysical Journal International*, *213*(3), 1876–1897. https://doi.org/10.1093/gji/ggy090

Colyer, A., Butler, A., Peach, D., & Hughes, A. (2022). How groundwater time series and aquifer property data explain heterogeneity in the Permo-Triassic

sandstone aquifers of the Eden Valley, Cumbria, UK. *Hydrogeology Journal*, *30*(2), 445–462. https://doi.org/10.1007/s10040-021-02437-6

Comina, C., De Luca, D. A., Dolce, S., Forno, M. G., Gattiglio, M., Gianotti, F., Lasagna, M., Pigozzi, G., Roux, S., & Vergnano, A. (2025). Using Electrical Resistivity Tomography to Reconstruct Alpine Spring Supply: A Case Study from the Montellina Spring (Quincinetto, NW Alps, Italy). *GeoHazards*, *6*(3), 51. https://doi.org/10.3390/geohazards6030051

Conte, E., & Troncone, A. (2011). Analytical Method for Predicting the Mobility of Slow-Moving Landslides owing to Groundwater Fluctuations. *Journal of Geotechnical and Geoenvironmental Engineering*, *137*(8), 777–784. https://doi.org/10.1061/(ASCE)GT.1943-5606.0000486

Conte, E., Troncone, A., & Donato, A. (2016). A Simple Approach for Evaluating Slope Movements Induced by Groundwater Variations. *Procedia Engineering*, *158*, 200–205. https://doi.org/10.1016/j.proeng.2016.08.429

Corominas, J., Moya, J., Ledesma, A., Lloret, A., & Gili, J. A. (2005). Prediction of ground displacements and velocities from groundwater level changes at the Vallcebre landslide (Eastern Pyrenees, Spain). *Landslides*, *2*(2), 83–96. https://doi.org/10.1007/s10346-005-0049-1

Crosta, G. B., Frattini, P., & Agliardi, F. (2013). Deep seated gravitational slope deformations in the European Alps. *Tectonophysics*, *605*, 13–33. https://doi.org/10.1016/j.tecto.2013.04.028

Cruden, D. (1996). Cruden,D.M.,Varnes, D.J.,1996, Landslide Types and Processes, Transportation Research Board, U.S. National Academy of Sciences, Special Report, 247: 36-75. *Special Report - National Research Council, Transportation Research Board*, *247*, 36–57.

De Luca, D. A., Cerino Abdin, E., Forno, M. G., Gattiglio, M., Gianotti, F., & Lasagna, M. (2019a). The Montellina Spring as an Example of Water Circulation in an Alpine DSGSD Context (NW Italy). *Water*, *11*(4), 700. https://doi.org/10.3390/w11040700

De Luca, D. A., Cerino Abdin, E., Forno, M. G., Gattiglio, M., Gianotti, F., & Lasagna, M. (2019b). The Montellina Spring as an Example of Water Circulation in an Alpine DSGSD Context (NW Italy). *Water*, *11*(4), 700. https://doi.org/10.3390/w11040700

Del Soldato, M., Confuorto, P., Bianchini, S., Sbarra, P., & Casagli, N. (2021). Review of Works Combining GNSS and InSAR in Europe. *Remote Sensing*, *13*(9), 1684. https://doi.org/10.3390/rs13091684

Deline, P., & Orombelli, G. (2005). Glacier fluctuations in the western Alps during the Neoglacial, as indicated by the Miage morainic amphitheatre (Mont Blanc massif, Italy). *Boreas*, *34*(4), 456–467. https://doi.org/10.1111/j.1502-3885.2005.tb01444.x

Desmarais, K., & Rojstaczer, S. (2002). Inferring source waters from measurements of carbonate spring response to storms. *Journal of Hydrology*, *260*(1–4), 118–134. https://doi.org/10.1016/S0022-1694(01)00607-2

Drew, D. (2011). Book review: Groundwater Hydrology of Springs: Engineering, Theory, Management, and Sustainability, edited by Neven Kresic and Zoran Stevanovic (Elsevier, 2010). *Hydrogeology Journal*, *19*(6), 1279–1280. https://doi.org/10.1007/s10040-011-0767-5

Duan, G., Su, Y., & Fu, J. (2023). Landslide Displacement Prediction Based on Multivariate LSTM Model. *International Journal of Environmental Research and Public Health*, *20*(2), 1167. https://doi.org/10.3390/ijerph20021167

Eberhardt, E., Stead, D., & Coggan, J. S. (2004). Numerical analysis of initiation and progressive failure in natural rock slopes—The 1991 Randa rockslide. *International Journal of Rock Mechanics and Mining Sciences*, *41*(1), 69–87. https://doi.org/10.1016/S1365-1609(03)00076-5

Esterby, S. R. (1993). Trend analysis methods for environmental data. *Environmetrics*, *4*(4), 459–481. https://doi.org/10.1002/env.3170040407

Feng, C., Li, L., & Sadeghpour, A. (2020). A comparison of residual diagnosis tools for diagnosing regression models for count data. *BMC Medical Research Methodology*, *20*(1), 175. https://doi.org/10.1186/s12874-020-01055-2

Filippini, M., Squarzoni, G., De Waele, J., Fiorucci, A., Vigna, B., Grillo, B., Riva, A., Rossetti, S., Zini, L., Casagrande, G., Stumpp, C., & Gargini, A. (2018). Differentiated spring behavior under changing hydrological conditions in an alpine karst aquifer. *Journal of Hydrology*, *556*, 572–584. https://doi.org/10.1016/j.jhydrol.2017.11.040

Fioraso, G. (2017). Impact of massive deep-seated rock slope failures on mountain valley morphology in the northern Cottian Alps (NW Italy). *Journal of Maps*, *13*(2), 575–587. https://doi.org/10.1080/17445647.2017.1342211

Fioraso, G., Baggio, P., Bonadeo, L., and Brunamonte, F. (2011). Post-glacial evolution of gravitational slope deformations in the upper Susa and Chisone valleys (Italian western Alps). *Italian Journal of Quaternary Sciences*, *24*, 104–106.

Fioraso, G., & Mosca, P. (2014). *Note Illustrative della Carta geologica d'Italia alla scala 1:50.000 F. 171 Cesana Torinese, Servizio Geologico d'Italia—ISPRA*. https://doi.org/10.15161/OAR.IT/143175

Fioraso, G., Tararbra, M., and Negro, N. (2010). La deformazione gravitativa profonda di Sauze d'Oulx (Alpi Occidentali): Analisi dei meccanismi

deformativi in relazione all'evoluzione tardo quaternaria dell'alta Valle di Susa. *Italian Journal of Quaternary Sciences*, *23*(1), 37–54.

Fioravanti, G., Lena, F., Fraschetti, P., Perconti, W., Piervitali, E. (2022). *I normali climatici 1991-2020 di temperatura e precipitazione in Italia.* (Rapporto ISPRA/Stato dell'Ambiente No. 99).

Fiorillo, F., & Doglioni, A. (2010). The relation between karst spring discharge and rainfall by cross-correlation analysis (Campania, southern Italy). *Hydrogeology Journal*, *18*(8), 1881–1895. https://doi.org/10.1007/s10040-010-0666-1

Flores, Y. G., Eid, M. H., Szűcs, P., Szőcs, T., Fancsik, T., Szanyi, J., Kovács, B., Markos, G., Újlaki, P., Tóth, P., McIntosh, R. W., & Püspöki, Z. (2023). Integration of Geological, Geochemical Modelling and Hydrodynamic Condition for Understanding the Geometry and Flow Pattern of the Aquifer System, Southern Nyírség–Hajdúság, Hungary. *Water*, *15*(16), 2888. https://doi.org/10.3390/w15162888

Fontan D. (2022). *Piano Regolatore Generale Comunale (Sestriere): Variante strutturale n.21 – Relazione Geologica (Progetto Definitivo)*.

Forno. (2012). MORPHOLOGICAL FEATURES OF RODORETTO VALLEY DEEP-SEATED GRAVITATIONAL SLOPE DEFORMATIONS. *American Journal of Environmental Sciences*, *8*(6), 648–660. https://doi.org/10.3844/ajessp.2012.648.660

Forno, M. G., Comina, C., Gattiglio, M., Gianotti, F., Lo Russo, . S., Raiteri, L., Sambuelli, L.,Taddia, G. (2016). Preservation of quaternary sediments in DSGSD environment: The mont fallère case study (aosta valley, NW Italy). *Alpine and Mediterranean Quaternary*, *29*(2), 181–191.

Forno, M. G., Lingua, A., Lo Russo, S., & Taddia, G. (2011). Improving digital tools for Quaternary field survey: A case study of the Rodoretto Valley (NW Italy). *Environmental Earth Sciences*, *64*(5), 1487–1495. https://doi.org/10.1007/s12665-011-0971-6

Frattini, P., Crosta, G. B., Rossini, M., & Allievi, J. (2018). Activity and kinematic behaviour of deep-seated landslides from PS-InSAR displacement rate measurements. *Landslides*, *15*(6), 1053–1070. https://doi.org/10.1007/s10346-017-0940-6

Frei, C., & Schär, C. (1998). A precipitation climatology of the Alps from high-resolution rain-gauge observations. *International Journal of Climatology*, *18*(8), 873–900. https://doi.org/10.1002/(SICI)1097-0088(19980630)18:8%253C873::AID-JOC255%253E3.0.CO;2-9

Galleani, L., Vigna, B., Banzato, C., & Russo, S. L. (2011). Validation of a Vulnerability Estimator for Spring Protection Areas: The VESPA index. *Journal of Hydrology*, *396*(3–4), 233–245. https://doi.org/10.1016/j.jhydrol.2010.11.012

Gariano, S. L., & Guzzetti, F. (2016). Landslides in a changing climate. *Earth-Science Reviews*, *162*, 227–252. https://doi.org/10.1016/j.earscirev.2016.08.011

Gariano, S. L., Rianna, G., Petrucci, O., & Guzzetti, F. (2017). Assessing future changes in the occurrence of rainfall-induced landslides at a regional scale. *Science of The Total Environment*, *596–597*, 417–426. https://doi.org/10.1016/j.scitotenv.2017.03.103

Giardino, M., Giordan, D., & Ambrogio, S. (2004). G.I.S. technologies for data collection, management and visualization of large slope instabilities: Two

applications in the Western Italian Alps. *Natural Hazards and Earth System Sciences*, *4*(2), 197–211. https://doi.org/10.5194/nhess-4-197-2004

Gizzi, M., Lo Russo, S., Forno, M. G., Cerino Abdin, E., & Taddia, G. (2020). Geological and Hydrogeological Characterization of Springs in a DSGSD Context (Rodoretto Valley – NW Italian Alps). In M. De Maio & A. K. Tiwari (A c. Di), *Applied Geology* (pp. 3–19). Springer International Publishing. https://doi.org/10.1007/978-3-030-43953-8_1

Gizzi, M., Mondani, M., Taddia, G., Suozzi, E., & Lo Russo, S. (2022). Aosta Valley Mountain Springs: A Preliminary Analysis for Understanding Variations in Water Resource Availability under Climate Change. *Water*, *14*(7), 1004. https://doi.org/10.3390/w14071004

Gizzi, M., Narcisi, R., Mondani, M., & Taddia, G. (2023). COMPREHENDING MOUNTAIN SPRINGS' HYDROGEOLOGICAL PERSPECTIVES UNDER CLIMATE CHANGE IN AOSTA VALLEY (NORTHWESTERN ITALY): NEW AUTOMATED TOOLS AND SIMPLIFIED APPROACHES. *Italian Journal of Engineering Geology and Environment*, *1*(2023_S), 73. https://doi.org/10.4408/IJEGE.2023-01.S-10

Golian, S., & Ruigar, H. (2015). Assessing the correlation between climate signals and monthly mean and extreme precipitation and discharge of Golestan Dam Watershed. *Earth Sciences Research Journal*, *19*(1), 65–72. https://doi.org/10.15446/esrj.v19n1.40996

Groundwater Hydrology of Springs. (2010). Elsevier. https://doi.org/10.1016/C2009-0-19145-6

Handwerger, A. L., Roering, J. J., & Schmidt, D. A. (2013). Controls on the seasonal deformation of slow-moving landslides. *Earth and Planetary*

Science Letters, *377–378*, 239–247. https://doi.org/10.1016/j.epsl.2013.06.047

Helland, I. S. (1987). On the Interpretation and Use of R 2 in Regression Analysis. *Biometrics*, *43*(1), 61. https://doi.org/10.2307/2531949

Helsel DR, Hirsch RM, Ryberg KR, Archfield SA, Gilroy EJ. (2020). *Statistical methods in water resources: Book 4, chap. A3*. https:// doi. org/ 10.3133/ tm4a3

Hilberg, S., & Riepler, F. (2016). Interaction of various flow systems in small alpine catchments: Conceptual model of the upper Gurk Valley aquifer, Carinthia, Austria. *Hydrogeology Journal*, *24*(5), 1231–1244. https://doi.org/10.1007/s10040-016-1396-9

Hodson, T. O. (2022). Root-mean-square error (RMSE) or mean absolute error (MAE): When to use them or not. *Geoscientific Model Development*, *15*(14), 5481–5487. https://doi.org/10.5194/gmd-15-5481-2022

Hong, Y.-M., & Wan, S. (2011). Forecasting groundwater level fluctuations for rainfall-induced landslide. *Natural Hazards*, *57*(2), 167–184. https://doi.org/10.1007/s11069-010-9603-9

Hoseinzade, Z., Mokhtari, M., Shirani, K., & Miresmaeili, N. S. (2022). Identification of areas at the risk of landslide via the short-time Fourier transform. *Earth Science Informatics*, *15*(4), 2405–2413. https://doi.org/10.1007/s12145-022-00816-5

Hrehova, S., Antosz, K., Husár, J., & Vagaska, A. (2025). From Simulation to Validation in Ensuring Quality and Reliability in Model-Based Predictive Analysis. *Applied Sciences*, *15*(6), 3107. https://doi.org/10.3390/app15063107

Hu, J., Li, Z. W., Ding, X. L., Zhu, J. J., Zhang, L., & Sun, Q. (2014). Resolving three-dimensional surface displacements from InSAR measurements: A review. *Earth-Science Reviews*, *133*, 1–17. https://doi.org/10.1016/j.earscirev.2014.02.005

Huang, A.-B., Lee, J.-T., Ho, Y.-T., Chiu, Y.-F., & Cheng, S.-Y. (2012). Stability monitoring of rainfall-induced deep landslides through pore pressure profile measurements. *Soils and Foundations*, *52*(4), 737–747. https://doi.org/10.1016/j.sandf.2012.07.013

Hugentobler, M., Loew, S., Aaron, J., Roques, C., & Oestreicher, N. (2020). Borehole monitoring of thermo-hydro-mechanical rock slope processes adjacent to an actively retreating glacier. *Geomorphology*, *362*, 107190. https://doi.org/10.1016/j.geomorph.2020.107190

Islam, Md. S., & Mostafa, M. G. (2022). Evaluation of Hydrogeochemical Processes in Groundwater Using Geochemical and Geostatistical Approaches in the Upper Bengal Basin. *Geofluids*, *2022*, 1–21. https://doi.org/10.1155/2022/9591717

Jin, A., Yang, S., & Huang, X. (2024). Landslide displacement prediction based on time series and long short-term memory networks. *Bulletin of Engineering Geology and the Environment*, *83*(7), 264. https://doi.org/10.1007/s10064-024-03714-w

Joelson, M., Golder, J., Beltrame, P., Néel, M.-C., & Di Pietro, L. (2016). On fractal nature of groundwater level fluctuations due to rainfall process. *Chaos, Solitons & Fractals*, *82*, 103–115. https://doi.org/10.1016/j.chaos.2015.11.010

Jomard, H., Lebourg, T., Guglielmi, Y., & Tric, E. (2010). Electrical imaging of sliding geometry and fluids associated with a deep seated landslide (La

Clapière, France). *Earth Surface Processes and Landforms*, *35*(5), 588–599. https://doi.org/10.1002/esp.1941

Kouassi, A. M., Ahoussi, K. E., Kouakou, K. E., Mamadou, A., & Biemi, J. (2016). Analyse comparative entre la distribution des fréquences de conductivité électrique et les faciès géochimiques des eaux des aquifères de socle (Côte d'Ivoire). *International Journal of Biological and Chemical Sciences*, *10*(1), 435. https://doi.org/10.4314/ijbcs.v10i1.33

Kresic, N., & Bonacci, O. (2010). Spring discharge hydrograph. In *Groundwater Hydrology of Springs* (pp. 129–163). Elsevier. https://doi.org/10.1016/B978-1-85617-502-9.00004-9

Lacroix, P., Handwerger, A. L., & Bièvre, G. (2020). Life and death of slow-moving landslides. *Nature Reviews Earth & Environment*, *1*(8), 404–419. https://doi.org/10.1038/s43017-020-0072-8

Lafare, A. E. A., Peach, D. W., & Hughes, A. G. (2016). Use of seasonal trend decomposition to understand groundwater behaviour in the Permo-Triassic Sandstone aquifer, Eden Valley, UK. *Hydrogeology Journal*, *24*(1), 141–158. https://doi.org/10.1007/s10040-015-1309-3

Laguardia, G. (2011). Representing the precipitation regime by means of Fourier series. *International Journal of Climatology*, *31*(9), 1398–1407. https://doi.org/10.1002/joc.2169

Lajaunie, M., Gance, J., Nevers, P., Malet, J.-P., Bertrand, C., Garin, T., & Ferhat, G. (2019). Structure of the Séchilienne unstable slope from large-scale three-dimensional electrical tomography using a Resistivity Distributed Automated System (R-DAS). *Geophysical Journal International*, *219*(1), 129–147. https://doi.org/10.1093/gji/ggz259

Lee, K., Suk, J., Kim, H., & Jeong, S. (2021). Modeling of rainfall-induced landslides using a full-scale flume test. *Landslides*, *18*(3), 1153–1162. https://doi.org/10.1007/s10346-020-01563-8

Legg, S. (2021). IPCC, 2021: Climate Change 2021—The Physical Science basis. *Interaction*, *49*(4), 44–45. (informit.315096509383738).

Leith, K., Moore, J. R., Amann, F., & Loew, S. (2014). Subglacial extensional fracture development and implications for Alpine Valley evolution. *Journal of Geophysical Research: Earth Surface*, *119*(1), 62–81. https://doi.org/10.1002/2012JF002691

Leone, G., Pagnozzi, M., Catani, V., Ventafridda, G., Esposito, L., & Fiorillo, F. (2021). A hundred years of Caposele spring discharge measurements: Trends and statistics for understanding water resource availability under climate change. *Stochastic Environmental Research and Risk Assessment*, *35*(2), 345–370. https://doi.org/10.1007/s00477-020-01908-8

Lindenmaier, F., Zehe, E., Dittfurth, A., & Ihringer, J. (2005). Process identification at a slow-moving landslide in the Vorarlberg Alps. *Hydrological Processes*, *19*(8), 1635–1651. https://doi.org/10.1002/hyp.5592

Liong, S. Y., Lim, W. H., Paudyal, G. N. (2000). River stage forecasting in Bangladesh: Neural network approach. *Journal of computing in civil engineering*, *14*(1), 1–8.

Liu, Y., Brezzi, L., Liang, Z., Gabrieli, F., Zhou, Z., & Cola, S. (2025). Image analysis and LSTM methods for forecasting surficial displacements of a landslide triggered by snowfall and rainfall. *Landslides*, *22*(3), 619–635. https://doi.org/10.1007/s10346-024-02328-3

Liu, Y., Qiu, H., Yang, D., Liu, Z., Ma, S., Pei, Y., Zhang, J., & Tang, B. (2022). Deformation responses of landslides to seasonal rainfall based on InSAR

and wavelet analysis. *Landslides*, *19*(1), 199–210. https://doi.org/10.1007/s10346-021-01785-4

Lo Russo, S., Suozzi, E., Gizzi, M., & Taddia, G. (2021). SOURCE: A semi-automatic tool for spring-monitoring data analysis and aquifer characterisation. *Environmental Earth Sciences*, *80*(21), 710. https://doi.org/10.1007/s12665-021-10027-8

Ma, R., An, Q., Liu, L., Cheng, Y., & Liu, X. (2025). Runoff Forecast Model Integrating Time Series Decomposition and Deep Learning for the Short Term: A Case Study in the Weihe River Basin, China. *Water*, *17*(18), 2718. https://doi.org/10.3390/w17182718

Ma, R., McBratney, A., Whelan, B., Minasny, B., & Short, M. (2011). Comparing temperature correction models for soil electrical conductivity measurement. *Precision Agriculture*, *12*(1), 55–66. https://doi.org/10.1007/s11119-009-9156-7

Marino, P., Santonastaso, G. F., Fan, X., & Greco, R. (2021). Prediction of shallow landslides in pyroclastic-covered slopes by coupled modeling of unsaturated and saturated groundwater flow. *Landslides*, *18*(1), 31–41. https://doi.org/10.1007/s10346-020-01484-6

Matsuura, S., Asano, S., & Okamoto, T. (2008). Relationship between rain and/or meltwater, pore-water pressure and displacement of a reactivated landslide. *Engineering Geology*, *101*(1–2), 49–59. https://doi.org/10.1016/j.enggeo.2008.03.007

Mburu, J. W., Li, A.-J., Lin, H.-D., & Lu, C.-W. (2022). Investigations of Unsaturated Slopes Subjected to Rainfall Infiltration Using Numerical Approaches—A Parametric Study and Comparative Review. *Sustainability*, *14*(21), 14465. https://doi.org/10.3390/su142114465

Mo, C., Ruan, Y., He, J., Jin, J., Liu, P., & Sun, G. (2019). Frequency analysis of precipitation extremes under climate change. *International Journal of Climatology*, *39*(3), 1373–1387. https://doi.org/10.1002/joc.5887

Mohsan, M., Vardon, P. J., & Vossepoel, F. C. (2021). On the use of different constitutive models in data assimilation for slope stability. *Computers and Geotechnics*, *138*, 104332. https://doi.org/10.1016/j.compgeo.2021.104332

Mondani, M., Gizzi, M., & Taddia, G. (2022). Role of Snowpack-Hydrometeorological Sensors for Hydrogeological System Comprehension inside an Alpine Closed-Basin. *Sensors*, *22*(19), 7130. https://doi.org/10.3390/s22197130

Montanari, A., & Toth, E. (2007). Calibration of hydrological models in the spectral domain: An opportunity for scarcely gauged basins? *Water Resources Research*, *43*(5), 2006WR005184. https://doi.org/10.1029/2006WR005184

Monte, N., Bucci, F., Mevoli, F. A., Santangelo, M., Reichenbach, P., Di Matteo, L., & Marchesini, I. (2024). A dataset of geotechnical parameters based on international literature to characterise lithotypes in Italy. *Scientific Data*, *11*(1), 1371. https://doi.org/10.1038/s41597-024-04095-1

Moreno, M., Lombardo, L., Crespi, A., Zellner, P. J., Mair, V., Pittore, M., Van Westen, C., & Steger, S. (2024). Space-time data-driven modeling of precipitation-induced shallow landslides in South Tyrol, Italy. *Science of The Total Environment*, *912*, 169166. https://doi.org/10.1016/j.scitotenv.2023.169166

Musbah, H., El-Hawary, M., & Aly, H. (2019). Identifying Seasonality in Time Series by Applying Fast Fourier Transform. *2019 IEEE Electrical Power and Energy Conference (EPEC)*, 1–4. https://doi.org/10.1109/EPEC47565.2019.9074776

Narcisi, R., Pappalardo, S. E., Taddia, G., & De Marchi, M. (2024). Assessing climate impacts on slow-moving landslides in the western Alps of Piemonte: Integration of monitoring techniques for detecting displacements. *Frontiers in Earth Science*, *12*, 1365469. https://doi.org/10.3389/feart.2024.1365469

Narcisi, R., Vagnon, F., Gizzi, M., & Taddia, G. (2026). Spring trends in slow-moving landslide displacement: Is it a reliable way to predict their movements? Two case studies in the Susa Valley (NW Italy). *Landslides*. https://doi.org/10.1007/s10346-026-02693-1

Natalia, L., & Yang, J. (2025). Impact of hysteresis of unsaturated hydraulic properties on rainfall-induced slope failures. *Engineering Geology*, *354*, 108175. https://doi.org/10.1016/j.enggeo.2025.108175

Ng, C. W. W., & Shi, Q. (1998). A numerical investigation of the stability of unsaturated soil slopes subjected to transient seepage. *Computers and Geotechnics*, *22*(1), 1–28. https://doi.org/10.1016/S0266-352X(97)00036-0

Nigrelli, G., & Chiarle, M. (2021). Evolution of temperature indices in the periglacial environment of the European Alps in the period 1990–2019. *Journal of Mountain Science*, *18*(11), 2842–2853. https://doi.org/10.1007/s11629-021-6889-x

Oppenheim, A. V., Schafer, R. W., & Buck, J. R. (1999). *Discrete-time signal processing / Alan V. Oppenheim, Ronald W. Schafer, with John R. Buck.* (Second edition.). Prentice Hall.

Ostertagová, E. (2012). Modelling using Polynomial Regression. *Procedia Engineering*, *48*, 500–506. https://doi.org/10.1016/j.proeng.2012.09.545

Panagopoulos, G., & Lambrakis, N. (2006). The contribution of time series analysis to the study of the hydrodynamic characteristics of the karst systems:

Application on two typical karst aquifers of Greece (Trifilia, Almyros Crete). *Journal of Hydrology*, *329*(3–4), 368–376. https://doi.org/10.1016/j.jhydrol.2006.02.023

Paranunzio, R., Chiarle, M., Laio, F., Nigrelli, G., Turconi, L., & Luino, F. (2019). New insights in the relation between climate and slope failures at high-elevation sites. *Theoretical and Applied Climatology*, *137*(3–4), 1765–1784. https://doi.org/10.1007/s00704-018-2673-4

Pecoraro, G., & Calvello, M. (2021). Integrating local pore water pressure monitoring in territorial early warning systems for weather-induced landslides. *Landslides*, *18*(4), 1191–1207. https://doi.org/10.1007/s10346-020-01599-w

Pecoraro, G., Calvello, M., & Piciullo, L. (2019). Monitoring strategies for local landslide early warning systems. *Landslides*, *16*(2), 213–231. https://doi.org/10.1007/s10346-018-1068-z

Pedretti, L., Bordoni, M., Vivaldi, V., Figini, S., Parnigoni, M., Grossi, A., Lanteri, L., Tararbra, M., Negro, N., & Meisina, C. (2023). InterpolatiON of InSAR Time series for the dEtection of ground deforMatiOn eVEnts (ONtheMOVE): Application to slow-moving landslides. *Landslides*, *20*(9), 1797–1813. https://doi.org/10.1007/s10346-023-02073-z

Peduto, D., Nicodemo, G., Luongo, D., Borrelli, L., Reale, D., Ferlisi, S., Fornaro, G., & Gullà, G. (2025). Multi-source data-based quantitative risk analysis of road networks to slow-moving landslides. *Engineering Geology*, *350*, 108011. https://doi.org/10.1016/j.enggeo.2025.108011

Pfeiffer, J., Zieher, T., Schmieder, J., Bogaard, T., Rutzinger, M., & Spötl, C. (2022). Spatial assessment of probable recharge areas – investigating the hydrogeological controls of an active deep-seated gravitational slope

deformation. *Natural Hazards and Earth System Sciences*, *22*(7), 2219–2237. https://doi.org/10.5194/nhess-22-2219-2022

Phakdimek, S., Komori, D., Chaithong, T., & Abe, Y. (2025). Physically based model for assessing rainfall-induced deep-seated landslides using a hydrological-geotechnical model. *Annals of GIS*, *31*(2), 301–331. https://doi.org/10.1080/19475683.2025.2481063

Piper, A. M. (1944). A graphic procedure in the geochemical interpretation of water-analyses. *Eos, Transactions American Geophysical Union*, *25*(6), 914–928.

Pirone, M., Di Maio, R., Forte, G., De Paola, C., Di Marino, E., Salone, R., Santo, A., & Urciuoli, G. (2023). Study of the groundwater regime in unsaturated slopes prone to landslides by multidisciplinary investigations: Experimental study and numerical modelling. *Engineering Geology*, *315*, 107045. https://doi.org/10.1016/j.enggeo.2023.107045

Pisani G. (2009). *Hydrogeological model and hydromechanical behaviour of the Rosone landslide* [PhD thesis]. Politecnico di Torino.

Preisig, G. (2020). Forecasting the long-term activity of deep-seated landslides via groundwater flow and slope stability modelling. *Landslides*, *17*(7), 1693–1702. https://doi.org/10.1007/s10346-020-01427-1

Priestley MB. (1981). Spectral analysis of non-stationary processes using the evolutionary spectrum. *Journal of the Royal Statistical Society*, *43*(1), 1–15.

Prokešová, R., Medveďová, A., Tábořík, P., & Snopková, Z. (2013). Towards hydrological triggering mechanisms of large deep-seated landslides. *Landslides*, *10*(3), 239–254. https://doi.org/10.1007/s10346-012-0330-z

Ramesh Kumar, A., & Riyazuddin, P. (2012). Seasonal variation of redox species and redox potentials in shallow groundwater: A comparison of measured

and calculated redox potentials. *Journal of Hydrology*, *444–445*, 187–198. https://doi.org/10.1016/j.jhydrol.2012.04.018

Rembert, F., Jougnot, D., & Guarracino, L. (2020). A fractal model for the electrical conductivity of water-saturated porous media during mineral precipitation-dissolution processes. *Advances in Water Resources*, *145*, 103742. https://doi.org/10.1016/j.advwatres.2020.103742

Ren, S., & Ghazali, K. H. (2025). Integrating Time Series Decomposition and Deep Learning: An STL-TCN-Transformer Framework for Landslide Displacement Prediction. *The 8th Mechanical Engineering, Science and Technology International Conference*, 60. https://doi.org/10.3390/engproc2025084060

Revelle, W. (2023). *psych: Procedures for Personality and Psychological Research [R package]* (Versione (Version 2023.06.1)) [Software]. https://CRAN.R-project.org/package=psych

Ronchetti, F., Piccinini, L., Deiana, M., Ciccarese, G., Vincenzi, V., Aguzzoli, A., Malavasi, G., Fabbri, P., & Corsini, A. (2020). Tracer test to assess flow and transport parameters of an earth slide: The Montecagno landslide case study (Italy). *Engineering Geology*, *275*, 105749. https://doi.org/10.1016/j.enggeo.2020.105749

Sapone M. (2023). *Evaluation of the effects of temperature increases on the flow rates of specific springs in the Piedmont region. Analysis of the changes in flow patterns observed in specific Piedmontese springs during recent years and their comparison with local meteorological data*. Politecnico di Torino.

Schanz T, Vermeer PA, Bonnier PG. (1999). *The Hardening Soil Model: Formulation and verification*.

Schoeller, H. (1962). *Les eaux souterraines masson et cie Paris*.

Schweiger, H. F., Fabris, C., Ausweger, G., & Hauser, L. (2019). Examples of successful numerical modelling of complex geotechnical problems. *Innovative Infrastructure Solutions*, *4*(1), 2. https://doi.org/10.1007/s41062-018-0189-5

Segoni, S., Lagomarsino, D., Fanti, R., Moretti, S., & Casagli, N. (2015). Integration of rainfall thresholds and susceptibility maps in the Emilia Romagna (Italy) regional-scale landslide warning system. *Landslides*, *12*(4), 773–785. https://doi.org/10.1007/s10346-014-0502-0

Servizio Geologico D'Italia. (2014). *Carta Geologica d'Italia alla scala 1:50.000, F. 171 Cesana Torinese* [Dataset]. INFN Open Access Repository. https://doi.org/10.15161/OAR.IT/143173

Shafieiganjeh, R., Schneider-Muntau, B., Ostermann, M., & Gems, B. (2024). Seepage process understanding at long-existing landslide dams through numerical analysis and hydrological measurements. *Engineering Geology*, *335*, 107524. https://doi.org/10.1016/j.enggeo.2024.107524

Shahbazi, S., Crosetto, M., & Barra, A. (2022). GROUND DEFORMATION ANALYSIS USING BASIC PRODUCTS OF THE COPERNICUS GROUND MOTION SERVICE. *The International Archives of the Photogrammetry, Remote Sensing and Spatial Information Sciences*, *XLIII-B3-2022*, 349–354. https://doi.org/10.5194/isprs-archives-XLIII-B3-2022-349-2022

Shamsudduha, M., Chandler, R. E., Taylor, R. G., & Ahmed, K. M. (2009). Recent trends in groundwater levels in a highly seasonal hydrological system: The Ganges-Brahmaputra-Meghna Delta. *Hydrology and Earth System Sciences*, *13*(12), 2373–2385. https://doi.org/10.5194/hess-13-2373-2009

Solari, L., Del Soldato, M., Montalti, R., Bianchini, S., Raspini, F., Thuegaz, P., Bertolo, D., Tofani, V., & Casagli, N. (2019). A Sentinel-1 based hot-spot analysis: Landslide mapping in north-western Italy. *International Journal of Remote Sensing*, *40*(20), 7898–7921. https://doi.org/10.1080/01431161.2019.1607612

Solari, L., Del Soldato, M., Raspini, F., Barra, A., Bianchini, S., Confuorto, P., Casagli, N., & Crosetto, M. (2020). Review of Satellite Interferometry for Landslide Detection in Italy. *Remote Sensing*, *12*(8), 1351. https://doi.org/10.3390/rs12081351

Song, K., Yan, E., Zhang, G., Lu, S., & Yi, Q. (2015). Effect of hydraulic properties of soil and fluctuation velocity of reservoir water on landslide stability. *Environmental Earth Sciences*, *74*(6), 5319–5329. https://doi.org/10.1007/s12665-015-4541-1

Stoffel, M., Tiranti, D., & Huggel, C. (2014). Climate change impacts on mass movements—Case studies from the European Alps. *Science of The Total Environment*, *493*, 1255–1266. https://doi.org/10.1016/j.scitotenv.2014.02.102

Tawalo, A., Falcone, G., Pirone, M., d'Onofrio, A., & Urciuoli, G. (2025). Numerical modelling of displacements induced by rainfall infiltration in a clayey soil slope: The Miscano (Southern Italy) case study. *Computers and Geotechnics*, *184*, 107267. https://doi.org/10.1016/j.compgeo.2025.107267

Terzaghi, K. (1962). Stability of Steep Slopes on Hard Unweathered Rock. *Géotechnique*, *12*(4), 251–270. https://doi.org/10.1680/geot.1962.12.4.251

Teshebaeva, K., Echtler, H., Bookhagen, B., & Strecker, M. (2019). Deep-seated gravitational slope deformation (DSGSD) and slow-moving landslides in the southern Tien Shan Mountains: New insights from InSAR, tectonic and

geomorphic analysis. *Earth Surface Processes and Landforms*, *44*(12), 2333–2348. https://doi.org/10.1002/esp.4648

Toločka, A. (2025). Towards understanding the global distribution of deep-seated gravitational deformations: A study of geological influences and spatial patterns. *Natural Hazards*, *121*(14), 16149–16183. https://doi.org/10.1007/s11069-025-07448-0

Tullen, P., Parriaux, A., & Tacher, L. (2002). Improvement of the hydrogeological modelling of landslides. *Engineering geology for developing countries*, 1406–1414.

Turkeltaub, T., Mannheim, R., Furman, A., & Weisbrod, N. (2023). Elucidating the relationship between gaseous O2 and redox potential in a soil aquifer treatment system using data driven approaches and an oxygen diffusion model. *Journal of Hydrology*, *618*, 129168. https://doi.org/10.1016/j.jhydrol.2023.129168

Vallet, A., Bertrand, C., Mudry, J., Bogaard, T., Fabbri, O., Baudement, C., & Régent, B. (2015). Contribution of time-related environmental tracing combined with tracer tests for characterization of a groundwater conceptual model: A case study at the Séchilienne landslide, western Alps (France). *Hydrogeology Journal*, *23*(8), 1761–1779. https://doi.org/10.1007/s10040-015-1298-2

Vallet, A., Charlier, J. B., Fabbri, O., Bertrand, C., Carry, N., & Mudry, J. (2016). Functioning and precipitation-displacement modelling of rainfall-induced deep-seated landslides subject to creep deformation. *Landslides*, *13*(4), 653–670. https://doi.org/10.1007/s10346-015-0592-3

Van Asch, Th. W. J., Malet, J.-P., & Bogaard, T. A. (2009). The effect of groundwater fluctuations on the velocity pattern of slow-moving landslides.

Natural Hazards and Earth System Sciences, *9*(3), 739–749. https://doi.org/10.5194/nhess-9-739-2009

Van Asch, Th. W. J., Van Beek, L. P. H., & Bogaard, T. A. (2007). Problems in predicting the mobility of slow-moving landslides. *Engineering Geology*, *91*(1), 46–55. https://doi.org/10.1016/j.enggeo.2006.12.012

Van Genuchten, M. Th. (1980). A Closed-form Equation for Predicting the Hydraulic Conductivity of Unsaturated Soils. *Soil Science Society of America Journal*, *44*(5), 892–898. https://doi.org/10.2136/sssaj1980.03615995004400050002x

Wagener, T., & Gupta, H. V. (2005). Model identification for hydrological forecasting under uncertainty. *Stochastic Environmental Research and Risk Assessment*, *19*(6), 378–387. https://doi.org/10.1007/s00477-005-0006-5

Wang, C., Dai, F., Liu, Y., Wang, Y., Li, H., & Qu, W. (2023). Shallow Groundwater Responses to Rainfall Based on Correlation and Spectral Analyses in the Heilonggang Region, China. *Water*, *15*(6), 1100. https://doi.org/10.3390/w15061100

Wang, L., Chen, Y., Huang, X., Zhang, L., Li, X., & Wang, S. (2023). Displacement prediction method of rainfall-induced landslide considering multiple influencing factors. *Natural Hazards*, *115*(2), 1051–1069. https://doi.org/10.1007/s11069-022-05620-4

Wei, J., Chen, T., Liu, G., & Yang, J. (2016). Higher-order Multivariable Polynomial Regression to Estimate Human Affective States. *Scientific Reports*, *6*(1), 23384. https://doi.org/10.1038/srep23384

Wei, Z., Lü, Q., Sun, H., & Shang, Y. (2019). Estimating the rainfall threshold of a deep-seated landslide by integrating models for predicting the groundwater

level and stability analysis of the slope. *Engineering Geology*, *253*, 14–26. https://doi.org/10.1016/j.enggeo.2019.02.026

Welch, G., Bishop, G. (1995). *An introduction to the Kalman filter.*

Wen, Q., Zhang, Z., Li, Y., & Sun, L. (2020). Fast RobustSTL: Efficient and Robust Seasonal-Trend Decomposition for Time Series with Complex Patterns. *Proceedings of the 26th ACM SIGKDD International Conference on Knowledge Discovery & Data Mining*, 2203–2213. https://doi.org/10.1145/3394486.3403271

WMO. (2017). *WMO Guidelines on the Calculation of Climate Normals. WMO-No. 1203* (p. 29). https://community.wmo.int/en/wmo-climatological-normals

Yang, K.-H., Nguyen, T. S., Rahardjo, H., & Lin, D.-G. (2021). Deformation characteristics of unstable shallow slopes triggered by rainfall infiltration. *Bulletin of Engineering Geology and the Environment*, *80*(1), 317–344. https://doi.org/10.1007/s10064-020-01942-4

Yokoyama, K., Imaizumi, F., & Egusa, T. (2022). A Review of Groundwater Observation Methods for Slow-Moving Landslide. *International Journal of Erosion Control Engineering*, *15*(2), 7–21. https://doi.org/10.13101/ijece.15.7

Zachos, J., Pagani, M., Sloan, L., Thomas, E., & Billups, K. (2001). Trends, Rhythms, and Aberrations in Global Climate 65 Ma to Present. *Science*, *292*(5517), 686–693. https://doi.org/10.1126/science.1059412

Zhang, G., Wang, P., & Geng, X. (2024). Application of time series decomposition and LSTM neural network model to runoff prediction. *Proceedings of the 2024 International Academic Conference on Edge Computing, Parallel and*

Distributed Computing, 226–233. https://doi.org/10.1145/3677404.3677444

Zhang, L. L., Zhang, J., Zhang, L. M., & Tang, W. H. (2011). Stability analysis of rainfall-induced slope failure: A review. *Proceedings of the Institution of Civil Engineers - Geotechnical Engineering*, *164*(5), 299–316. https://doi.org/10.1680/geng.2011.164.5.299

Zhang, Z., Wang, B., Li, Z., Ye, X., Sun, Z., & Dias, D. (2024). Physics-guided neural network-based framework for 3D modeling of slope stability. *Computers and Geotechnics*, *176*, 106801. https://doi.org/10.1016/j.compgeo.2024.106801

Zhou, Z., Yu, L., Zhang, L., Jia, B., Zhang, Y., Luo, S., & Yin, C. (2025). Enhanced reservoir outflow prediction using STL-Informer model: A decomposition–prediction–reconstruction framework. *Journal of Hydroinformatics*, *27*(10), 1618–1631. https://doi.org/10.2166/hydro.2025.088

Zieher, T., Gallotti, G., Rianna, G., Reder, A., & Pfeiffer, J. (2023). Exploring the effects of climate change on the water balance of a continuously moving deep-seated landslide. *Natural Hazards*, *115*(1), 357–387. https://doi.org/10.1007/s11069-022-05558-7

Zieher, T., Markart, G., Ottowitz, D., Römer, A., Rutzinger, M., Meißl, G., & Geitner, C. (2017). Water content dynamics at plot scale – comparison of time-lapse electrical resistivity tomography monitoring and pore pressure modelling. *Journal of Hydrology*, *544*, 195–209. https://doi.org/10.1016/j.jhydrol.2016.11.019

Appendix A

This appendix contains supplementary material in support of the processing of climate and auxiliary datasets, as described in Chapter 2. The workflow adopted for extracting and processing daily climate data for the Dora Riparia and Chisone river basins is detailed in Figure A.1, and the results of autumn and spring cumulative precipitation anomalies for the 1991–2020 reference period are shown in Figure A.2 and Figure A.3. The time series related to the Champlas du Col landslide case study are also represented, namely the snow cover height from the Sestriere weather station (Figure A.4) and the groundwater level fluctuations recorded by the P6SSTC4 piezometer (Figure A.5), which will be further considered and discussed in the following chapters.

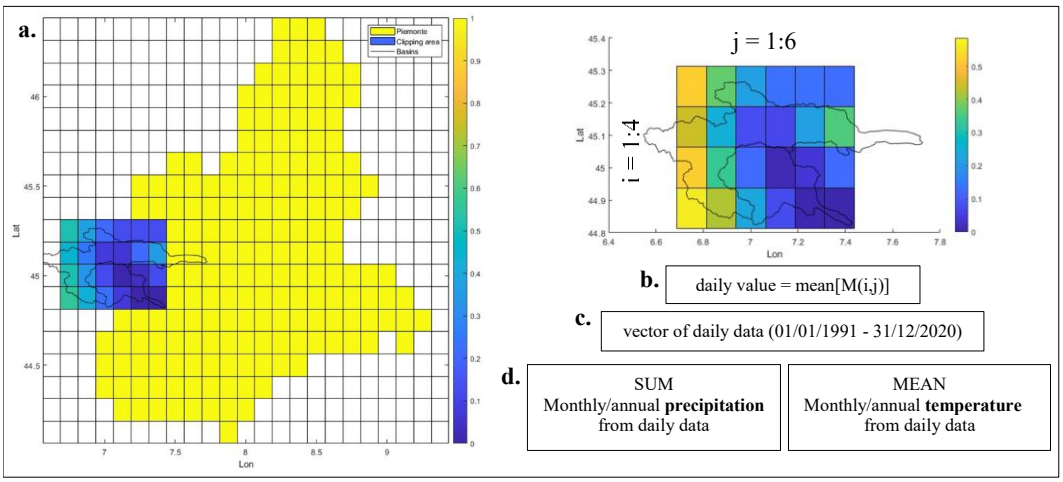

Figure A.1 Workflow of climatic data processed on MATLAB®. The following steps are shown: a. clipping of the area from the grid of daily climatic values of Piedmont (in the example, the precipitation data are shown) - b. daily value for the whole area from the spatial mean - c. vector of daily data - d. calculation of monthly/annual values.

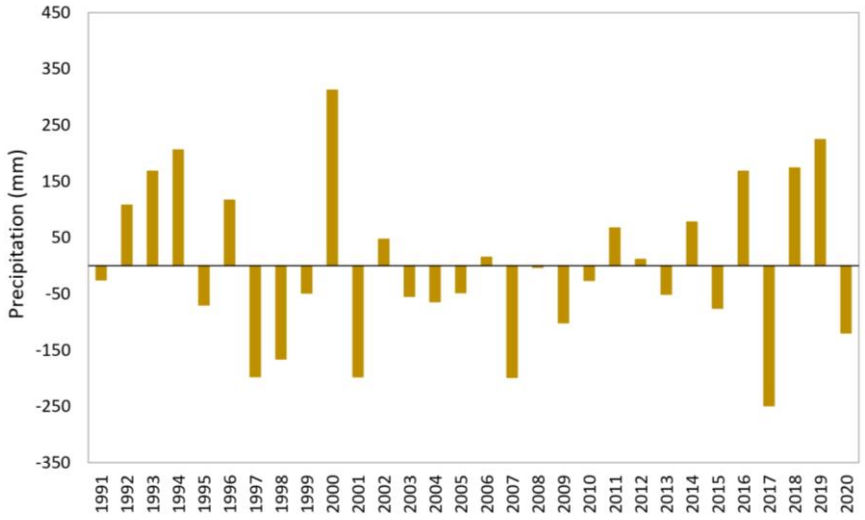

Figure A.2 Autumnal cumulative precipitation anomalies for the Dora Riparia and Chisone basins over the reference period 1991-2020. The resulting reference value is 328.24 mm.

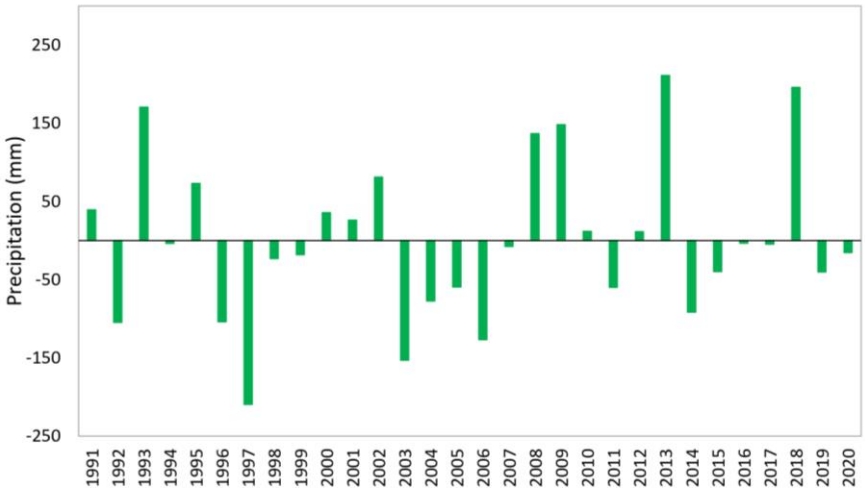

Figure A.3 Spring cumulative precipitation anomalies for the Dora Riparia and Chisone basins over the reference period 1991-2020. The resulting reference value is 299.24 mm.

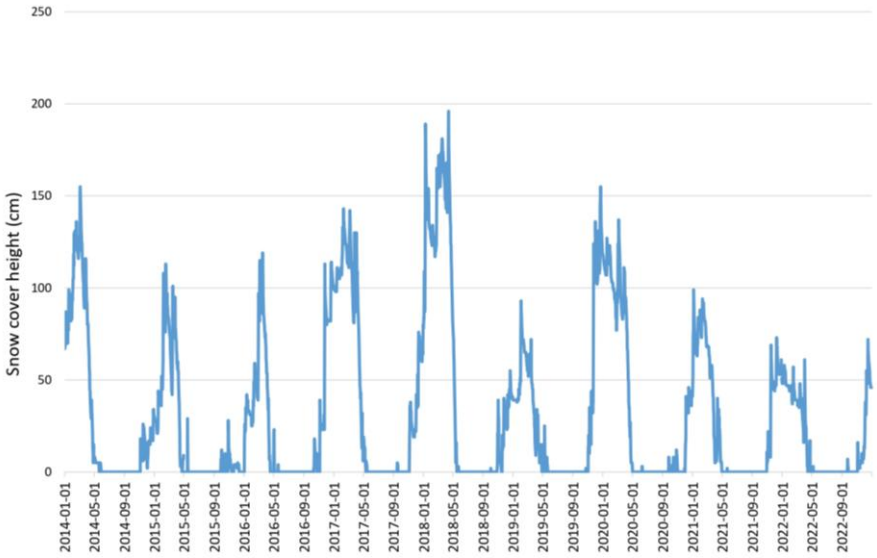

Figure A.4 Daily ground snow time series at Sestriere weather station (2020 m a.s.l.).

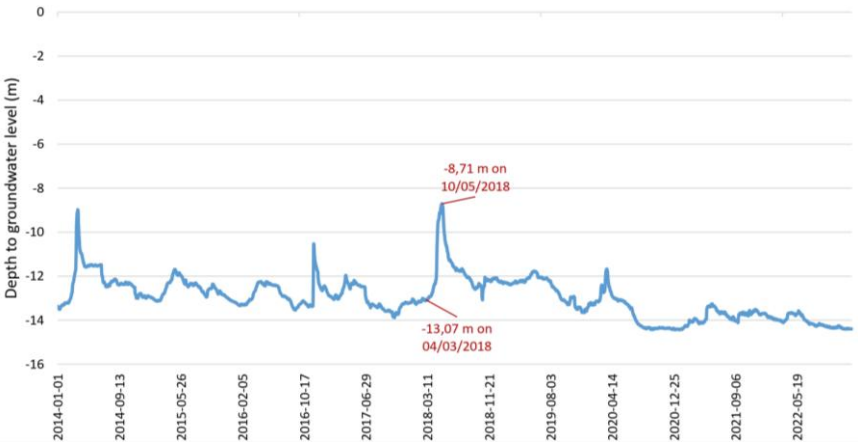

Figure A.5 Daily depth to groundwater level trend by piezometer P6SSTC4. Rising values in spring 2018 are marked.

Appendix B

Table B.1 and Table B.2 show the results of the hydrochemical analyses conducted during sampling campaigns at the Champlas du Col and Thures landslide sites (Chapter 4) since the beginning of monitoring activity. Specifically, the tables report the concentrations of the main ions measured on each water sample collected at the springs. Values of the field survey carried out on 21 November 2025 are not yet available. Schoeller diagrams of the springs illustrate the relative ionic composition of the sampled waters.

Table B.1 Results of the hydrochemical analyses performed on spring water samples (Boiler = BO; CFAV; Cordeminas=COR; TD=Tunnel Drenante) at the Champlas du Col site. Sampling campaigns are referred to the dates reported in Table 4.1

Sampling campaign	Ca^{2+}	Mg^{2+}	Na^{+}	K^{+}	Cl^{-}	SO_4^{2-}	HCO_3^{-}
BO-07	38,03	27,11	2,01	0,51	1,58	43,41	199,43
BO-08	51,73	38,03	2,70	0,84	1,27	46,17	295,41
BO-09	31,03	37,75	2,68	0,84	1,43	41,18	236,77
BO-10	43,20	43,31	2,27	0,71	2,91	37,86	296,93
BO-11	59,99	44,11	2,66	0,79	3,39	35,11	359,74
BO-12	58,92	41,16	3,21	1,95	1,25	32,03	354,50
BO-13	66,03	49,21	2,35	0,89	2,61	49,42	381,96
BO-14	57,04	42,97	2,66	0,83	1,95	42,86	340,47
BO-15	65,23	45,68	2,97	0,32	1,87	55,63	339,25
CFAV-08	50,43	28,77	2,94	0,52	0,49	31,26	265,62
CFAV-09	33,94	30,18	3,72	0,48	0,24	28,86	228,26
CFAV-10	50,74	39,11	3,99	0,47	1,69	29,38	321,80
CFAV-11	50,24	40,32	4,19	0,49	1,67	29,67	325,15
CFAV-12	61,44	36,24	4,50	0,94	0,54	23,83	349,62
CFAV-13	65,26	35,56	1,67	0,34	2,21	24,79	342,30
CFAV-14	63,27	36,19	2,94	0,44	1,18	30,95	341,69
CFAV-15	65,35	34,11	2,86	0,34	1,51	34,59	307,52
COR-07	29,33	24,24	1,14	0,19	1,21	21,73	183,94
COR-08	37,95	30,79	1,47	0,41	0,85	21,35	245,17
COR-09	29,21	32,41	1,42	0,45	0,52	20,37	228,60
COR-10	41,03	40,61	1,43	0,70	2,13	21,41	298,31
COR-11	47,64	35,51	1,40	0,51	2,52	26,57	286,21
COR-12	51,12	28,31	3,22	1,01	2,23	16,89	279,45
COR-13	45,60	35,68	0,87	0,37	2,02	15,71	291,66
COR-14	50,96	32,59	1,41	0,39	1,40	21,03	293,49
COR-15	42,91	35,93	1,40	0,40	1,39	23,57	258,10
TD-07	35,02	33,04	3,73	0,85	1,23	54,76	211,25
TD-08	50,77	43,51	4,65	1,22	0,95	49,48	321,99
TD-09	41,85	44,84	5,66	1,32	0,71	55,18	297,49
TD-10	52,57	55,00	5,04	0,92	2,05	48,70	380,45
TD-12	66,01	58,96	9,66	2,09	0,67	59,44	449,08
TD-13	56,62	49,58	2,37	1,10	2,08	38,65	375,25

Table B.2 Results of the hydrochemical analyses performed on spring water samples (Abete Bianco = ABTH; Thures 2=CTH; Fontana Thures=FTH; Rotazionale=SRTH) at the Thures site. Sampling campaigns are referred to the dates reported in Table 4.2

Sampling campaign	Ca^{2+}	Mg^{2+}	Na^{+}	K^{+}	Cl^{-}	SO_4^{2-}	HCO_3^{-}
ABTH-01	79,29	10,01	3,40	4,99	7,79	25,32	258,28
ABTH-02	70,54	8,19	8,91	12,21	25,94	17,15	233,11
ABTH-03	79,14	9,41	5,16	3,56	10,67	24,50	255,57
ABTH-04	81,88	10,14	13,24	4,39	34,82	19,66	250,59
ABTH-05	56,28	8,95	11,44	3,90	33,23	27,24	154,63
ABTH-06	47,11	5,95	6,76	2,45	23,69	24,53	118,01
ABTH-07	57,78	7,41	7,61	2,70	24,21	28,26	153,95
ABTH-09	56,01	9,88	9,90	4,21	25,03	28,07	167,80
ABTH-10	61,32	12,77	11,90	3,14	37,46	27,56	178,25
ABTH-11	80,51	13,66	9,81	1,36	25,48	28,86	248,93
ABTH-12	95,43	12,56	30,08	4,42	70,13	21,79	283,72
ABTH-13	70,87	11,11	7,56	4,17	21,37	18,64	231,25
ABTH-14	70,22	12,44	12,73	4,60	20,97	26,99	237,96
ABTH-15	81,88	11,93	10,24	5,33	22,92	29,69	256,88
CTH-03	77,44	8,90	0,36	1,18	2,04	27,37	246,53
CTH-04	75,41	8,47	0,39	1,36	0,34	21,20	245,69
CTH-05	41,68	8,99	0,60	1,11	2,09	30,05	130,24
CTH-06	45,16	5,24	0,43	0,77	0,47	26,96	129,78
CTH-07	52,14	5,87	0,33	0,66	0,60	30,68	148,74
CTH-08	65,44	8,47	0,39	1,19	0,53	28,21	206,57
CTH-09	52,64	8,29	0,45	1,15	0,34	29,35	165,66
CTH-10	54,65	9,13	0,24	0,85	1,78	28,39	171,56
CTH-11	61,39	11,92	0,21	0,84	1,74	28,41	206,96
CTH-12	82,89	11,15	0,42	1,39	0,35	19,33	286,17
CTH-13	74,02	10,47	0,21	1,13	1,94	21,68	244,67
CTH-14	63,25	10,51	0,39	1,24	1,01	25,98	211,73
CTH-15	78,99	10,55	0,36	1,28	1,34	29,60	234,91
FTH-01	122,79	20,11	0,65	1,48	2,15	81,42	376,26
FTH-02	108,88	17,76	3,60	1,45	2,40	64,99	346,39
FTH-03	119,13	19,84	0,65	1,48	2,10	79,43	368,44
FTH-04	116,54	18,33	0,79	1,65	0,79	72,36	354,30
FTH-05	91,14	21,55	0,89	1,40	2,31	81,38	278,89
FTH-06	67,33	12,08	0,67	0,89	0,95	77,00	168,77
FTH-07	81,65	14,33	0,58	0,95	0,97	82,04	217,50
FTH-08	101,05	19,88	1,02	1,68	1,68	80,21	307,74
FTH-09	72,54	18,51	0,74	1,45	0,62	80,15	214,79
FTH-10	63,14	22,79	0,66	0,95	2,09	79,32	200,75
FTH-11	101,56	23,52	0,59	0,96	2,02	81,55	320,16
FTH-12	131,10	22,93	1,99	1,99	1,95	81,74	413,08
FTH-13	111,60	20,81	0,45	1,55	2,17	83,92	340,47
FTH-14	108,70	22,55	0,75	1,56	1,24	86,00	339,25
FTH-15	119,38	20,56	0,92	1,58	1,64	80,97	350,23
SRTH-03	116,55	31,48	1,08	2,73	2,94	94,88	401,61

SRTH-04	109,95	29,24	1,13	2,87	0,96	85,71	370,25
SRTH-05	75,41	21,48	1,18	2,47	2,77	93,83	223,32
SRTH-06	65,56	18,94	0,96	1,52	1,95	92,82	177,52
SRTH-07	77,95	22,54	0,91	1,86	1,67	99,42	226,15
SRTH-08	95,01	28,28	1,06	2,62	2,07	95,12	313,43
SRTH-09	51,06	28,77	1,23	2,73	1,66	110,04	164,57
SRTH-10	81,02	33,16	0,94	2,43	5,81	88,46	294,66
SRTH-11	106,27	36,43	0,54	1,24	2,42	96,13	378,47
SRTH-12	124,42	34,60	1,57	2,46	1,48	111,34	414,30
SRTH-13	113,52	34,86	0,83	2,31	3,91	100,85	390,50
SRTH-14	115,89	33,91	1,22	2,99	2,43	99,47	402,71
SRTH-15	122,32	34,57	0,71	2,85	3,17	102,94	402,71

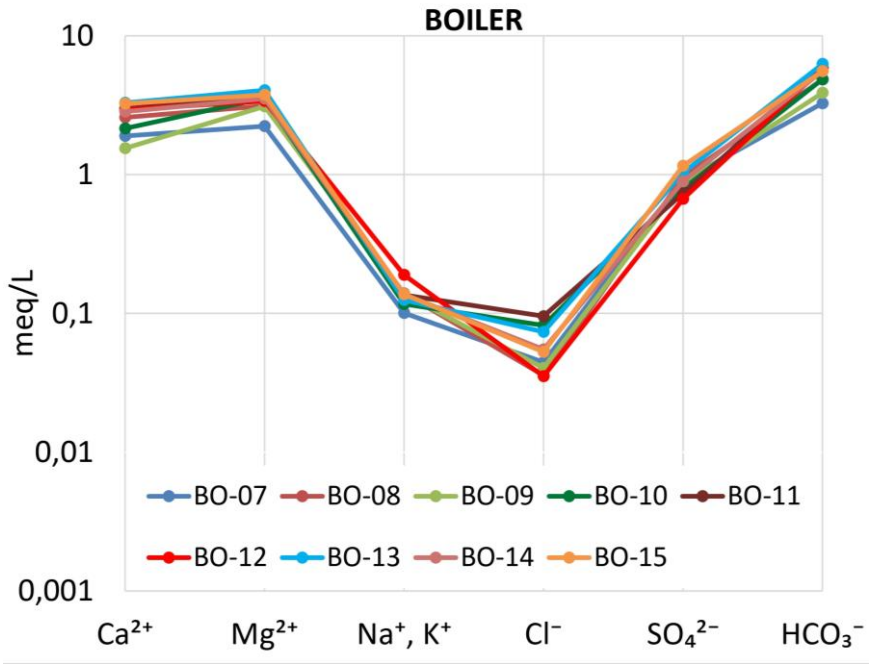

Figure B.1 Schoeller diagram of Boiler spring.

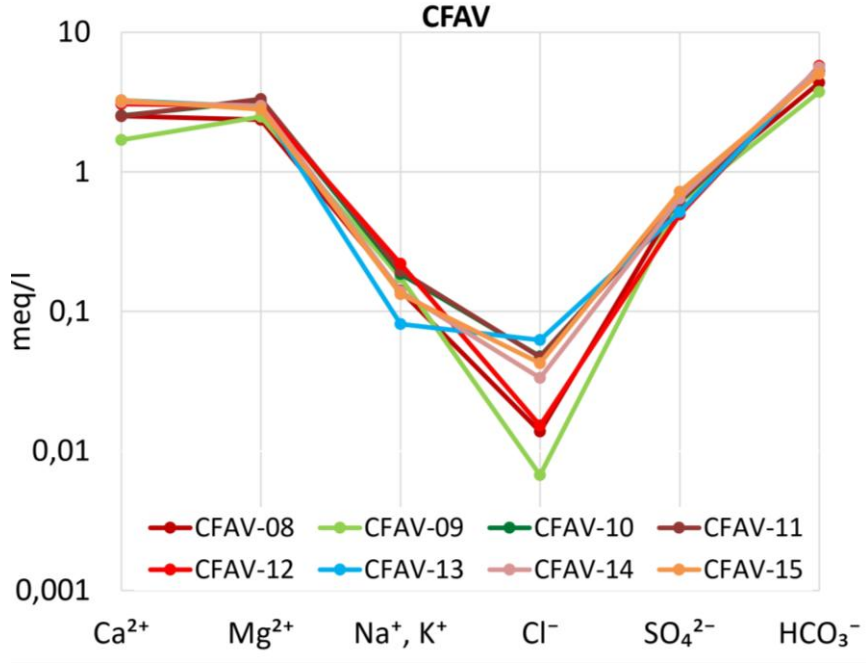

Figure B.2 Schoeller diagram of CFAV spring.

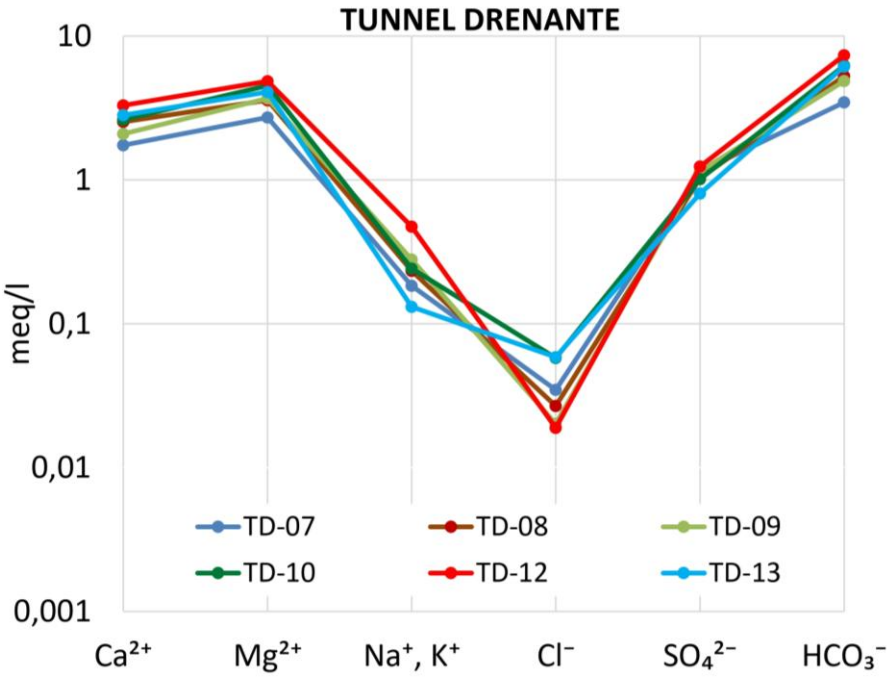

Figure B.3 Schoeller diagram of Tunnel Drenante spring.

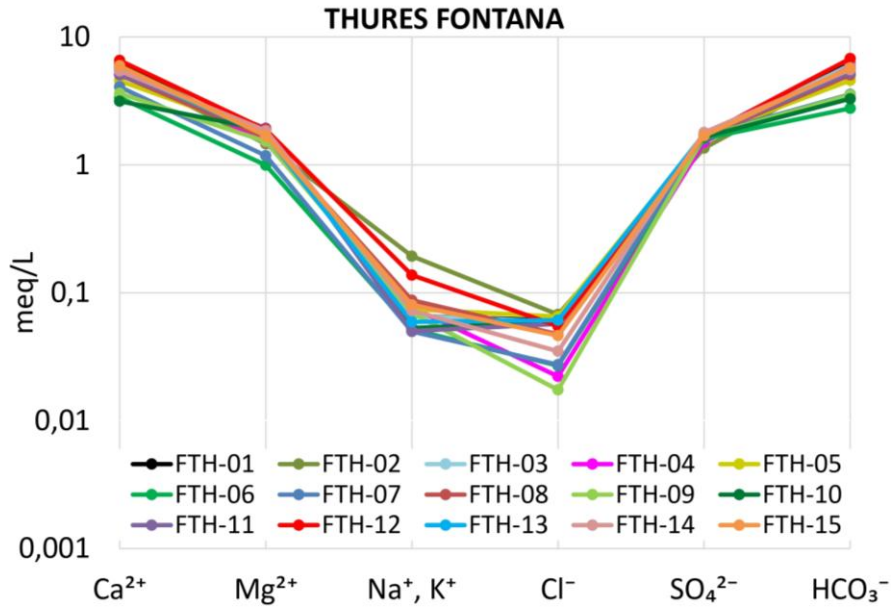

Figure B.4 Schoeller diagram of Fontana spring.

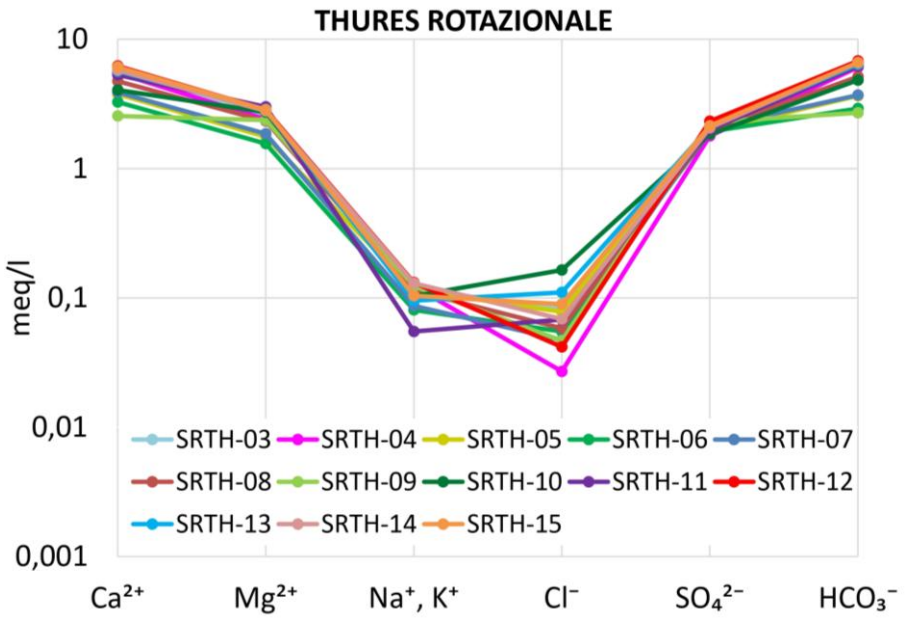

Figure B.5 Schoeller diagram of Rotazionale spring.

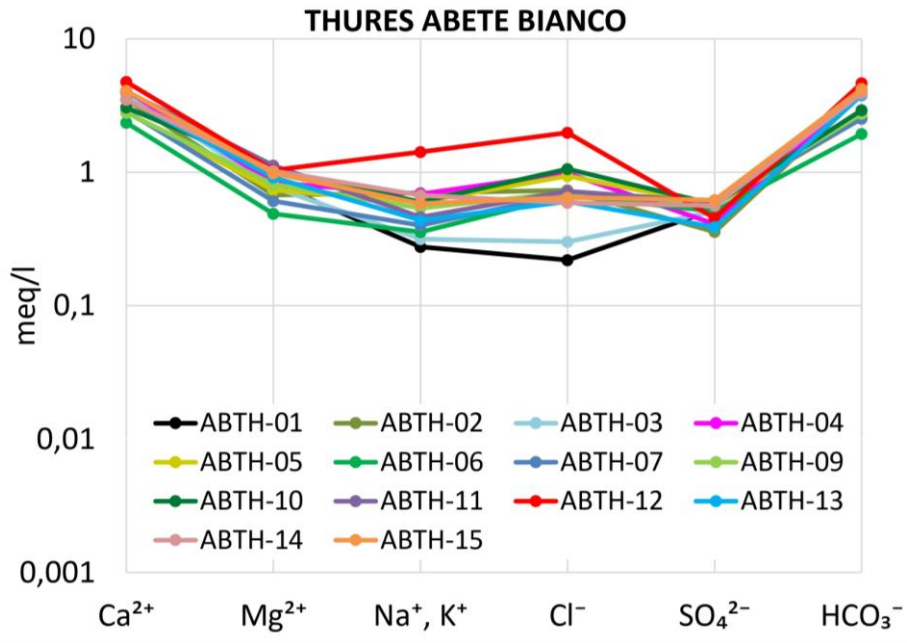

Figure B.6 Schoeller diagram of Abete Bianco spring.

Appendix C

This appendix contains the STL-decomposed time series (Eq. 5.1) of groundwater fluctuations (P6SSTC4) (Figure C.1) and landslide displacements at Champlas du Col (Figure C.2) and Thures (Figure C.3). The displacement patterns were derived from the S6SSTC1A and S6CESB0A inclinometric measurements, respectively, according to the Eq. (3.3). For each parameter, Q–Q plots of the residuals are also provided, as discussed in Section 5.1.

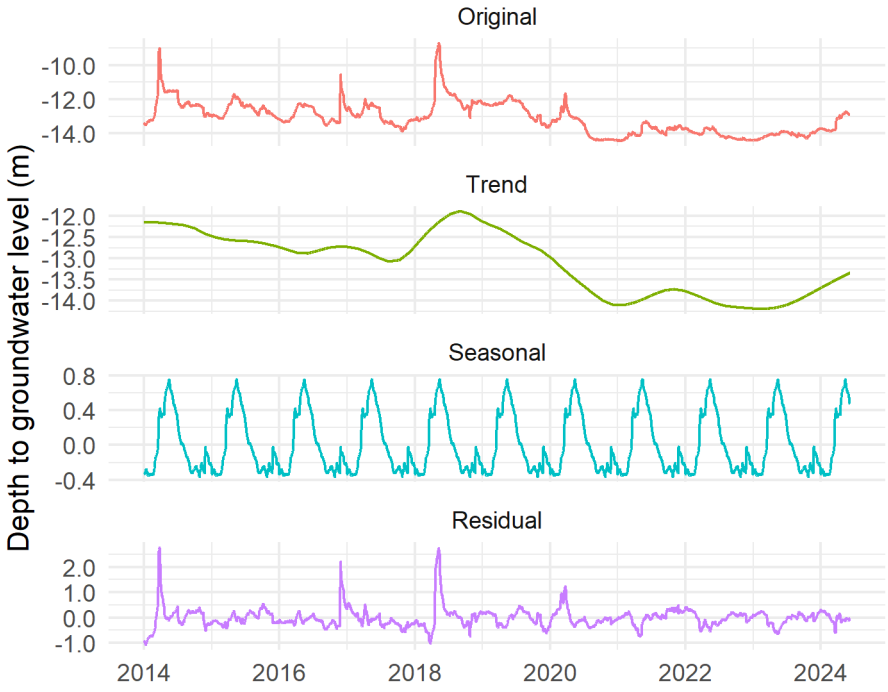

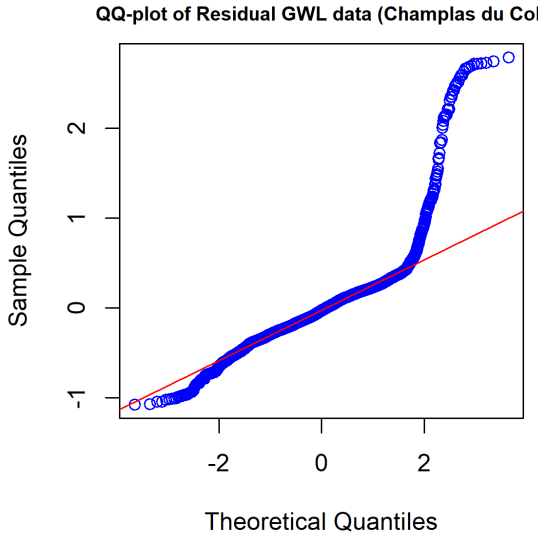

Figure C.1 STL decomposition results of groundwater level (piezometer P6SSTC4).

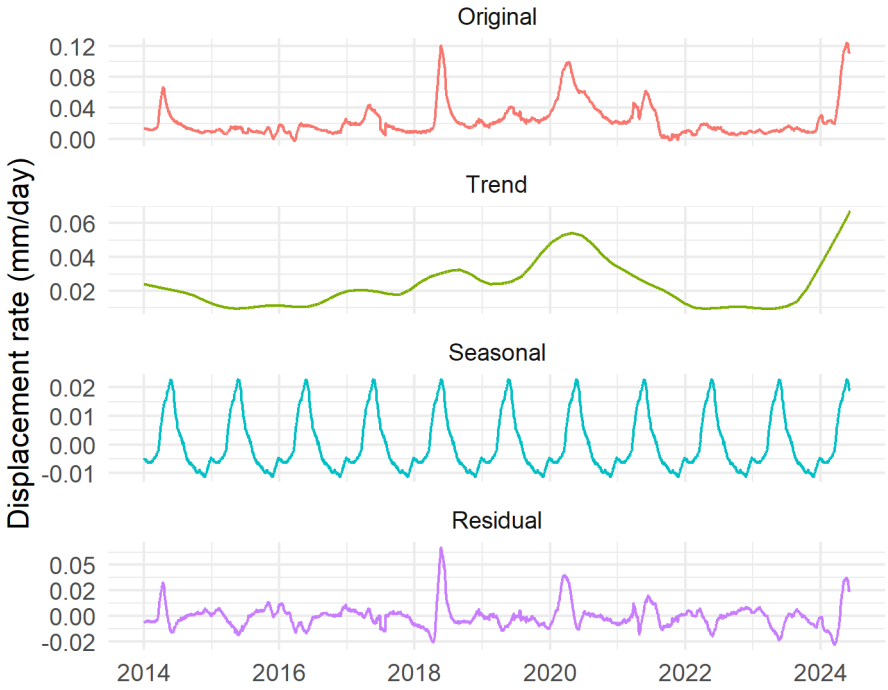

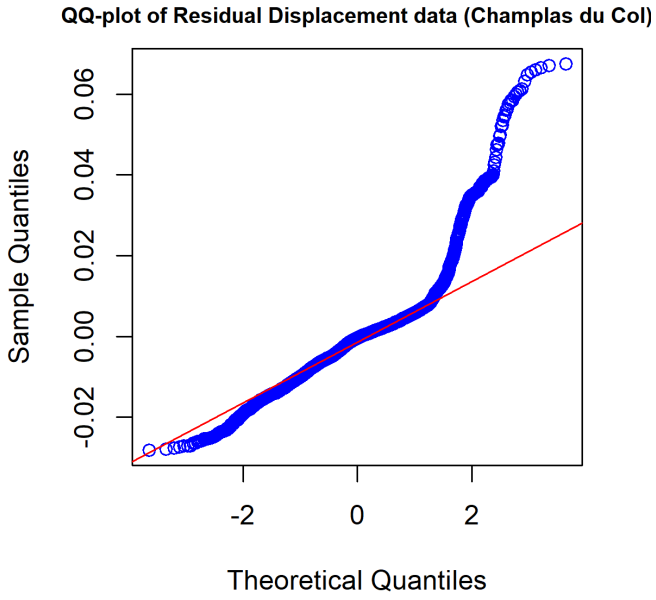

Figure C.2 STL decomposition results of displacement rate (inclinometer S6SSTC1A).

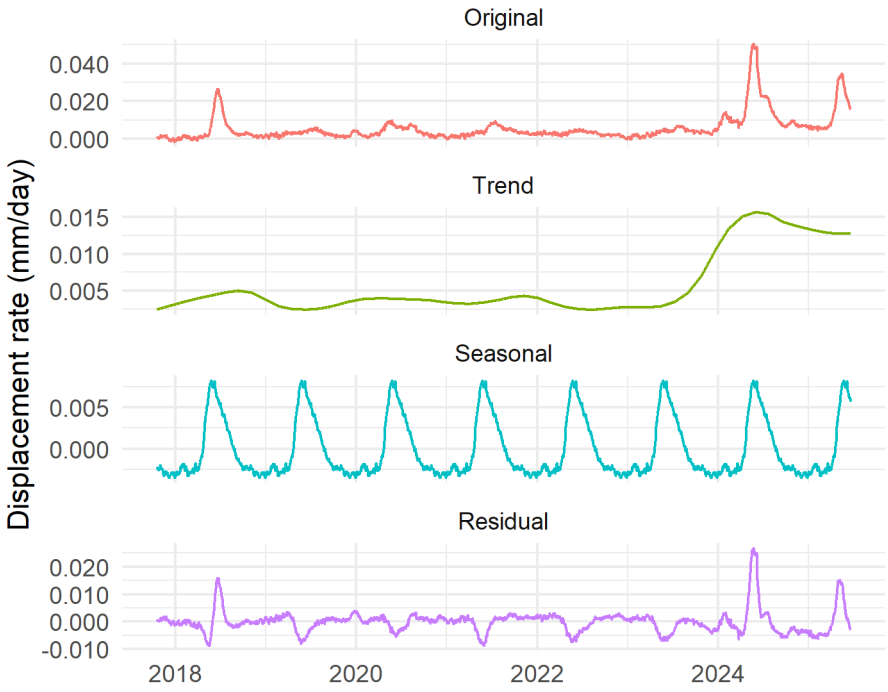

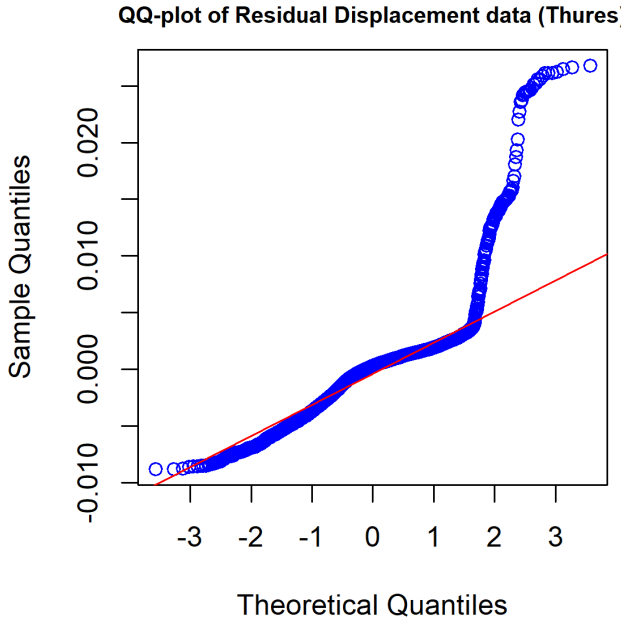

Figure C.3 STL decomposition results of displacement rate (inclinometer S6CESB0A).

This section outlines the process behind the forecasting model presented in Section 5.2, which concerns Multivariate Polynomial Regression (MPR) and the estimation of coefficients.

For a single-output static system that is governed by a *m*-variable smooth function $y = g(x_1, x_2, \dots, x_m)$, the *pth*-order multivariable polynomial function $MPR_p(x_1, x_2, \dots, x_m)$:

$$MPR_P = (x_1, x_2, .. x_m) = \\ = \beta_0 + \sum_{l_1=1}^{m} \beta_{l_1} x_{l_1} \\ + \sum_{l_1=1}^{m} \sum_{l_2=l_1}^{m} \beta_{l_1 l_2} x_{l_1} x_{l_2} + \cdots + \sum_{l_p=l_{p-1}}^{m} \beta_{l_1 l_2 \dots l_p} x_{l_1} x_{l_2} .. x_{l_p}$$

can be used to approximate the smooth function $y = g(x_1, x_2, \dots, x_m)$ at any precision no matter how complex the function $y = g(x_1, x_2, \dots, x_m)$ is, where $x_1, x_2, \dots, x_m$ is the input variables of the system, the order p is a certain non-negative integer, and $\beta_0, \beta_{l_1}, \beta_{l_1 l_2}, \beta_{l_1 l_2 \dots l_p}$ are polynomial coefficients. As the multivariable function $MPR_p(x_1, x_2, \dots, x_m)$ is linear with respect to its polynomial coefficients, standard linear least-squares estimation can be used to estimate these coefficients from experimental observations (Ostertagová, 2012; Wei et al., 2016).

The least squares estimate the regression coefficients, their standard errors and the p-value which indicates how probable the results are due to chance. Conventionally, $p < 0.05$ is referred as statistically significant and $p < 0.001$ as statistically highly significant.

The regression models built for the Champlas du Col (Eq. C.1, C.2, C.3) and Thures (Eq. C.4, C.5, C.6) sites are reported hereafter, together with the corresponding outputs (Table C.1 and Table C.2).

Champlas du Col

$$y_{trend}(t) = \beta_{tr,0} + \beta_{tr,snow,1} snow_{tr}\left(t - \tau_{tr,snow}\right) + \beta_{tr,snow,2} snow_{tr}\left(t - \tau_{tr,snow}\right)^2 \quad (C.1)$$

$$\begin{aligned} y_{seasonal}(t) = {} & \beta_{seas,0} + \beta_{seas,gwl,1} gwl_{seas}\left(t - \tau_{seas,gwl}\right) \\ & + \beta_{seas,gwl,2} gwl_{seas}\left(t - \tau_{seas,gwl}\right)^2 \\ & + \beta_{seas,snow,1} snow_{seas}\left(t - \tau_{seas,snow}\right) \\ & + \beta_{seas,snow,2} snow_{seas}\left(t - \tau_{seas,snow}\right)^2 \\ & + \beta_{seas,rain30,1} rain30_{seas}\left(t - \tau_{seas,rain30}\right) \\ & + \beta_{seas,rain30,2} rain30_{seas}\left(t - \tau_{seas,rain30}\right)^2 \end{aligned} \quad (C.2)$$

$$y_{residual}(t) = \beta_{res,0} + \beta_{res,gwl,1} gwl_{tr}\left(t - \tau_{res,gwl}\right) + \beta_{res,gwl,2} gwl_{tr}\left(t - \tau_{res,gwl}\right)^2 \quad (C.3)$$

Table C.1 Regression results obtained from the model fitting (Champlas du col)

Coefficient	Estimate	Std. Error	p-value
$\boldsymbol{\beta_{tr,0}}$	1.25E-03	1.43E-03	0.383
$\boldsymbol{\beta_{tr,snow,1}}$	8.98E-04	9.31E-05	<0.0001
$\boldsymbol{\beta_{tr,snow,2}}$	-7.04E-06	1.33E-06	<0.0001
$\boldsymbol{\beta_{seas,0}}$	-3.68E-03	1.75E-04	<0.0001
$\boldsymbol{\beta_{seas,gwl,1}}$	1.17E-02	4.34E-04	<0.0001
$\boldsymbol{\beta_{seas,gwl,2}}$	1.78E-02	7.37E-04	<0.0001
$\boldsymbol{\beta_{seas,snow,1}}$	5.60E-05	3.08E-06	<0.0001
$\boldsymbol{\beta_{seas,snow,2}}$	5.56E-07	8.56E-08	<0.0001
$\boldsymbol{\beta_{seas,rain30,1}}$	-1.73E-04	9.24E-06	<0.0001
$\boldsymbol{\beta_{seas,rain30,2}}$	5.76E-06	5.41E-07	<0.0001
$\boldsymbol{\beta_{res,0}}$	-5.84E-04	1.85E-04	<0.01
$\boldsymbol{\beta_{res,gwl,1}}$	1.71E-02	5.93E-04	<0.0001
$\boldsymbol{\beta_{res,gwl,2}}$	1.22E-03	3.38E-04	<0.001

Thures

$$y_{trend}(t) = \beta_{tr,0} + \beta_{tr,lev,1} level_{tr}\left(t - \tau_{tr,level}\right) + \beta_{tr,lev,2}\left(t - \tau_{tr,level}\right)^2 + \beta_{tr,rain14,1} rain14_{tr}\left(t - \tau_{tr,rain14}\right) + \beta_{tr,rain14,2} rain14_{tr}\left(t - \tau_{tr,rain14}\right)^2 \quad (C.4)$$

$$y_{seasonal}(t) = \beta_{seas,0} + \beta_{seas,lev,1} level_{seas}\left(t - \tau_{seas,level}\right) + \beta_{seas,lev,2} level_{seas}\left(t - \tau_{seas,level}\right)^2 + \beta_{seas,snow,1} snow_{seas}\left(t - \tau_{seas,snow}\right) + \beta_{seas,snow,2} snow_{seas}\left(t - \tau_{seas,snow}\right)^2 \quad (C.5)$$

$$y_{residual}(t) = \beta_{res,0} + \beta_{res,level,1} level_{res}\left(t - \tau_{res,level}\right) + \beta_{res,level,2} level_{res}\left(t - \tau_{res,level}\right)^2 \quad (C.6)$$

Table C.2 Regression results obtained from the model fitting (Thures)

Coefficient	Estimate	Std. Error	p-value
$\boldsymbol{\beta_{tr,0}}$	3.71	5.50E-01	<0.0001
$\boldsymbol{\beta_{tr,level,1}}$	-5.52E+01	8.19E+00	<0.0001
$\boldsymbol{\beta_{tr,level,2}}$	2.05E+02	3.04E+01	<0.0001
$\boldsymbol{\beta_{tr,rain14,1}}$	-5.31E-04	9.67E-05	<0.0001
$\boldsymbol{\beta_{tr,rain14,2}}$	1.23E-05	1.74E-06	<0.0001
$\boldsymbol{\beta_{seas,0}}$	-1.82E-04	3.61E-05	<0.0001
$\boldsymbol{\beta_{seas,level,1}}$	1.67E+00	2.95E-02	<0.0001
$\boldsymbol{\beta_{seas,level,2}}$	2.31E+01	6.96E+00	<0.001
$\boldsymbol{\beta_{seas,snow,1}}$	1.17E-05	1.24E-06	<0.0001
$\boldsymbol{\beta_{seas,snow,2}}$	8.70E-08	2.57E-08	<0.001
$\boldsymbol{\beta_{res,0}}$	2.85E-04	6.44E-05	<0.0001
$\boldsymbol{\beta_{res,level,1}}$	1.43E+00	3.80E-02	<0.0001
$\boldsymbol{\beta_{res,level,2}}$	-9.80E+01	1.08E+01	<0.0001

Appendix D

This appendix provides further outputs from the numerical modelling of the Champlas du Col landslide. Total displacement patterns computed along the slope are presented for the spring 2018 (Figure D.1), spring 2024 (Figure D.2) and November 2016 (Figure D.3) scenarios, with the aim of highlighting the spatial distribution of cumulative displacements and the main shear zones under different conditions. A further model evaluation is carried out using surface displacements measured at GPS benchmarks installed on the slope (Figure D.4). Only those located along the investigated cross section are considered. The corresponding nodes (depicted on the mesh in Figure D.2) and the displacement values are then compared with the magnitude and temporal evolution of the GPS-derived surface movements. This provides an independent check on the model capability to reproduce the observed displacement patterns.

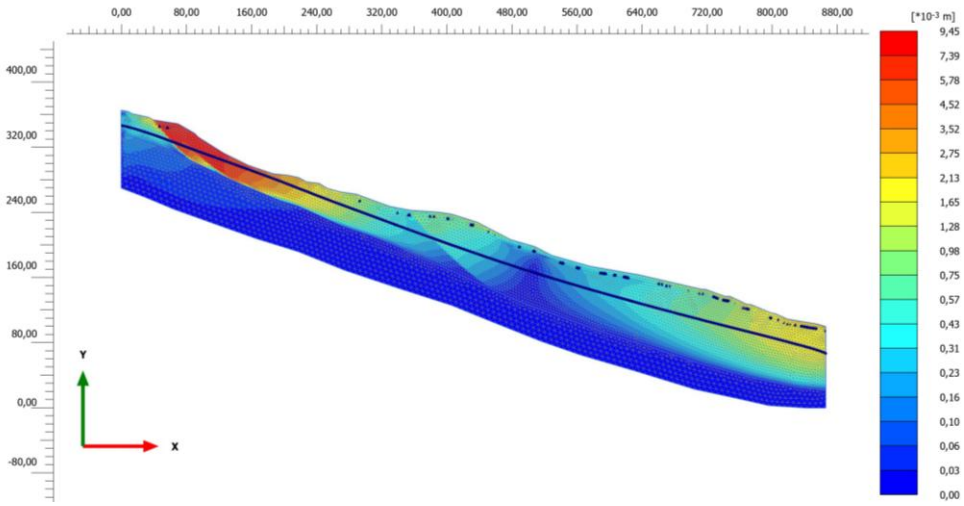

Figure D.1 Total displacements (spring 2018).

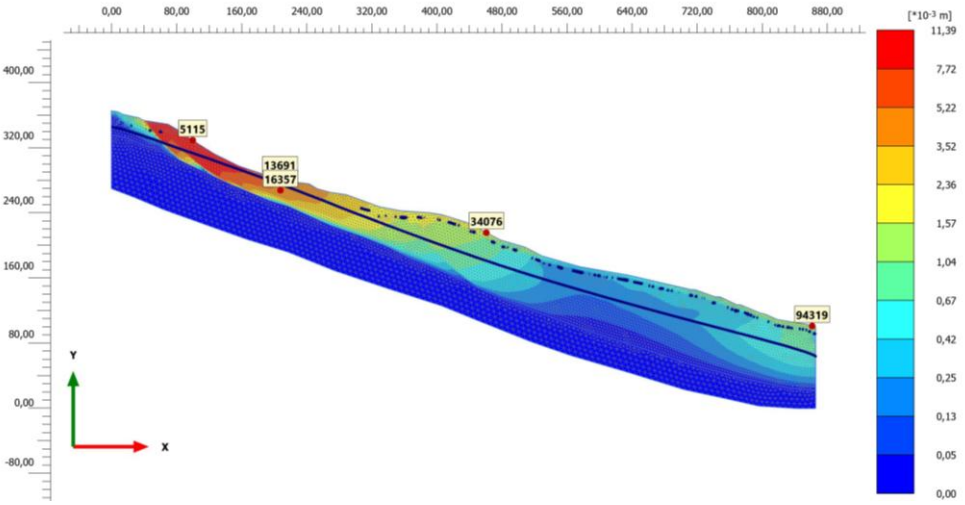

Figure D.2 Total displacements (spring 2024).

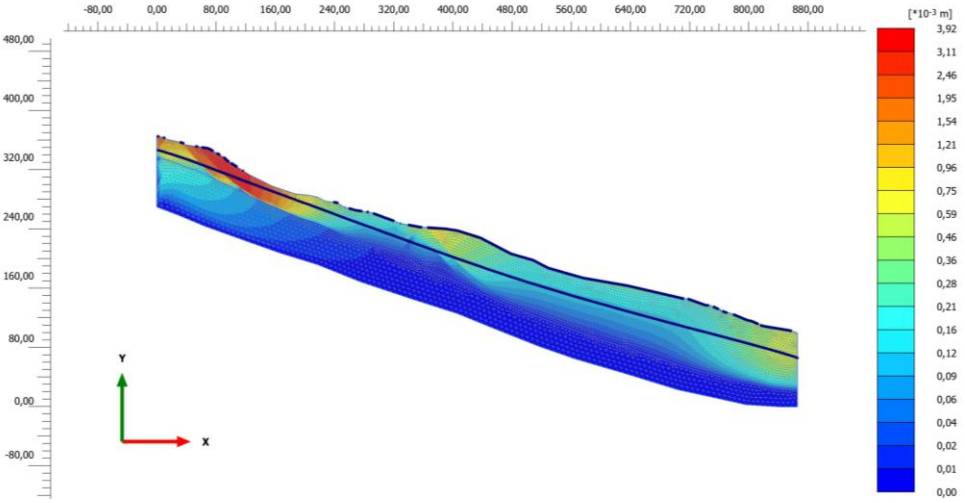

Figure D.3 Total displacements (November 2016).

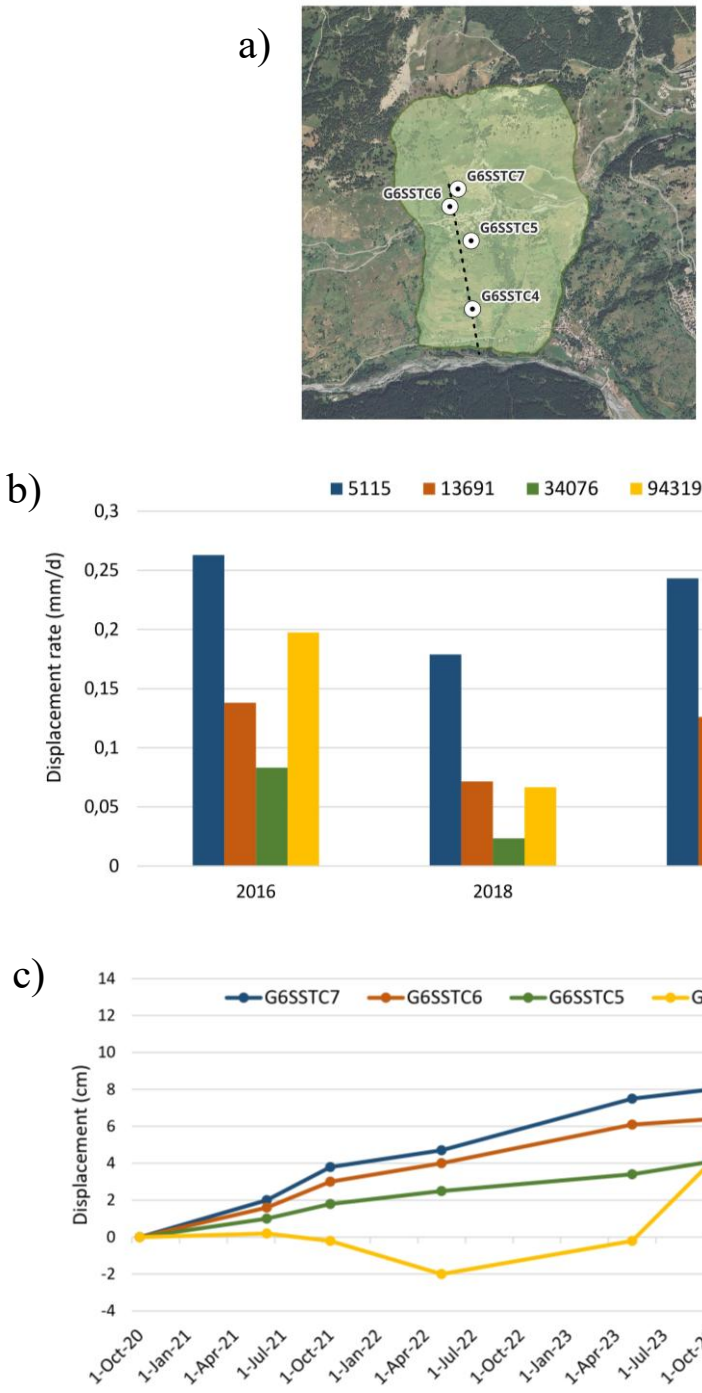

Figure D.4 Comparison between observed and modelled surface displacements at the Champlas du Col landslide: (a) location of the GPS benchmarks along the model section; (b) modelled displacement rates at selected mesh nodes (Figure D.2) for the analysed scenarios; (c) cumulative surface displacements measured at the GPS benchmarks during the monitoring period.